UCL

Design and Modeling of Multi-Arm Continuum Robots

by

Zisos Mitros

THESIS

submitted

in partial fulfillment of the requirements for the degree of

Doctor of Philosophy

January 2022

Thesis Supervisors:

Dr. Christos Bergeles, Prof. Lyndon daCruz

I, Zisos Mitros, confirm that the work presented in this thesis is my own. Where information has been derived from other sources, I confirm that this has been indicated in the work.

Abstract

Continuum robots are snake-like systems able to deliver optimal therapies to pathologies deep inside the human cavity by following 3D complex paths. They show promise when anatomical pathways need to be traversed thanks to their enhanced flexibility and dexterity and show advantages when deployed in the field of single-port surgery.

This PhD thesis concerns the development and modelling of multi-arm and hybrid continuum robots for medical interventions. The flexibility and steerability of the robot's end-effector are achieved through concentric tube technology and push/pull technology. Medical robotic prototypes have been designed as proof of concepts and testbeds of the proposed theoretical works. System design considers the limitations and constraints that occur in the surgical procedures for which the systems were proposed for. Specifically, two surgical applications are considered.

Our first prototype was designed to deliver multiple tools to the eye cavity for deep orbital interventions focusing on a currently invasive intervention named Optic Nerve Sheath Fenestration (ONSF). This thesis presents the end-to-end design, engineering and modelling of the prototype. The developed prototype is the first suggested system to tackle the challenges (limited workspace, need for enhanced flexibility and dexterity, danger for harming tissue with rigid instruments, extensive manipulation of the eye) arising in ONSF. It was designed taking into account the clinical requirements and constraints while theoretical works employing the Cosserat rod theory predict the shape of the continuum end-effector. Experimental runs including ex vivo experimental evaluations, mock-up surgical scenarios and tests with and without loading conditions prove the concept of accessing the

eye cavity.

Moreover, a continuum robot for thoracic interventions employing push/pull technology was designed and manufactured. The developed system can reach deep seated pathologies in the lungs and access regions in the bronchial tree that are inaccessible with rigid and straight instruments either robotically or manually actuated. A geometrically exact model of the robot that considers both the geometry of the robot and mechanical properties of the backbones is presented. It can predict the shape of the bronchoscope without the constant curvature assumption. The proposed model can also predict the robot shape and micro-scale movements accurately in contrast to the classic geometric model which provides an accurate description of the robot's differential kinematics for large scale movements.

Impact Statement

In this thesis, the development of multi-arm and hybrid continuum robots for two surgical applications is presented while theoretical models for the designed systems are shown.

Chapter 1: In this chapter I present an extensive literature review on continuum robots and more specifically on concentric tube robots (CTRs), a class of continuum robots that is increasingly being considered for single-port surgical applications. This chapter can help researchers acquire deep understanding of the research field and produce scientific results in a faster way. The progress on CTRs is shown and an extensive discussion on their design and modelling and on the structural design and optimization of the end-effector is presented. Based on this discussion, researchers can identify gaps in the field of continuum robots in which one can contribute. This work was published in the *Annual Review of Control, Robotics, and Autonomous Systems* [1].

Chapter 3: In this chapter I propose the design, modelling and engineering of a medical robotic system for deep orbital interventions with a focus on ONSF. The prototype and the ability to perform the required surgical task was analysed by various experiments. The designed robotic system is the first suggestion of a robotic system to perform ONSF. It has shown to the scientific community that CTRs can be used in deep orbital interventions and make various surgical approaches less invasive. This work was published in the *IEEE/RSJ Int. Conf. on Intelligent Robots and Systems* in 2020 and in the *IEEE Robotics and Automation Letters* as a dual paper [2].

Chapter 4: In this chapter I present a quasistatic mechanics-based model that

describes the shape of concentric tube robotic arms when they are eccentrically arranged along an also-flexible backbone. This theoretical work proposes eccentrically arranged concentric tubes, it consists the first step towards modeling multi-arm CTR. It was published in the *Int. Conf. on Biomedical Robotics and Biomechatronics (BioRob)* in 2018 [3] and in the *10th Hamlyn Symposium on Medical Robotics* [4]. This work is considered by several international groups as the first work that proposed eccentrically arranged concentric tubes. It has created a new direction in the scientific community, researching ways to increase the dexterity and flexibility of continuum robotic.

Chapter 5: Here, a new type of continuum robot is suggested. The proposed system combines the flexibility of push/pull actuated continuum robots and the dexterity offered by concentric tube robotic end-effectors. A tailored quasistatic mechanics-based model is presented and evaluated on the proposed system. This work was published in the *IEEE Int. Conf. on Robotics and Automation* in 2022 [5]. It shows that hybrid systems can employ the advantages of each technology to achieve increased flexibility. It is envisioned that this work will create new directions in the community to create systems where the advantages of each technology will be combined to create systems with enhanced capabilities.

Chapter 6: Here, push/pull technology is employed to develop a bronchoscope using a miniaturized multi-backbone robot. The suggested system can target positions in the distal lung, while a geometrically exact model of the robot that considers both the geometry of the robot and the mechanical properties of the backbones predicts the robot's shape. It is the first suggestion of accessing all the regions inside a bronchial tree using a robotic system, while the model is the first modelling work aiming to model a push/pull continuum robot taking into account micro-scale movements and providing increased accuracy. This work was published in the *Frontiers in Robotics and AI* in 2021 [6] and shows that continuum robots being actuated by push/pull technology can access deep seated pathologies in the bronchial tree thus increasing the efficiency of lung bronchoscopy which has shown that plays an important role in the mortality of patients.

Acknowledgements

This is a very long list of amazing supervisors, colleagues, friends and family so please bear with me.

First and foremost, I would like to thank my primary supervisor, Dr. Christos Bergeles, for his advices and guidance over the past years. I am grateful for his support, encouragement and help in every aspect of my PhD and personal life. I will never forget the trust and help that he gave me when the stress was overwhelming. I am glad also to have Prof. Lyndon daCruz as secondary supervisor. His clinical inputs and engineering insights were invaluable in my doctorate studies. I am thankful for his support, help and the fact that he was always there for me.

This work is a product of deep conversations with Dr. Mohsen Khadem, Dr. Carlo Seneci and Dr. Hadi Sadati. I will never forget our extensive meetings and their willingness to answer the too many questions that I had. Our meetings were inspiring, challenging and highly engaging. I am very fortunate to have worked with them and consider them now friends. A special thanks to Dr. Khadem for letting me intern at his lab and supervise me in the exciting bronchoscopy project.

A special thanks also to all the members of RVIM lab for our conversations and for making my PhD time a lot funnier and less stressing. I will totally miss our coffee breaks and the time in the lab and the office. A special thanks to Claudio, John, Ross, Omar and Harris with whom we either started our PhDs at the same time and/or spent a lot of time working together. I am also grateful to Anestis, Sotiris and Thodoris. We started this journey together and without them I wouldn't be able to finish it. Our time in the lab, it'll always make me smile. Thank you for your friendship!

'Μια αστραπή η ζωή μας... μα προλαβαίνουμε '

Νίκος Καζαντζάκης

Στη μνήμη του θείου μου, Βαγγέλη

To my uncle's memory, Vangelis

Contents

List of Figures

List of Tables

Chapter 1

Introduction

1.1 Motivation

The motivation of this dissertation arises from the vision that robotic instrumentation will provide surgeons with new, enhanced capabilities for minimally invasive surgeries (MIS). Robot-assisted single port surgery is predicted to be the next step in MIS as it offers lower morbidity, improved cosmesis due to the elimination of peripheral ports, reduced trauma, and shorter hospitalization time [26, 27].

Continuum robots are systems that do not possess rigid links and identifiable rotational links [28]. They can bend continuously along their length via elastic deformation and produce snake-like motions. Continuum robots have been studied as surgical systems as they promise to deliver optimal therapies when anatomical pathways need to be traversed and deep seated pathologies are targeted. Their flexibility and dexterity promise to overcome the challenges of confined surgical workspace and lack of articulation.

1.2 Dissertation Overview and Contributions

The dissertation is divided in five chapters in total. Chapter 1 discusses the motivation that drives this research and presents an extensive literature review on CTRs which is the main focus of this work and on continuum robots in general. Chapter 2 includes the mathematical background needed for the derivation of the proposed modelling theory describing the shape of multi-arm CTRs and hybrid continuum robots. Chapter 3 presents a multi-arm CTR for deep orbital interventions,

with a focus on ONSF. Next, Chapter 4 discusses the modelling of eccentrically arranged CTRs, while Chapter 5 proposes an alternative design option of multi-arm continuum robots. Specifically it presents a new class continuum robot combining push/pull and concentric tube technology. Chapter 6 discusses the modelling and design of a robotic bronchoscope for distal lung sampling employing solely the push/pull technology. Finally, Chapter 7 concludes this dissertation.

This dissertation contributes to the field of continuum robots in several ways. It shows that continuum robots can make deep orbital interventions less invasive and lung bronchoscopy be performed with higher efficiency. Here, several medical robotic prototypes have been designed as proof of concepts and testbeds of the proposed theoretical works. These prototype showcase new design options and propose to the scientific community ways to enhance the dexterity of the end-effector and the delivery of multiple tools to the surgical area of interest. All the developed systems propose new modelling approaches which contribute to the effort of predicting the shape of the continuum end-effector.

1.3   Continuum Robots

Continuum robots show promise in single port surgeries in which instrumentation with increased dexterity and flexibility is required to overcome the challenges of confined surgical workspace and lack of articulation. They can be categorized by their structural design and actuation strategy [26] as can be seen from Fig. 1.1-1.2.

A medical continuum robot can be either a single backbone system or a multi-backbone (see Fig. 1.1). Single backbone systems have one central elastic element that permits the passage of actuation elements and can house the required surgical tools. Various materials have been used in the development of single backbone robots such as springs, elastic rods and tubes, braided polymer tubes and molded polymers. A characteristic example of a single backbone system is described in [9] and shown in Fig. 1.1c. On the other hand, multibackbone systems are composed of multiple elastic elements that are constrained with respect to each other typically by the use of rigid fixtures. In [7], a central backbone is employed with multiple sec-
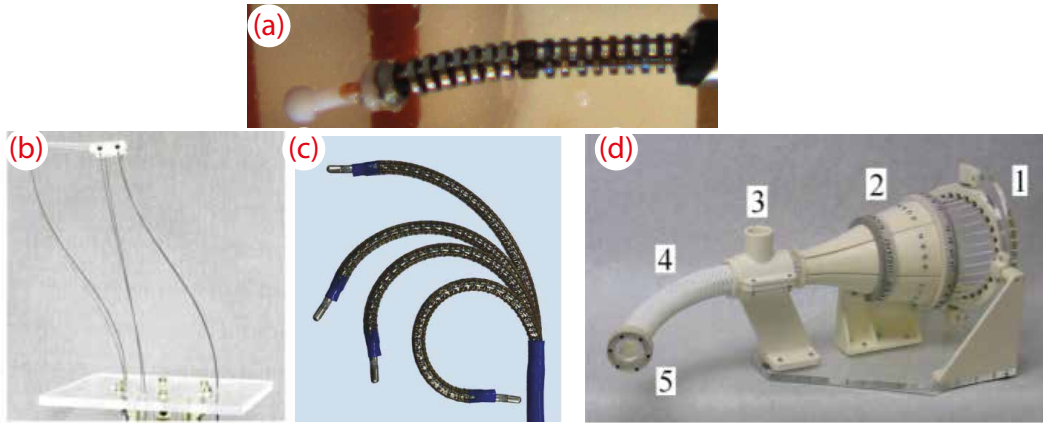
Figure 1.1: Continuum robots are categorized as single backbone systems or as multibackbone: Characteristic examples of continuum robots are a) a central backbone with multiple secondary backbones per bending segment [7], b) a multibackbone system without intermediate constraints [8], c) a characteristic example of a single backbone system [9] and d) a multiple backbone system composing of many interlocking fiber backbones [10].

ondary backbones per bending segment that are eccentrically arranged with respect to the central backbone (see Fig. 1.1a). In a similar approach, a manipulator made of many interlocking fiber backbones that run down the length of the manipulator was proposed in [10] and shown in Fig. 1.1d while in [29, 8], an approach of multibackbone systems without intermediate constraints was proposed (see Fig. 1.1b). A classic multi-backbone system is shown in Fig. 1.2b.

Moreover, continuum robots can be categorized as intrinsically or extrinsically actuated based on where actuation occurs. In [26], actuation is defined as the final conversion of power to the mechanical energy domain. Extrinsically actuated systems in surgical applications are the tendon/cable driven mechanisms and multibackbone structures, [6, 7, 30]. Their actuation is based on the push/pull of tendons/rods from their proximal end to control the overall shape of the manipulator. Transmission mechanisms with intrinsic actuation include hydraulic and pneumatic chambers [16, 14], embedded micromotors [31], fluidic-reinforced elastomers [32] and McKibben muscles [33].

1.4 Progress in Concentric Tube Robots (CTRs)

Concentric Tube Robots (CTRs), also known as active cannulas, are continuum robots that possess a continuously flexible backbone that comprise concentric pre-
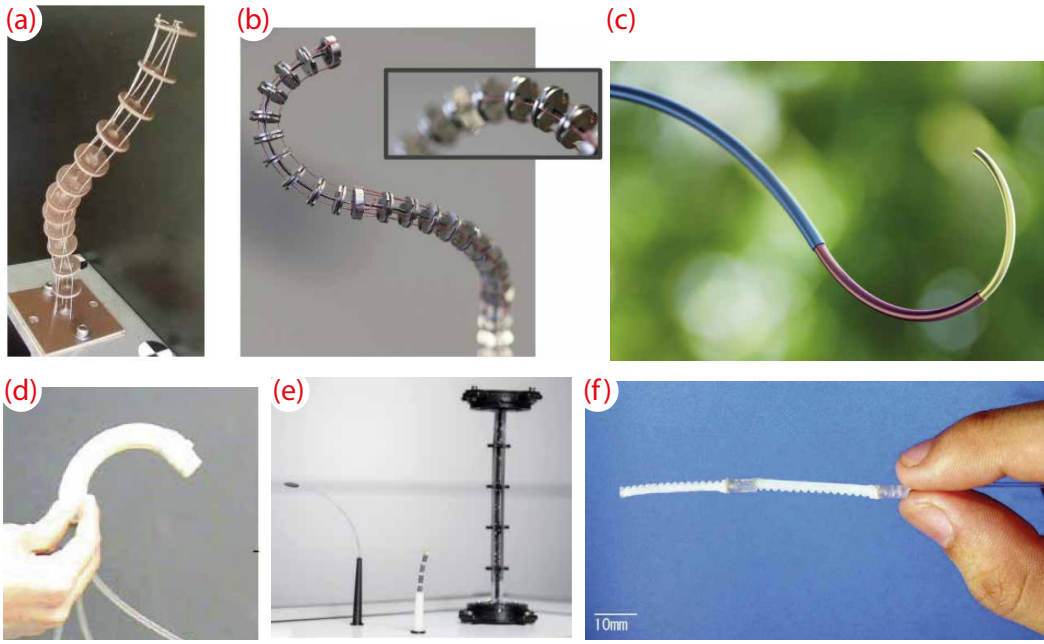
Figure 1.2: Continuum robots categorized by their structure and method of actuation. Extrinsic actuation: a) Tendon driven system [11], b) Multi-backbone system [12], c) Concentric Tube Robot [13]. Intrinsic actuation: d) Pneumatic system [14], e) System with shape memory alloys [15] and f) Hydraulic system [16].

curved tubes made of super-elastic material, most commonly nitinol (NiTi). They are preferred to be employed as surgical robotic end-effectors compared to other technologies due to the increased capacity of tubes to exhibit large curvatures as their diameter decreases, and due to the tubes' tuneable application-specific stiffness. This is one of the reasons that CTRs are investigated in this dissertation to be employed in making surgical interventions less invasive. The shape and tip pose of those miniature robotic manipulators is controlled by the relative rotation and translation of each tube. Thus, CTRs are able to steer without the need to exert force on tissue [34, 35]. They are categorized as extrinsically actuated due to the axial rotation and translation of the tubes' bases, despite the effect that each tube has on the others. Bending actuation arises due to elastic interaction between the tubes. Since their actuation is only based on the flexing of their own backbone, i.e., the robot's outermost structure, and not on mechanisms like tendon wires or pneumatic/hydraulic chambers, they are able to steer in hollow regions or liquid filled cavities. CTRs can be very thin without sacrificing dexterity as they are externally actuated.

The first concentric tube style device was disclosed in a patent application filed in 1990s [36] and was composed of a straight outer tube and a precurved NiTi wire. The device was proposed for the localization of lesions within the body and, in particular, of non-palpable lesions within the breast. Cuschieri *et al.* [37] highlighted for the first time the new directions that concentric tube devices, made of precurved tubular NiTi components, can open up in endoscopic surgeries. Few years later, Daum GmbH filed a patent application for a deflectable needle assembly which included a telescoping cannula, a catheter and a stylet [38]. The catheter, made from NiTi, was curved at its distal end and axially rotatable within the lumen of the cannula. The first motorized concentric tube system was presented in [39] in 2005 and the first mechanics-based models were introduced by [40, 41] in 2006. Since then, energy minimization methods, Bernoulli-Euler beam theory, Cosserat rod theory and, recently, data-driven learning of forward and inverse kinematics of a CTR have all been explored as modelling approaches for effective robot control. Similar progress has been achieved on the computational design of CTRs, incorporating task considerations and patient-anatomy constraints. Eccentric arrangement of tubes is also being investigated, while multi-arm CTRs with straight or flexible backbones have also appeared. The former are already being considered for first-in-human evaluation and clinical translation, [42]. Startups leveraging this technology have started working on bringing systems into the operating room (OR) (see Virtuoso Surgical (virtuososurgical.net) and EndoTheia, Inc. (www.endotheia.com)).

To get into depth in the research of CTRs for various interventions and understand their limitations and the advancements in the field, an extended literature survey was performed [1]. The robot prototypes are critically discussed along with their design principles and constraints. The theoretical contributions are identified, and a comparison between the theoretical models is presented. The literature review is the first step towards our own research in the field of continuum robots and concentric tube robots.

The scientific literature search was conducted by considering the flagship robotics conferences e.g. ICRA, IROS, BioRob, RSS, journals e.g. IJRR, TRO,
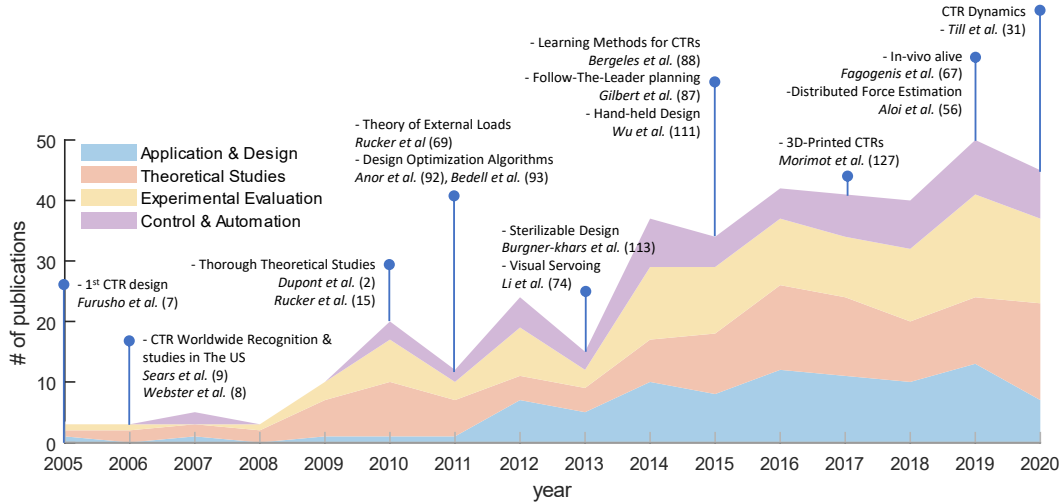
Figure 1.3: Number of occurrence of keywords categories per year versus the number of publications. Selected works in the research field of CTRs are shown.

TMECH, TBME, Frontiers in Robotics & AI, Annuals Reviews and previous review works [43, 44, 45]. Each journal and conference dated back to the year that the first paper related to CTRs, or the first issue of a journal was published, was searched for related work. At that stage, the first search was performed using keywords: continuum robot, active cannula, CTR and soft robot. Then, the collection of the papers that had been identified was further evaluated with regards to its "forward" citations and "backwards" references. All papers were read and categorized based on their focus. The main categories of keywords were: application and design, analysis and modelling theory, experimental evaluation, and control, which are all echoed in the manuscript's organisation. Figure 1.3 shows the number of occurrences of each category per year versus the number of publications. In the beginning, biannual publication rise is observed probably due to the limited research groups working on CTRs. Subsequently, a steady rise shows the spread of research. Moreover, Fig. 1.3 shows the increased number of publications on control of CTRs that progressively takes place.

In this dissertation, the literature survey on the developed CTR systems, modelling theory and design optimization techniques is presented. The presented survey is part of an extensive literature review in the field of CTRs which was published on *Annual Review of Control, Robotics, and Autonomous Systems* entitled "From

Theoretical Work to Clinical Translation: Progress in Concentric Tube Robots" in which the author of this dissertation is the first author [1].

1.4.1 Modeling

A CTR's workspace is determined by the robot tubes' precurvature, stiffness, and length. The joint to task-space mapping for a CTR is complex, consisting of unstable equilibrium points causing snapping (structural instability resulting in the robot's rapid transitioning from one configuration, i.e. equilibrium state, to another of lesser energy), and constraints resulting in non-commutativity of the robot input sequence [46, 44]. These characteristics complicate the modeling of CTRs.

Quasi-Static Models: Two of the most widely studied and referenced CTR mechanics models are based on (i) curvature weighted superposition [47, 48, 34] and (ii) differential (variable) curvature kinematics [35]. Beam mechanics or Cosserat rod theories and Hooke's material law are utilized as the system conservational (system) and constitutional (material) laws (mechanics) for both the aforementioned kinematic representations.

In weighted curvature superposition, the system kinematics (tubes' local shape and orientation) is based on weighted curvature superposition combined with torsional rigidity. The curvature weights are the tubes' bending and torsional structural stiffness values, which form a simple to integrate Initial Value Problem (IVP) that is well-suited for real-time numerical performance.

In differential curvature kinematics, the system kinematics is derived via a set of differential equations for curvatures and torsion known as variable curvature kinematics in continuum robotics. The system kinematics is usually combined with Cosserat rod theory to derive the system governing equations [35]. As a result, a Boundary Value Problem (BVP) is formed with unknown boundary conditions at the base and tip of the robot backbone, which can be solved via numerical optimisation method, e.g. single shooting [35]. This method is favorable because of accuracy, generality, and robustness.

Other investigated models include: (iii) approximating the robot forward map via curve (e.g. Truncated Fourier Series) fitting [49], (iv) forming a lookup table

for the robot input-output relation based on precollecting experimental or precomputing simulation data collection, (v) simplifying the system BVP problem based on tube-base force sensing [50], (vi) finite shell element modeling based on piecewise constant strain assumption [51, 52], (vii) Reduced-Order techniques based on curvature [53] and shape polynomial [54] approximation, and (viii) learning-based methods [55, 13, 56]. The effect of external loads are extensively studied based on Cosserat rod model [57, 58]. A summary of the technical aspects, implementation procedure, advantages and shortcomings of these methods are presented in Table 1.1, where l is length, ϕ is twist angle, κ is curvature, C is fitting curve coefficient, $\mathbf{p}$ is Cartesian position vector, n_t is number of tubes, n_s is number of overlapping segments, n_e is number of finite elements, n_ψ is number of shape functions in a fitting method, n_p is polynomial order, and i, j, k are general numerators.

Absolute (Euclidean distance of simulation predictions and robot tip position in experiments) and relative (absolute error value divided by the robot backbone curve length expressed in percentage) error values are used for experimental verification of theoretical studies. The state-of-the-art relative error for the modeling tasks is approximately $1.5 - 2\%$ ($1.5 - 4.7$ mm) [57, 59]. The modeling and tracking error can reach values as small as 0.02 mm for carefully optimized tube parameters and simple trajectories [60]. Adaptive frameworks, e.g. truncated Fourier series shape estimation (3 mm, 1.2% error) [61], and Kalman-filter-based model parameter estimation (2 mm, 0.8% error) [62] can improve the accuracy of the physics-based models. Medical applications of CTRs usually call for positioning accuracy of $1 - 2$ mm [61], implying that models can perform on par with the clinical requirements. It must be noted, however, that most models and controllers perform their best in unloaded conditions.

Elastic Stability & Snapping Motion: Relative rotation of the tubes results in the accumulation of torsional energy up to an unstable point where this torsional energy overcomes the bending energy. At these unstable points, the system's torsional energy is released causing the tubes' rapid motion, known as snapping. Such sudden high energy motion is usually undesirable in medical interventions and should

be avoided by structural design, motion control, or planning [63]. Mathematically, this instability is associated with a bifurcation point in the tube tip twist angle when plotted versus the base input rotation angle. This is equivalent to the appearance of two stable points in the deformation energy plot versus the tubes' base rotation angle [48]. The system static formulation has multiple solutions (equilibrium points) at this instance, known as a system with cardinality greater than one [64].

The system's linearized governing equations can be used to analyze the system local (arbitrary tube number) and global (two-tube systems) stability [65, 64]. Alternatively, the relation between the tubes' distal and proximal rotation angle [66], investigating the momentum free condition at the distal tube ends [67, 68], the bifurcation and elastic stability theory [65, 69], and employed optimal control theories based on second time-derivative of elastic energy function [70] can be used. More recently, local stability of CTRs with general precurved shapes, e.g. helical, were investigated [64]. Snapping's sudden energy release may be utilized to perform high energy tasks such as driving a suturing needle through a tissue. Such efforts significantly benefit from dynamic models able to capture the snapping transient dynamics [71, 72, 54].

Hysteresis Due to Tube Friction & Clearance: CTRs' shape not only depends on the actuation input values but also on their time history due to the tubes' friction and clearance. These are the main sources of hysteresis in the system. Early investigation based on simple mechanical models by [73] suggested that the dominant effect of the frictional force is associated with concentrated bending moment at the tube ends. More recently, [74] reported the hysteresis due to distributed torsional friction as the main source of CTR modeling inaccuracy compared to the tube clearances.

Table 1.1: Forward and inverse modeling techniques for CTRs.

Models	Curvature Superposition (Piecewise Const. Curves)	Differential Curvature (Truncated Fourier Series)	Approximate Forward Map	Precomputed Lookup Table
Ref.s	[41, 75]	[76, 35, 77]	[49]	[78]
States	$l_i, \phi_i, \kappa_i, i=1..n_s$	$l_i, \kappa_{(s)}, \phi_{i(s)}, i=1..n_t$	$C_i, i=1..n_\psi$	$l_i, \phi_i, \mathscr{P}_t, i=1..n_s$
[No.]	$[3n_s]$	$[\infty]$	$[n_\psi]$	$[2n_t+6]$
Inv. Kin.	Inv. Jacobian, Num. optimization or lookup table	Inv. Jacobian, Num. optimization or lookup table	Analytical	Lookup table
Dynamic	NA	[72]	No	No
IK Algoritm	1. Desired tip position $\mathscr{P}_t$ 2. Piecewise CC fitting 3. Inputs (l_i, ϕ_i) via inv. CC map 4. Mapping for external loads	1. Form optimization problem based on forward map 2. BCs initial guess for curvatures 3. Inv. Kin. via num. optimization	1. Forward kin. precomputation 2. Fourier Series fitting 3. Inv. kin. via the fitted mapping	1. Forward kin. precomputation 2. Forming look-up table 3. Inv. kin. via table search
Error	4 & 1.9 mm (0.3 & 1.3%) (without & with load)	2-12.5 mm (1.5-3.9%)	0.03-4.2 mm (0.01-3.1%) 0.06 − 8.6°	3-21 mm (1 − 7.5%)
Pros.	+ Real-time + Inv. kin. map + Simplest model + Multiple solutions	+ Inv. compliance map + Inv. kin. map + Exact formulation + Multiple solutions	+ Real-time + Inv. kin. & compliance maps + Real-time adaptive implementation	+ Fast inverse map + Inv. kin. & compliance maps
Cons.	- external load only via separate mapping - if High relative stiffness - Only circular const. pre-curves	- Num. inefficient - Initial guess issues - Sever Convergence issues - Hard to find multiple solutions - Dataset richness limitations	- Pre-known external loading - Fixed lengths - Fitting convergence issues - No multiple solutions	- No external loads - No multiple solutions - Storage memory issue
Software	NA	[72]	NA	[80]

Models	Forward Integration by Sensing Base Loads	Discretization (finite shell or constant strain elements)	Reduced-Orde Kin. (Polunomial Curve or Shape Approx.))	Deep learning & (Neural Network models)
Ref.s	[81, 82]	[51, 83, 52]	Renda2021ARobots, sadati2020	[55, 56]
States	$l_i, \kappa_{(s)}, \phi_{i(s)}, i=1..n_t$	$l_i, \kappa_{ij}, \phi_{ij}, i=1..n_t, j=1..n_e$	$C_{ijk}, i=1..nt, j=3 \text{ or } 4, k=0..n_p$	NN parameters
[No.]	$[\infty]$	$[3n_t n_e]$	$[(3 \text{ or } 4) \times n_t \times n_p]$	[No. of NN parameters]
Inv. Kin.	Multi-layer	Inv. Jacobian	Inv. Jacobian, Optimization	Neural Network
Dynamic	No	No	Yes	No
IK Algoritm	1. Cosserat rod formulation 2. Forward integration with known BCs at $s=0$	1. Discretized rod formulation 2. Forming an optimization problem 3. Solve for system states	1. General form shape function 2. Substituting in governing eq. (derive linear form) 3. Solve for C_{ijk}	1. Large experimental dataset 2. NN training 3. Inv. kin. via the trained NN
Error	1.5-4.7 mm (1-3%)	3.3 mm (1.3%, no load) 2.5-4% (point & distributed load)	2.5 mm (1.3%)	forward: 1.36-2.3 mm (0.6-1%), 1.1° inverse: 4 mm (1.7%), 8.3°
Pros.	+ Real-time + Force observation + Force compensation controller	+ Possible real-time implementation + External loads + Finite num. of states + Multiple solutions	+ Possible real-time implementation + Inv. kin. & compliance maps + Finite number of states + Multiple solutions + External loads	+ Fast inverse map + Inv. kin. map + High accuracy
Cons. LightCyan	- Sensitivity to force sensor errors - Requires known loading condition - Complex setup design - no inv. kin. or compliance map	- Requires convergence guarantee - Computationally expensive - Complex inv. kin. formulation	- Complex derivation - Estimation causes error - Convergence guarantee needed	- Known loading condition - No multiple solutions - Dataset richness limitations
Software	NA	NA	TMTDyn by [54]	NA

Dynamic Modeling: Existing quasi-static models evaluated independently or as part of inverse kinematics approaches cannot capture the system transient dynamics, such as vibration and overshoot due to snapping, high bandwidth maneuvers when the system inertial forces matter (e.g. for a hyper-elastic structure robot [84] or due to sudden exertion or release of external loads [72]). Furthermore, extra modeling layers are needed to capture system hysteresis and Coulomb friction [73]. Till *et al.* [72] presented the first dynamical model for CTRs by extending their real-time solver for dynamical modeling of continuum robots based on differential curvature kinematics and Cosserat rod mechanics [57, 59]. Their model could capture a CTR's transient vibrations after snapping and environmental contact release. However, the employed Cosserat rod-based methods require an infinite number of states and are not suitable for nonlinear control and observation design. Recently, approaches based on modelling with reduced number of states attempt to address these challenges [53, 54].

1.4.2 CTRs in Surgery & Intervention

In this subsection, concentric tube robot prototypes are organised according to their surgical application. The singled-out prototypes have been evaluated on realistic phantoms and/or cadavers, or show innovative design characteristics. Figure 1.4 provides a pictorial overview of some of the discussed systems.

Brain & Skull Base Surgery: Skull base surgery takes place near locations where neurovascular structures enter and exit the brain. It is prescribed for a wide variety of neurological disorders, such as intracerebral hemorrhage (ICH), brain tumors, and epilepsy. Rigid instruments limit the effectiveness of procedures as they must follow straight trajectories resulting in increased danger to harm critical tissue and structures. When regions deep inside the brain must be reached, conventional approaches can result in heavy trauma to healthy brain tissues. CTRs promise to dexterously access regions within the brain and skull base and deliver therapies to deep seated pathologies.
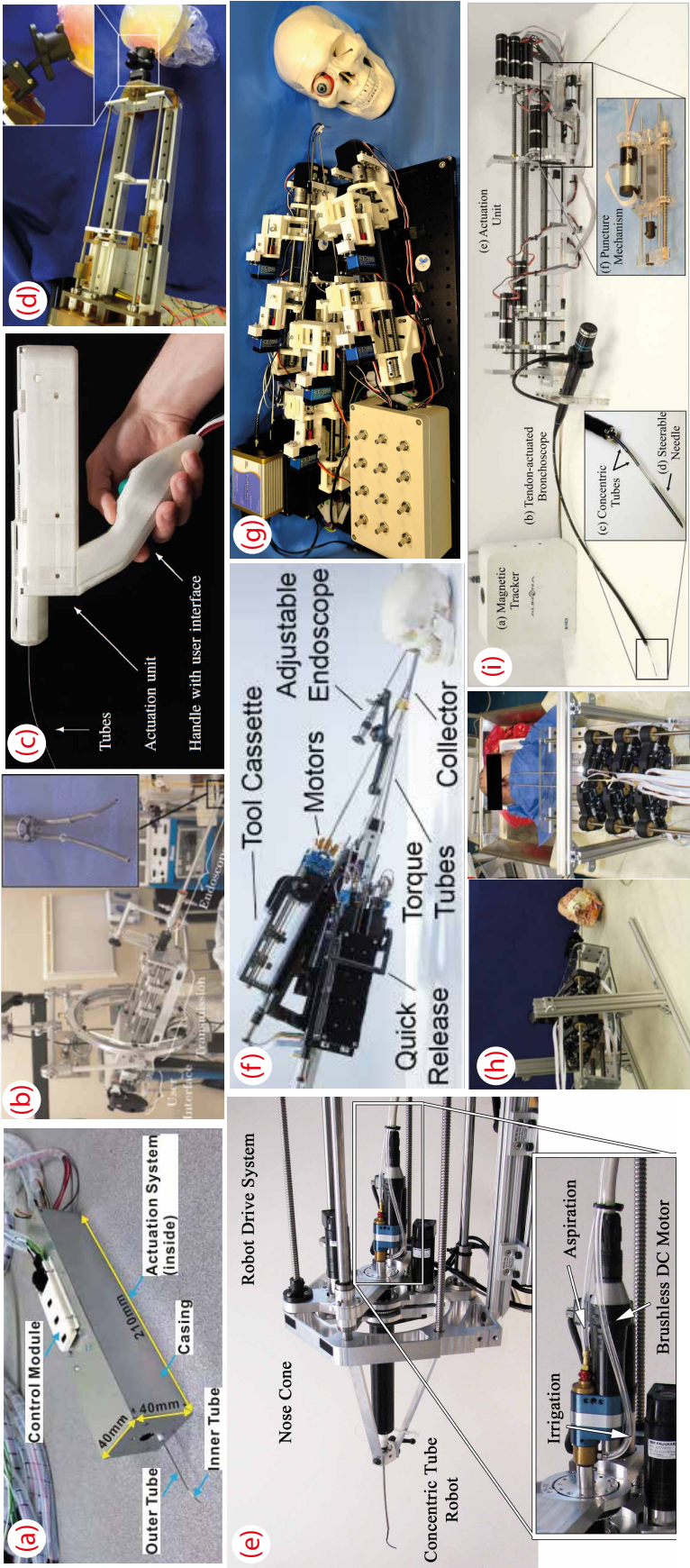
Figure 1.4: Concentric tube robots for various medical applications: a) Light Pipe for Intraocular Procedures ([17]), b) Prostate Surgery ([18]), c) Handheld CTR for MIS ([19]), d) Intracerebral Hemorrhage Evacuation ([20]), e) Intracardiac Surgery ([21]), f) Endonasal Surgery ([22]), g) Deep Orbital Interventions ([2]), h) Endonasal Tumor Removal ([23]) and i) Partial Nephrectomy ([24]).

Burgner *et al.* [20] introduced a sterilisable and biocompatible robot with 3 Degrees of Freedom (DoFs) for intracerebral hemorrhage evacuation shown in Fig. 1.4(d). The prototype was the first reusable, sterilizable, and operating room ready actuation unit for CTRs. All its components were autoclavable and biocompatible, while the motors could be bagged to ensure the sterility of the system. The robot comprised 2 tubes, with the outer one being straight and the inner one having a curved distal end. The inner aspiration tube was interchangeable during the application. The motors could be attached or detached from the transmission through Oldham couplings. Lead screws were used for the translation of the tubes while the rotation of the inner aspiration tube was achieved via a square shaft that interfaced with a gear train. The authors validated the concept by performing experiments using a gelatin phantom. The phantom was placed in an acrylic box and was made from 10% by weight Knox gelatin (Kraft Foods Global, Inc., USA), while clots were made from Jell-O gelatin.

Burgner *et al.* [23] developed a telerobotic system for endonasal skull base surgery. The system comprised two concentric tube arms, made from NiTi, holding a ring curette and a gripper [see Fig. 1.4(h)]. A straight manually operated endoscope was used for visualization. The robotic system also comprised two 6 DoF input devices and an Electro-Magnetic (EM) tracking system. The translation of the tubes was based on the use of a worm gear, which rotates a nut that rides on a stationary lead screw. The worm gear driving the rotation, rotated a spring collet which grasped the base of its respective tube. The robot and the clinical concept were evaluated by performing a mock-up surgery on a human cadaver head. The two manipulators entered the nasal passage of the cadaver through a single nostril to show that they can successfully reach the pituitary gland. An updated system [see Fig. 1.4(f)] included three arms to satisfy real-world surgical workflow requirements, see [22]. Each arm was a single interchangeable tube cassette, which was mounted on any of the four module carriers of a base and was locked by a large handle. The motors were placed outside of the module carriers to reinforce sterility. Tube translation was achieved via lead screws, while spur gears and square shafts

were used for the rotation. The tool module was made of autoclavable and biocompatible materials. Visualization was achieved by a Karl Storz EndoCAMeleon rod lens endoscope with adjustable lens direction. Four additional motors located behind each module carrier translated the modules relative to the robot base, enabling full system insertion or retraction.

Vitreoretinal & Deep Orbital Interventions: CTRs offer compelling solutions to challenging intraocular and orbit surgery, which require dexterous manoeuvres of sub-millimetre surgical tools. The forces that relevant tissues can withstand without damage are minuscule, while the constrained workspace introduces further complications.

The first use of CTRs for vitreoretinal surgery was proposed by [85, 86]. The authors proposed a hybrid robotic system for applications that require fine dexterous manipulation such as Internal Limiting Membrane pealing and treatment of severe retinal detachments. The intraocular part of the robot was a 2 DoF CTR which comprised a precurved NiTi tube that was extended from a straight cannula. The parallel part of the robot provided global precise positing of the surgical instrument inside the eye and manipulation of the eyeball itself. Later on, [87] and [17] developed one-arm CTRs with 4 and 3 DoFs, respectively. The systems were tested on custom-made phantoms while the robot developed by [17] was also evaluated on porcine eyes. These were the first systems wherein the concept of miniaturizing the actuation compartment was considered. Each one of the system's module of [87] measured just 66mm x 52mm x 29.5mm, with a linear travel range of 30mm corresponding to the eye's diameter. The robot comprised two NiTi tubes with the diameter of the outer one being less than 23-gauge (0.6 mm). The inner tube housed a gripper, which comprised steel forceps with a diameter of 300μm welded with a piece of 27-gauge stainless steel tube.

The prototype of [17], shown in Fig. 1.4(a), was 40mm x 40mm x 210mm. The outer tube was in the 20-gauge range, while the inner tube, with a bending radius of 30mm, was less than 23-gauge with an inner diameter sufficient to house a 25-gauge (0.5 mm) light pipe. Hollow shaft motors eliminated the need for gears or

lead screws and avoided backlash. They were controlled by a custom made joystick and buttons on the top side of the robot. The robot was very light, with a total weight of 0.496kg, to enable handheld operation, being the first to be used in this fashion.

In [42], the robotic system first presented in [22] for pituitary tumor removal surgery, was used for the removal of tumours growing behind the eyes in the orbital apex region. The authors integrated a sterile draping concept for non-sterile components, and a cartridge-based tool change approach that eased instruments swaps. The robot was evaluated on a silicone eye phantom housed in a portion of a skull 3D-printed in plastic. Two otolaryncologists performed 10 orbital tumor resections in total while at the same time minimizing unnecessary fat removal. The phantom of the tumor was made from silicone, and ballistics gel was cast to simulate orbital fat and connective tissues. The authors developed a modular solution for the electrical hardware comprising of multiple units with microcontrollers rather than a traditional computer, reducing in this way the cost and size. The distribution of the computational load permits real-time, synchronous and closed-loop position control of the motors. Regarding the surgeon interface console, it was a custom made mobile cart which housed a high-level control computer, two human-machine interfaces (PHANTOM Omni haptic devices, 3DSystems, Inc.) and a 42-inch high-definition monitor. This was the first system that consisted of a complete, clinically practical system that permitted intraoperative interchange of concentric tube instruments.

Fetoscopic Interventions: Fetoscopic interventions are unique in their requirement to protect the welbeing of both the mother and the fetus. Delicate manoeuvres under poor visualisation conditions are required, occasionally with oblique lines of sight. Dwyer *et al.* [88] developed a 2 DoF CTR with primary novelty its coupling to a KUKA LBR iiwa 7 R800 robotic arm constrained by a remote centre of motion (RCM). The robot was designed for Fetoscopic Laser Photocoagulation (FLP), a minimally invasive surgery used to treat Twin-Twin Transfusion Syndrome. The robot was evaluated by scanning a human placenta, via the employ-

ment of a miniature camera (Naneye Stereo Camera, AWAIBA Lda, Portugal) at the robot's tip. The tubes are actuated by servo motors (Dynamixels MX-28) with the use of square shafts and gears for the rotation and lead screws for the translation. The robot was controlled via VxWorks (Wind River Systems Inc., United States) providing a soft real-time system. An updated system was presented in [89]. The mechanism has been improved by the inclusion of linear rails and Oldham couplings while the minimization of the actuation system has been taken into account.

Vandebroek *et al.* [90] showcased a multi-arm CTR for fetal surgery with a focus on spina bifida, which is one of the most common birth defects. The authors were the first to explore the macro-micro concept during the robot's design. The robot comprised four arms housed within a rigid insertion sheath with an outer diameter of 11mm. The robot had 2 mirrored instruments arms, a camera arm (NanEye camera, AWAIBA), and one arm for suction and irrigation. Macromotion was achieved based on concentric tube technology, while the micromotion part was a highly bending segment actuated by a miniaturized fluidic McKibben muscle of 1.2mm outer diameter.

Cardiac Surgery: Heart surgery is an acute procedure usually requiring the cut and spread of the sternum to expose the heart, and a cardiopulmonary bypass to perform the final intervention in a non-beating heart. Interventions on a beating heart obviate the need for the bypass but increase the risk of adverse effects and co-morbidity. CTRs have reported potentially game-changing benefits in heart surgery.

Gosline *et al.* [21, 91] used a CTR prototype, shown in Fig. 1.4(e), to deliver metal microelectromechanical systems (MEMS) to intracardiac locations though the patient's neck to the right atrium of the heart. This work was the first that proposed the use of CTRs as a means to deliver micro-manufactured instruments rather than only as active cannulas or dexterous manipulators. Validation in [92] demonstrated robotic percutaneous beating-heart tissue removal through an *in vivo* atrial septostomy on a Yorkshire swine. Finally, Fagogenis *et al.* [93] demonstrated in a preclinical porcine *in vivo* model autonomous navigation of a CTR inside the heart by ensuring low-force contact with the heart tissue and then following tissue

walls to reach a goal location.

Lung Interventions: CTRs have also been proposed for early detection of lung cancer. While CTRs are compliant robotic systems, they are rigid and cannot safely conform to the human anatomy unless they are patient-specific. To mitigate this, Swaney [94] developed a three-stage steering system for lung biopsy and therapy delivery, shown in Fig. 1.4(i). The system comprised a bronchoscope housing a CTR. The bronchoscope was used to reach the bronchial wall, while the CTR was used to penetrate it, carrying also the tools necessary for a biopsy. The robot was validated on a phantom consisting of a bronchial tree (made from plastic tubes) that was embedded in a phantom parenchyma (gelatin) and on *ex vivo* porcine wall tissue. Amack *et al.* [95] improved the concept of accessing the peripheral lung by designing a more compact, modular, multi-stage robot to retrieve biopsies from lesions in the peripheral regions of the lung. The improved version included a quick-connect mechanism, which allowed the rapid tool interchange employing a similar concept as in [20]. Each tool was pre-configured with a spur gear. The robotic system featured two spring-loaded levers, with adjustable sprint tension to minimize backlash, which were able to deflect to accept the spur gear hub. Finally, the new design featured the first precise, systematic homing protocol to acquire a repeatable home position for all DoFs of the robot achieving a homing precision with a standard deviation of $\pm 7.3 \mu$m and $\pm 0.09°$.

Prostate Surgery: Transurethral laser prostate surgery was studied in [18]. CTRs were developed to facilitate holnium laser enucleation of the prostate (HoLEP), which currently is a very challenging procedure. The authors demonstrated the use of a robotic system with two concentric tube manipulators housed within a rigid endoscope, as shown in Fig. 1.4(b). The hand-held system was suspended from a spring-loaded counter balanced boom arm. The two manipulators possessed 9 DoFs in total with one of them comprising three precurved tubes (6 DoFs) while the other included two tubes with the outer one being straight (3 DoFs). One arm facilitated tissue manipulation and retraction while the other aimed the laser fiber. The linear motion of the tubes was achieved via lead screws which drove

tube carriers on ball screws, while rotation was achieved via square shafts, which transmitted torque through a gear train to each tube. A key innovation of the work was that the user teleoperated the concentric tube arms using joysticks mounted on the system itself. The system has been demonstrated through phantom and cadaver experiments on a procedure for benign prostatic hyperplasia.

Motorised Systems for MIS: In the interest of brevity, we do not discuss in detail all the systems developed solely for evaluation of the theoretical works. However, systems presenting a novel design and have not been presented above are discussed here.

Girerd *et al.* [19] designed a hand-held CTR, shown in Fig. 1.4(c), for MIS which can provide increased accessibility and dexterity as large robotized devices while maintaining the footprint of a traditional hand-held tool. The robot comprised 3 NiTi tubes while roller gears for the simultaneous rotation and translation of a tube, creating a lightweight and easy to assemble system. It was controlled via a symmetric hand held interface which enabled single-hand operation. Also, [96] designed the first 3D printed CTR weighted 490 gr and with dimensions 17.5in×3.5in×4*in*. The robot was composed of 3 tubes and 6 DoFs in total. It demonstrated through experiments the precision and accuracy that a 3 tube system can have. Childs *et al.* [84] presented the first continuum robot based on a pair of concentric precurved bellows. Each bellow rotated axially at its base, allowing independent control of the end-effector's curvature and bending plane. The authors developed a 3D printed system as a proof of concept and performed experiments to demonstrate payload capacity and validate their theoretical work. It was the first proposition of a continuum robot based on concentric tube technology able to be used as a soft gripper and generally in non medical application.

Table 1.2: Concentric Tube Robots & Systems in Literature

Reference	Pathology/Application	Test on	Arms	DoFs	Motors	Encoders
[93]	Intracardiac Beating Heart	Porcine heart	1	7	Faulhaber & Stepper	N/A
[18]	Prostate	Custom made phantom	1	9	Brushless motors	N/A
[17]	Intraocular	Phantom & Porcine eye	1	3	Stepper Motors	N/A
[94]	Transoral Lung Access	Phantom & Porcine tissue	1	5	Maxon Motor, Inc.	N/A
[97]	Endonasal	Cadaver & Phantom	2	12	DC Motors	Motor's Encoders
[98]	Endonasal	-	4	24	DC motors with	Motor's Encoders
[22]	Endonasal	-	3	3*6+4	Brushless motors	Motor's Encoders
[99]	Neurosurgical	Test of controller	1	5	-	-
[100]	Neuroendoscope	Silicon Phantom	2	10	DC Maxon motors	Potentiometers & Motor's Encoders
[101]	Image-guided neurosurgery percutaneous interventions	Phantom	1	6	Firgelli linear actuators Piezoelectric actuators	Optical
[87]	Vitreoretinal	Phantom	1	4	DC Motors	Potentiometers
[20]	Intracerebral Hemorrhage Evacuation	Phantom	1	3	Maxon Motors	Optical Tracker
[102]	Deep Anterior Brain Tumor	On air	1	6	Maxon Motors	Optical
[103]	Transnasal Nasopharyngeal Carcinoma	Cadaver Experiment	3	14	Stepper Motors	Motor's Encoders
[88]	Fetal Surgery	Human placenta	1	2	Dynamixel MX-28 motors	Motor's Encoders
[90]	Fetal Surgery	Theor. Eval.	3	2	Fluidic McKibben Muscles	N/A
[104]	Transnasal surgery	Cadaveric studies	1	4	Stepper motors	N/A
[95]	Transbronchial Lung Biopsy	Phantom	1	8	Brushless DC motors	Motor's Encoders optical photointerruptors rotational reflective sensors
[2]	Optic Nerve Sheath Fenestration	Phantom & Porcince Eyes	3	3*4	Servo motors	Potentiometers
[105]	Neurosurgical MIS	Phantom	1	6	Stepper motors	N/A
[106]	Rigid Neuroendoscopy	Phantom	2	8	Brushled DC motors	Hall & magnetic sensor
[107]	Nasopharyngeal carcinoma	Phantom	3	16	Stepper motors	N/A
[108]	Theoretical Evaluation	Open-source simulator Origami tunnel	1	3	Stepper Motors	N/A
[59]	Theoretical Evaluation	Load & Force exp.	1	4	Manual Actuation	-
[84]	Theoretical Evaluation	Object	1	3	Manual Actuation	Camera & Stylus pointer
[109]	Theoretical Evaluation	Free space	1	6	OWIS GmbH	Tip Camera
[110]	Theoretical Evaluation	Phantom & FEM	1	4	Dynamixel & Maxon motors	Telecentric lens
[111]	Theoretical Evaluation	Free space	1	6	Maxon Motors	Motor's Encoders
[50]	Theoretical Evaluation	Trajectory tracking	1	3	Zaber motors	N/A
[96]	Theoretical Evaluation	Accuracy & Precision testing	1	6	DC Micro Metal motors	Quadrature encoder
[112]	Theoretical Evaluation	Target capture	1	4	Servo motors	Motor's Encoders
[113]	Theoretical Evaluation	Workspace Coverage	1	4	N/A	N/A

1.4.3 Summary of CTR Applied Research in Medicine

Design variables that should be considered when designing a CTR are determined by the application that the robot will be used on. They include the diameter of the manipulator, the number of tubes, the material, the curvature and the stiffness of each tube. The DoFs that the robot should possess, the output force range, the type of transmission which affects the friction and the backdrivability of the system should be taken into account as well.

CTRs can either be a standalone robotic system or part of a hybrid system based on the required DoF and the aimed intervention. Most CTRs are standalone systems to take advantage of the miniature end-effector and the increased curvature they can possess. On the other hand, the use of hybrid systems, e.g. combining either a parallel robot or a flexible catheter with a CTR can cancel out the drawbacks of each technology in the expense of a more complex actuation system.

Several challenges should be addressed prior to the employment of CTRs in the clinical setting. Safety during an intervention is one of the most important requirements. The employment of several sensors and the use of the robot by an experienced surgeon can minimize the risk of complications. Moreover, the size and the placement of a robot in the operating room should not intervene with the surgical procedure as the space in an operating room is limited. CTRs can be mounted either on robotics manipulators or on passive articulated arms, which can be placed aside when they are not needed. Works on the miniaturization of CTRs and the surgical tools are taken place so to minimize their hardware footprint.

Remarks on the design of CTRs based on the prototypes that are presented above can be summarized to the fact that components should be biocompatible and tools should be interchangeable. The sterility of the system should be taken into consideration if the ultimate goal is to deploy robots in the operating room. This can be achieved by biocompatible materials and bagging the motors when they are close to the surgical area. Furthermore, the ability of the system to possess a miniature camera at its end-effector to visualize the surgical area is critical when visualisation through other modalities is not possible. Finally, the research trend is to consider

multi-arm systems because of the need to manipulate tissue and deliver more than one tools at the same time in the surgical area.

1.4.4 Fabrication Techniques

CTRs are mostly made from NiTi due to its super-elastic capabilities. NiTi tubes can be precured using heat treatment either via the employment of a furnace [2] or via an electric technique that uses Joule heating [46].

To shape setting NiTi tubes via an electric furnace in [2], an aluminum template (Al 2219) with grooves of the desired curvature was machined. It was experimentally found that the template should be preheated to $520°$ for approximately $10\,\mathrm{mins}$ to ensure its uniform heating when the tubes are inserted. Next, the tubes were inserted in the preheated template and the assembly was inserted in the oven at $510°$ - $514°$ steady state temperature for $30\,\mathrm{mins}$. Afterwards, the template with the tube was rapidly quenched in cold water for immediate cooling. Reliable shape setting was observed for curvatures ranging from 14.5 to $285.7\,\mathrm{m}^{-1}$, and diameters from 1 to $2.8\,\mathrm{mm}$.

To decrease the manufacturing time, overall cost, and also achieve higher accuracy on precurvature setting without the presence of relaxation, an electric technique that uses Joule heating was proposed in [46]. A complete system for closed loop, high temperature resistance heating of NiTi tubes was presented. The template was made of inexpensive medium density fiberboard (MDF) and an Arduino microcontroller board was employed to regulate the on-off state of the measured resistance of the heated part while a MOSFET is used to control the flow of current, commanded by the microcontroller. The designed system was evaluated on shape setting 10 wires with a target radius of curvature of $r = 63.7$ mm. The mean radius of curvature of the resulting wires was 65.1 mm with a standard deviation of 1.7 mm.

1.5 Structural Design & Optimization

Specific surgical tasks and the anatomical environment impose constraints on the design of a CTR end-effector. Design methodologies and optimization frame-

works have been developed to tailor the workspace, dexterity and task specificity of CTRs prior to an intervention. Computational design methods aim to maximise performance metrics, such as manipulability, stiffness, and stability, by fine tuning characteristics, such as tube diameters, lengths, and curvatures through constrained optimisation. Constraints may include the requirement to avoid contact with the anatomy, limit the approach angle of the robot to vessels, or push for a reduced overall length and curvature. The state-of-the-art on computational CTR design methods is summarised in Table 1.3.

Early research was presented in [114, 115]. Anor *et al.* [114] presented a systematic approach to optimize the design of CTRs for neurosurgical procedures with a focus on endoscopic choroid plexus ablation. This method for the first time identified the need for either fixed-curvature versus variable-curvature sections, while in [115] the notion of robot navigation and manipulation sections were presented. In both works, Global Pattern Search Optimization determined the length and curvature of each tube to reach multiple targets while avoiding contact with brain ventricles and heart wall, and minimizing tubes' length and curvature.

An unconstrained nonlinear simplex search method in a skull base surgery scenario for the minimization of the unreachable points was presented in [97], where the authors introduced the concept of volume-coverage in robot design instead of specific point reachability. A torsionally rigid robot kinematic model was considered. An optimal cannula tube design was acquired when the end-effector's tip was within the desired working volume. In [116], the authors provided an in-depth discussion on the idea of volume-based design. They advanced their previous work by using a mechanics-based model which included torsional compliance and incorporated workspace constraints related to the robot's entry path in approaching the surgical site. Moreover, the authors introduced a new volume-based optimization metric that penalized voids in the robot's workspace. In similar vein, [117] added the number of tubes, apart from the curvature, in the design process. The authors employed a brute force and greedy algorithm to maximize workspace coverage for intracerebral hemorrhage evacuation. A generalization of the previous works was

presented in [118]. The authors proposed a novel computer-assisted design process which decomposes the problem into task- and robot-specific design optimizations. The method was based on a multi-objective particle swarm optimization algorithm with variable length. The authors used the scenario of laser-induced thermotherapy in the brain to validate their method. The robot-specific design process determined the tube curvature and length of the CTR end-effector as well as different configurations. The proposed algorithm was evaluated on real patient datasets.

Inspired from path-planning, Torres et al. [119] employed a rapid exploring random tree (RRT) to acquire CTR designs to reach multiple sites within the bronchial tubes while avoiding the anatomy. The method included for the first time the notion of design coherence, which is based on the observation that collision-free configuration spaces of robots of similar design are also similar. It was the first work to incorporate mechanics models with torsional compliance.

Bergeles *et al.* [120] introduced the elastic stability of CTRs in the design optimisation by including heuristics that maximize robot stability. The effect of section type (variable or fixed curvature) on the boundaries of the workspace was discussed in detail and affected the design methodology and optimization method. Nelder-Mead Downhill Simplex was used as an optimisation algorithm, and explored the scenarios of hydrocephalus treatment and beating heart surgery in simulation.

The work of Yang *et al.* [105] introduced the number of tubes as an additional optimization variable, along with tubes' curvature. They introduced geometry-based kinematics in CTR design, which significantly reduced the computational time. The geometry-based method estimated continuous circular curves while intermediate nodes, derived from the desired trajectory, determined the number and type of subsections that the final design of the CTR comprised. The authors implemented a mesh adaptive direct search for the optimal design. Their optimal design was defined as retaining the maximum distance from the organs as it followed a provided trajectory, and had to incorporate the smallest number of tubes.

It should be noted that all the works mentioned above on the design of a CTR are based on optimization variables and functions that the designer has decided to

Table 1.3: Computational CTR Design. The optimization variable L stands for the tube's length while κ stands for tube's curvature.)

Name	Method	Obj. Function	Opt. Variables
[114]	Global Pattern Search (GPS) Optimization Method	1) Min(L & κ) 2) Reach multiple targets 3) Obstacle Avoidance	L & κ
[115]	Global Pattern Search	1) Min(L & κ) 2) Obstacle Avoidance 3) Reach all targets	L & κ
[97]	Unconstrained Nonlinear Simplex Search Method	Min(unreachable points)	L & κ
[119]	Rapidly Exploring Random Tree (RRT)	1) Reach multiple targets 2) Obstacles avoidance	L & κ
[116]	Nelder-Mead Simplex Algorithm	Max(Workspace Coverage)	L & κ
[68]	Study of the Monotony	Max(Stability)	Precurvature funtion
[121]	Adaptive Simulated Annealing (ASA) & RRT	Max(Workspace)	L & κ
[120]	Nelder-Mead Downhill Simplex Method	1) Anatomical Constraints 2) Stability 3) Workspace	Number of Tubes Bending Stiffness & κ
[102]	Pareto Grid Searching Method	Reachability Elastic Stability	L & κ
[113]	fminsearch	Max(Workspace Coverage)	-
[117]	Brute Force & Greedy Algorithms	Max(Workspace Coverage)	Number & Type of Aspiration Tube
[122]	Steepest Descent	Max(Stability)	Combined precurvature
[123]	Particle Swarm Optimization	Max(Collaborative Configurations)	L & κ
[118]	Multi-Objective Particle Swarm Optimization	1) Max(Tumor's Coverage) 2) Min(ablation overlap)	Ablation objects L & κ
[105]	Mesh Adaptive Direct Search	1) Min(Number of tubes) 2) Max(Distance from organs) 3) Follow Trajectory	Number of Tubes & κ

implement in their method with little-to-no surgeon input to the final design. In some works, e.g., [114, 66, 118], a surgeon can select the initial entry point/vector and constraints for the initial configuration, but their vast knowledge of the patient anatomy and procedure is not fully leveraged. Morimoto *et al.* [124] created a surgeon design interface to design a CTR for a specific patient and procedure so to enable the surgeon to give more input into the design. The intuitive interface allowed the user to see the anatomical model of interest in 3D and initialize a CTR design by setting a number of via points. The user could alter individual tube parameters until the desired configuration was acquired. Moreover, the interface allowed the user to explore the environment and simulate CTR's motion through the body.

Design algorithms are not the only way to acquire optimal CTR designs. To minimize the effect of instability, methods for anisotropic patterning of tubes have been studied. Several works and experimental results have shown the promising employment of patterned tubes to achieve higher curvatures while eliminating the problem of snapping. Azimian et al. [125] explored the use of a cellular tube to minimize the ratio of bending-to-stiffness ratio (BTSR). Simulations using finite element analysis derived the optimal design of the cell geometry via trial-and-error. Experiments using the derived optimal design showed that a patterned tube can exhibit a smooth rotation without snap-through motion. Lee et al. [126] improved previous work by building a lumped analytical model and examining it with finite-element analysis (FEA) and providing an in-depth discussion on patterning of NiTi tubes. The developed experimental system shows that the tubes' patterning can eliminate snapping and decrease the BTSR ratio. Similarly, Kim et al. [110] studied the creation of a nonuniform pattern on coaxial tubes to enhance stiffness of a CTR via a continuously variable stiffness mechanism. The stiffness change was validated via analytical modeling, FEM simulation studies, and experimental results all of which showed an increase in stiffness. Finally, Luo et al. [127] employed for the first time topology optimization methods to acquire the optimal design of patterning so to decrease the BTSR and resolve the snapping problem. The developed method was validated through FEA as well as experimental testing.

Remarks & Limitations: Methods for computing optimal CTR designs to reach specified positions have been derived by employing different optimization algorithms and taking into account different design variables. Also, topology optimization methods and FEA have been used to derive optimal designs with enhanced stability and stiffness. However, a unified framework taking into account all possible design variables and requirements has not yet been released nor deployed in a real case scenario.

Moreover, new design variables can be included in future optimization methods. Design variables can include metrics used in control e.g force/ velocity manipulability [111] or characteristics such as triangulation [123] that describe coop-

eration in the case of multi-arm systems. These metrics can also be employed as a unified comparison metric despite the fact that the community unofficially uses the error per unit length to compare ones' work to the state of the art. End-effector's stiffness and anisotropy is a possible candidate for future design optimization algorithms as there are limitations on the diameters of tubes that can be manufactured. In addition, tissue properties should really be taken thoroughly into consideration. Finally, a general analytical model for optimal patterning designs has yet to be derived.

1.6   Conclusion

Over the last decades, CTRs have matured from a relatively niche area of research to the point where modelling accuracy, control, system design, and application have showcased impressive outcomes. Nevertheless, there are still gaps in the state of the art that should be addressed prior to usage of such a system to human.

A CTR and a continuum robot in general should be designed based on a specific application and take into account the appropriate clinical requirements. Many interventions require bimanual manipulation of tools and the necessity to visualize them and the surgical area of interest. Multi-arm systems promise to offer the necessary number of DoF to satisfy these needs while at the same time offer increased flexibility and dexterity.

In the next chapters, new designs of continuum robots are suggested to access deep seated pathologies. For each proposed design option, a prototype with the corresponding new modelling theory is employed to validate the concept. This dissertation aims to take advantage of the literature review to propose the new design options for two surgical applications.

Chapter 2

Mathematical Background

In this chapter, the mathematical background used throughout this dissertation is presented. The theoretical work developed and discussed in Chapters 4, 5, and 6 and briefly mentioned in Chapter 3 is based on classical solid mechanics principles and Cosserat-rod theory. Here, a concise overview of the mathematical background needed for the development of the required models is given as well as a model for the exact prediction of the shape of CTRs is presented [35]. The following notation is used: x, $\mathbf{x}$, and $\mathbf{X}$ denote a scalar, a vector, and a matrix, respectively. The dot notation i.e. $\dot{x}$ denotes derivatives with respect to spatial coordinate s.

2.1 Kinematic Model of a Rod

2.1.1 Geometric Representation of a Rod

The position and orientation of a rod are functions related to the scalar reference length parameter s over the finite interval $s \in [0\ \ l]$ where l is the rod's length. The shape of a rod can be defined as a parametric curve in Cartesian space, $\mathbf{p}(s) \in \mathbb{R}^3$, paired with a Bishop frame, $\mathbf{R(s)} \in SO(3)$, attached to every point along its arclength, with the z-axis of the frame remaining tangent to the curve. This convention is expressed as:

$$\mathbf{R}(s)e_3 = \frac{\dot{p}(s)}{\|\dot{p}(s)\|}, \tag{2.1}$$

where $\mathbf{e_1}, \mathbf{e_2}$, and $\mathbf{e_3}$ are the standard basis vectors $[1\ 0\ 0]^T$, $[0\ 1\ 0]^T$ and $[0\ 0\ 1]^T$.

The homogeneous transformation matrix describing the shape of the entire rod

is $\mathbf{g}(\mathbf{s}) \in SE(3)$:

$$\mathbf{g}(s) = \begin{bmatrix} \mathbf{R}(s) & \mathbf{p}(s) \\ 0_{3x1}^T & 1 \end{bmatrix}. \tag{2.2}$$

A rod can undergo deformation due to external forces and/or moments. The undeformed shape of a rod, which will be also referred as initial reference frame, is defined as:

$$\mathbf{g}^*(s) = \begin{bmatrix} \mathbf{R}^*(s) & \mathbf{p}^*(s) \\ 0_{3x1}^T & 1 \end{bmatrix}. \tag{2.3}$$

The * symbol denotes variables related to the initial reference frame.

2.1.2   Differential Geometry of a Rod

It is known that $\mathbf{R}(s)^T \dot{\mathbf{R}}(s) \in \mathfrak{so}(3)$ is the Lie algebra of Lie group SO(3) and is expressed as a 3x3 skew symmetric matrix while the $\hat{}$ depicts the mapping from $\mathbb{R}^3$ to $\mathfrak{so}(3)$. For example, for a vector $\mathbf{u} = [u_x\, u_y\, u_z]^T \in \mathbb{R}^3$ the skew symmetric matrix is:

$$\hat{\mathbf{u}} = \begin{bmatrix} 0 & -u_z & u_y \\ u_z & 0 & -u_x \\ -u_y & u_x & 0 \end{bmatrix}. \tag{2.4}$$

The inverse operation i.e. the mapping from $\mathfrak{so}(3)$ to $\mathbb{R}^3$ is denoted by $\check{}$.

In a similar way, the $\mathbf{g}(s)^{-1}\dot{\mathbf{g}}(s) \in \mathfrak{se}(3)$ is the Lie algebra of Lie group SE(3). For a vector $\boldsymbol{\xi}(s) = [v_x\, v_y\, v_z\, u_x\, u_y\, u_z]^T \in \mathbb{R}^6$ the skew symmetric matrix is:

$$\hat{\boldsymbol{\xi}} = \begin{bmatrix} 0 & -u_z & u_y & v_x \\ u_z & 0 & -u_x & v_y \\ -u_y & u_x & 0 & v_z \\ 0 & 0 & 0 & 0 \end{bmatrix}. \tag{2.5}$$

The twist vector $\boldsymbol{\xi}$ represents the rate of change of $\mathbf{g}(s)$ with respect to s expressed in coordinates of $\mathbf{g}(s)$. The first three components of $\boldsymbol{\xi}(s)$ represent a vector of linear rates of change, $\upsilon = [v_x\, v_y\, v_z]$, while the last three represent a vector of angular rates of change, $\mathbf{u} = [u_x\, u_y\, u_z]$. If the twist vector $\boldsymbol{\xi}(s)$ and an initial frame $\mathbf{g}(0)$

are known, then the remaning frames can be obtained by integrating the following differential equation:

$$\dot{\mathbf{g}}(s) = \mathbf{g}(s)\hat{\boldsymbol{\xi}}(s), \tag{2.6}$$

or equivalently:

$$\dot{\mathbf{r}}(s) = \mathbf{R}(s)\mathbf{e}_3, \ \dot{\mathbf{R}}(s) = \mathbf{R}(s)\hat{\mathbf{u}}(s). \tag{2.7}$$

Equations (2.6)-(2.7) are solved, in most of the cases, employing numerical integration as the twist vector is not constant with respect to s.

2.1.3 Mechanics of a Rod

To derive the equilibrium equations for a Cosserat rod, the notation and methodology presented in [128] are employed. Taking an arbitrary section from c to s of the Cosserat rod shown in Fig. 2.1 , the static equilibrium dictates that:

$$\mathbf{n}(s) - \mathbf{n}(c) + \int_c^s \mathbf{f}(\sigma)d\sigma = 0 \tag{2.8}$$

$$\mathbf{m}(s) + \mathbf{p}(s) \times \mathbf{n}(s) - \mathbf{m}(c) - \mathbf{p}(c) \times \mathbf{n}(c) + \\ \int_c^s (\mathbf{p}(\sigma) \times \mathbf{f}(\sigma + l(\sigma)))d\sigma = 0, \tag{2.9}$$

in which $\mathbf{m}(s), \mathbf{n}(s)$ are the internal moments and forces respectively that the material of $(s, l]$ exerts on $[c, s]$ while $\mathbf{m}(c), \mathbf{n}(c)$ are the internal moments and forces respectively that the material of $[c, s]$ exerts on $[0, c)$. Also, $\mathbf{f}, \mathbf{l}$ are the applied force and moment distribution per unit of s respectively.

Taking the derivative of (2.8)-(2.9), the evolution of $\mathbf{m}$ and $\mathbf{n}$ is described as:

$$\dot{\mathbf{n}}(s) + \mathbf{f}(s) = 0 \tag{2.10}$$

$$\dot{\mathbf{m}}(s) + \dot{\mathbf{p}}(s) \times \mathbf{n}(s)\mathbf{l}(s) = 0. \tag{2.11}$$

2.1.4 Constitutive Laws

Constitutive stress-strain laws relate the kinematic variables $\boldsymbol{v}, \mathbf{u}$ to the internal loads $\mathbf{m}, \mathbf{n}$. They also express the difference between the undeformed state of a
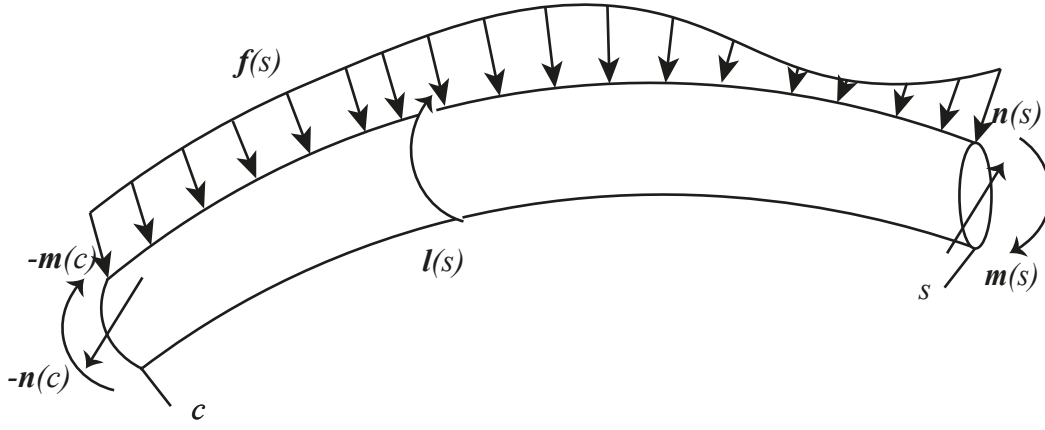
Figure 2.1: Arbitrary section of a Cosserat rod from c to s under external force. The internal forces and moments are shown at both ends of the rod.

rod to the deformed one. The most used constitutive law is a linear relationship which assumes that the x and y axes of $\mathbf{g}^*$ are aligned with the principal axes of the cross section. Employing this assumption, one have:

$$\mathbf{n}(\mathbf{s}) = \mathbf{R}(s)\mathbf{K}_{se}(s)(\boldsymbol{v}(\boldsymbol{s}) - \boldsymbol{v}^*(\boldsymbol{s})), \tag{2.12}$$

$$\mathbf{m}(\mathbf{s}) = \mathbf{R}(s)\mathbf{K}_{bt}(s)(\mathbf{u}(\mathbf{s}) - \mathbf{u}^*(\mathbf{s})), \tag{2.13}$$

where $\mathbf{K}_{se}(s), \mathbf{K}_{bt}(s)$ are stiffness matrices. The subscript $[.]_{se}$ denotes shear and extension while $[.]_{bt}$ denotes bending and torsion. The stiffness matrices for a rod with Young's modulus E, shear modulus G, area of the cross section A, second area of the tube cross section about the principal axes I_{xx}, I_{yy} are:

$$\mathbf{K}_{se}(s) = \begin{bmatrix} GA & 0 & 0 \\ 0 & GA & 0 \\ 0 & 0 & EA \end{bmatrix}, \tag{2.14}$$

$$\mathbf{K}_{bt}(s) = \begin{bmatrix} EI_{xx} & 0 & 0 \\ 0 & EI_{yy} & 0 \\ 0 & 0 & GI_{zz} \end{bmatrix}, \tag{2.15}$$

where $I_{zz} = I_{xx} + I_{yy}$ is the polar moment of inertia.

2.1.5 Model Equations

Collecting all the equations presented above, a rod can be described in static conditions via a full set of differential equations as:

$$
\begin{aligned}
\dot{\mathbf{r}}(s) &= \mathbf{R}(s)\mathbf{e}_3 \\
\dot{\mathbf{R}}(s) &= \mathbf{R}(s)\hat{\mathbf{u}}(s). \\
\dot{\mathbf{n}}(s) &= -\mathbf{f}(\mathbf{s}) \\
\dot{\mathbf{m}}(s) + \dot{\mathbf{p}}(s) \times \mathbf{n}(s)\mathbf{l}(s) &= 0.
\end{aligned}
\tag{2.16}
$$

with the constitutive equations to relate internal loading to strains to be:

$$
\begin{aligned}
\mathbf{n}(\mathbf{s}) &= \mathbf{R}(s)\mathbf{K}_{se}(s)(\boldsymbol{v}(\boldsymbol{s}) - \boldsymbol{v}^*(\boldsymbol{s})), \\
\mathbf{m}(\mathbf{s}) &= \mathbf{R}(s)\mathbf{K}_{bt}(s)(\mathbf{u}(\mathbf{s}) - \mathbf{u}^*(\mathbf{s})),
\end{aligned}
\tag{2.17}
$$

To solve the differential equations describing a rod, boundary conditions are employed. The boundary conditions for a rod clamped at $s = 0$ and under external loads $(\mathbf{F}_{s=L}, \mathbf{M}_{s=L})$ are:

$$
\begin{aligned}
\mathbf{R}(0) &= \mathbf{R}_0 \\
\mathbf{r}(0) &= \mathbf{r}_0 \\
\mathbf{m}(L) &= \mathbf{M}_L \\
\mathbf{n}(L) &= \mathbf{F}_L
\end{aligned}
\tag{2.18}
$$

2.2 CTR Quasi-static Model

Here, a brief summary of the CTR model first presented in [34, 35] is shown.

The CTR tubes are modelled as long, slender, one-dimensional Cosserat rods endowed with a continuous homogeneous transformation matrix attached to every point on its arc. The shape of each tube is determined by the position vector $\mathbf{r}(s) : [0, \ell] \to \mathbb{R}^3$, where the coordinate $s \in [0, \ell]$ is the arc length, and ℓ is the tube's length. The rotation matrix of the frame moving along the tube's arc is $R(s) : [0, \ell] \to SO(3)$, representing orientation change and twisting along s. The constitutive equation for calculating the instantaneous curvature of the tubes and the overall robot shape are
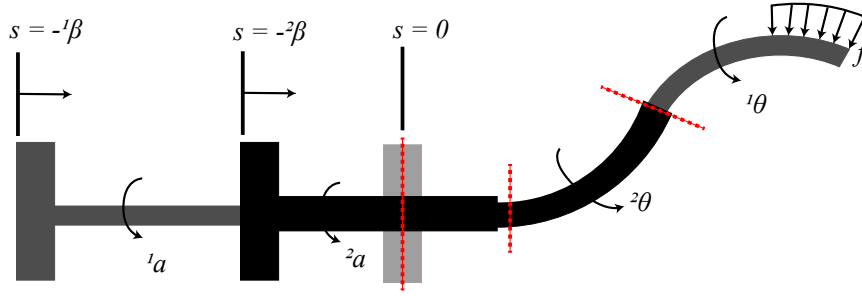
Figure 2.2: Model of a concentric tube robot. Tubes are grasped at their respective prox-
imal ends. The actuation variables $\alpha^i(t)$ and $\beta^i(t)$ denote the proximal base
rotation and translation of the i-th tube, respectively. Each tube comprises a
straight and a curved part. Angular displacement of tube i at arclength s is
denoted by $\theta^i(s)$.

derived according to [34, 35]. The shape of the robot is derived by computing the
shape of the segments that it is composed of. Those segments are identified by
splitting the robot at transition points which model the position where the curvature
or the number of the tubes changes. At those points, the continuity of shape and
internal moment must be enforced (transition points are shown by dashed lines in
Fig. 2.2). To find the deformed shape of all the tubes, it should also be taken into
account that at a given time t they must be equal to the curve of a referred tube
$\mathbf{r}^i(s)$. Considering the rotation of the tubes, the angle $\theta^i(s)$ is employed which
parameterizes the tubes' twist around z axis following the guidelines introduced in
[34]. Finally, based on these assumptions, in the absence of external torques, the
curvature of tubes is found as follows

$$\dot{\mathbf{r}}^1 = \mathbf{R}^1 \mathbf{e}_3, \tag{2.19a}$$

$$\dot{\mathbf{R}}^1 = \mathbf{R}^1 \hat{\mathbf{u}}^1, \tag{2.19b}$$

$$\dot{\mathbf{u}}_1 \Big|_{x,y} = -\mathbf{K}^{-1} \sum_{i=1}^{n} \mathbf{R}_{\theta_i} \Big(\mathbf{K}_i \big(\dot{\theta}_i \frac{d\mathbf{R}_{\theta_i}^T}{d\theta_i} \mathbf{u}_1 - \dot{\mathbf{u}}_i^* \big) + \hat{\mathbf{u}}_i \mathbf{K}_i (\mathbf{u}_i - \mathbf{u}_i^*) \Big) \Big|_{x,y}$$

$$- \mathbf{K}^{-1} \big(\mathbf{e}_3 \times \mathbf{R}_1^T \int_S \mathbf{f}_s(\sigma) d\sigma + \mathbf{R}_1^T \mathbf{l} \big) \Big|_{x,y}, \tag{2.19c}$$

$$\dot{u}_{i,z} = \dot{u}_i^* + \frac{(EI)_i}{(GJ)_i} (u_{i,x} u_{i,y}^* - u_{i,y} u_{i,x}^*) + \frac{\dot{G}_i I_i}{G_i J_i} (u_{i,z}^* - u_{i,z}) - \frac{1}{G_i J_i} \mathbf{e}_3 \mathbf{R}_i^T \mathbf{l}. \tag{2.19d}$$
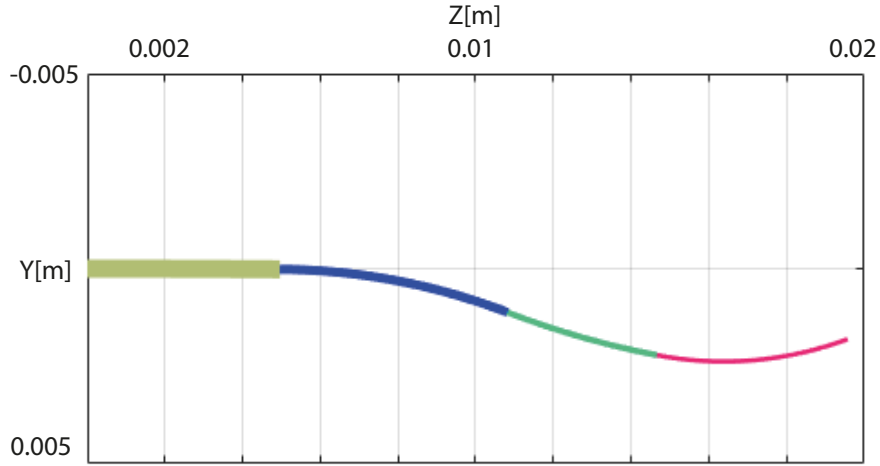
Figure 2.3: A CTR comprising four NiTi tubes. Each tube has a specific precurvature. The shape of the CTR is predicted employing the presented modelling theory.

where subscript $i = 1, \cdots, N$ denotes the i-th tube, with $i = 1$ corresponding to the innermost tube; $\mathbf{e}_3 = [0, \ 0, \ 1]^T$ is the unit vector aligned with the z-axis of the global coordinate frame; $\mathbf{u}_i^*$ denotes the precurvature of each tube in its reference configuration; $\mathbf{K}_i = \mathrm{diag}((EI)_i, (EI)_i, (GJ)_i)$ is the stiffness matrix for tube i; E is the tube's Young's modulus; I is the second moment of inertia; G is the shear modulus; J is the polar moment of inertia; f is any external force applied to the robot. Please note that the (s) notation was dropped for simplicity.

The boundary conditions can be specified in terms of tube curvature and the actuators' values as follows:

$$
\begin{aligned}
\mathbf{r}_1|_{s=0} &= [0\ 0\ 0]^T, & \mathbf{R}_1|_{s=0} &= \mathbf{R}_1|_{z(\alpha_1 - \beta_1 u_{1_3})}, \\
\theta_i|_{s=0} &= \alpha_i - \beta_i u_{i3}, & \mathbf{u}_i|_{s=\ell_i+\beta_i} &= \mathbf{u}_i^*,
\end{aligned}
\tag{2.20}
$$

where the notation $(|_{s=\xi})$ indicates the value of a variable at arclength of ξ, and ℓ_i is the length of the i-th tube. Solving (2.19) and (2.20) gives the robot backbone curvature and shape. The Boundary Value Problem (BVP) is solved using any optimization function.

Figure 2.3 shows the shape of a CTR comprising four NiTi tubes with a unique precurvature for each tube. The shape of the robot is predicted solving (2.19) and (2.20).

2.3 Conclusion

Cosserat rod theory has attracted increased interest in the recent years by several research groups working on continuum robots despite the fact the Cosserat brothers derived their theory of elasticity at the turn of the 1900s [128]. Thanks the to accuracy that it provides, it has been employed in the modelling of CTRs too [35]. In the next chapters, Cosserat rod theory is employed and previous theoretical works are extended to model a multi-arm CTR and a hybrid continuum robot.

Chapter 3

Deep Orbital Interventions with a Multi-Arm Continuum Robot

This chapter describes the development of a robotic system for deep orbital interventions with a focus on Optic Nerve Sheath Fenestration (ONSF). The developed robot comprises three concentric tube robot arms, each one able to hold a different surgical tool. In the design of the system, the clinical requirements of ONSF are taken into account to reach/navigate the optic nerve. Here, a prototype of the robot is presented, and its ability to penetrate the optic nerve was analysed by conducting *ex vivo* experiments on porcine optic nerves and comparing their stiffness to human ones. Also, the robot was successfully deployed in a clinical scenario using a custom-made realistic eye phantom.

The majority of this chapter is adapted from a paper published in the *Robotics and Automation Letters* and *IEEE/RSJ Int. Conf. on Intelligent Robots and Systems* in 2020 entitled "Optic Nerve Sheath Fenestration with a Multi-Arm Continuum Robot" [2].

The primary contributions of this chapter are: 1) the first suggestion of robotic ONSF in the literature for which a prototype is developed, 2) an end-to-end methodological design and validation procedure and 3) evaluating the robot performance in cannulating porcine eye *ex vivo*, given the lack of published data on ONSF force requirements. The validation procedure includes the design and fabrication of a high-fidelity eye phantom on which the robotic system was tested on, system modeling,

computational analysis and experimental validation of the reachable workspace. Moreover, the robot was evaluated by performing *ex vivo* tests and mock surgery on the high-fidelity eye phantom, and theoretically via the employment of a mechanics based model.

3.1   Clinical Motivation

Infections, brain lesions, idiopathic intracranial hypertension or other disorders can result in raised intracranial pressure (ICP) which is normally maintained at $10 - 18\,cm\ H_2O$ by a clear liquid which is named cerebrospinal fluid (CSF). Elevated ICP can cause both generalized and ocular damage, such as compression of the optic nerve around its whole circumference in a "choking manner". This can cause optic nerve head (ONH) edema also known as papilledema [25]. Papilledema can cause optic disc protrusion and engorgement of blood vessels and nerve fibres. Given the role of the optic nerve which is to transmit photosensory information from the retina to the brain, ONH may lead to permanent vision loss.

Elevated intracranial pressure can be treated by medication however, when this fails, alternatives are Ventriculo-Peritoneal Shunting (VPS) and Optic Nerve Sheath Fenestration (ONSF). VPS is a risky complex neurosurgical procedure. It aims to redirect excess CSF from the ventricles to the abdominal compartment. On the other hand, ONSF involves surgically opening the optic nerve sheath to locally provide a sustained drop in ICP. It is a less invasive procedure compared to VPS however, it still is a surgical option to treat significant ONH and the elevated hydrostatic pressure on the optic nerve.

The preferred approach to ONSF is termed "Medial Transconjunctival", [25] and is shown in Fig. 3.1. It can minimize surgical invasiveness, bleeding, and damage to structures local to the optic nerve [25]. However, to expose the optic nerve, the medial rectus muscle has to be separated from the eye and extensive manipulation of the eye is required.

The procedure starts with the isolation and then the detachment of the medial rectus muscle. Then, the globe is retracted laterally. The orbital fat is retracted
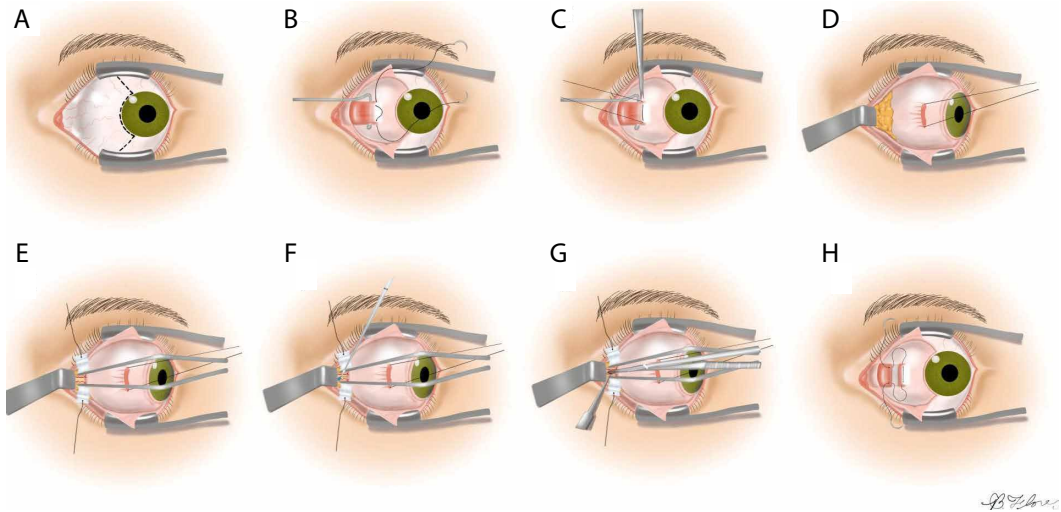
Figure 3.1: Medial transconjuctival approach for ONSF. **A:** Peritomy is performed, **B:** Isolation of the medial rectus muscle, **C:** The muscle is detached from the globe, **D:** Lateral retraction of the globe, **E:** The orbital fat is retracted away from the optic nerve, **F:** Incision of the optic nerve sheath, **G:** Extension of the incision to a total length of 3 to 5 mm, **H:** The medial rectus is reattached and the peritomy is closed. Image adapted from [25].

away and the optic nerve is exposed. A small incision is performed on the optic nerve sheath to relieve the optic nerve pressure. The procedure ends with the reattachment of the medial rectus to the globe and the closure of the peritomy. This intervention can be suffer from complications and the chance of inadvertent tissue damage is increased. Therefore, ONSF is currently reserved for patients with significant papilledema and progressive or impending visual loss.

ONSF significantly improves the function of the optic nerve [129], but is not widely used due to the difficulty in surgical access and risk of sight loss [130]. Notably, the complication rate was found to be as high as 45% (mean of 12.9%) [131] and approximately 1 out of 8 (sample of 317) ONSF interventions fail to restore vision and a re-operation is required due to sustained elevated pressure [131].

To overcome the challenges presented in deep orbital interventions such as ONSF, surgical robots are proposed to be used. Surgical robots can offer solutions to the unique challenges that presented above. Continuum robots and more specifically CTRs are proposed for a novel approach to access the eye orbit and the optic nerve by navigating periocularly, following the eye surface, to reach the

position where multiple concentric tube robot arms collaboratively perform the intervention. Figure 3.2 shows the robotised approach of cannulating the optic nerve sheath. CTRs access the posterior part of the eye globe through a bespoke collimator that is sutured on the eye sclera (the white protective part of the eye) as a hybrid mechanism for deep orbital interventions and specifically ONSF.

The suggested approach promises to drastically reduce the invasiveness of a broad range of orbital interventions as it need not be restricted to ONSF. It can perform with minimal adjustments intrarterial cannulation for retinoblastoma and interventions to cure myopic staphyloma. In these interventions, no robotic approach has been addressed yet.

3.2   System Design & Prototyping

3.2.1   End-Effector Design and Engineering

The mechanical system design begins with a Degree of Freedom (DoF) discussion for tool positioning, and selection of the dimensions of the tubular components that house the surgical instruments. The clinical requirements of ONSF highlight the need of a vision module and at least two arms for tissue manipulation and completion of the surgical task. One arm holds the tissue while the other performs optic nerve cannulation. Moreover, the surgical area that the arms should cover starts 2 mm posterior to the globe and extends posteriorly for a total length of $4-5$ mm [25]. The CTR arms should access this workspace by following the curvature of the eye, therefore they should be able to bend by at least that radius of curvature [132]. To minimize disruption to surrounding tissue and to facilitate the insertion of the tools to the desired workspace, a bespoke collimator is employed to introduce the continuum arms and hold the camera.

To achieve the required flexibility and steerability, concentric tube technology is employed. All the tubular components are made from NiTi to take advantage of its excellent elasticity and recovery capabilities [46]. Concentric tube technology enables the design of a manipulator to a diameter even to less than a millimeter while retaining high tip dexterity. These characteristics are necessary in deep orbital
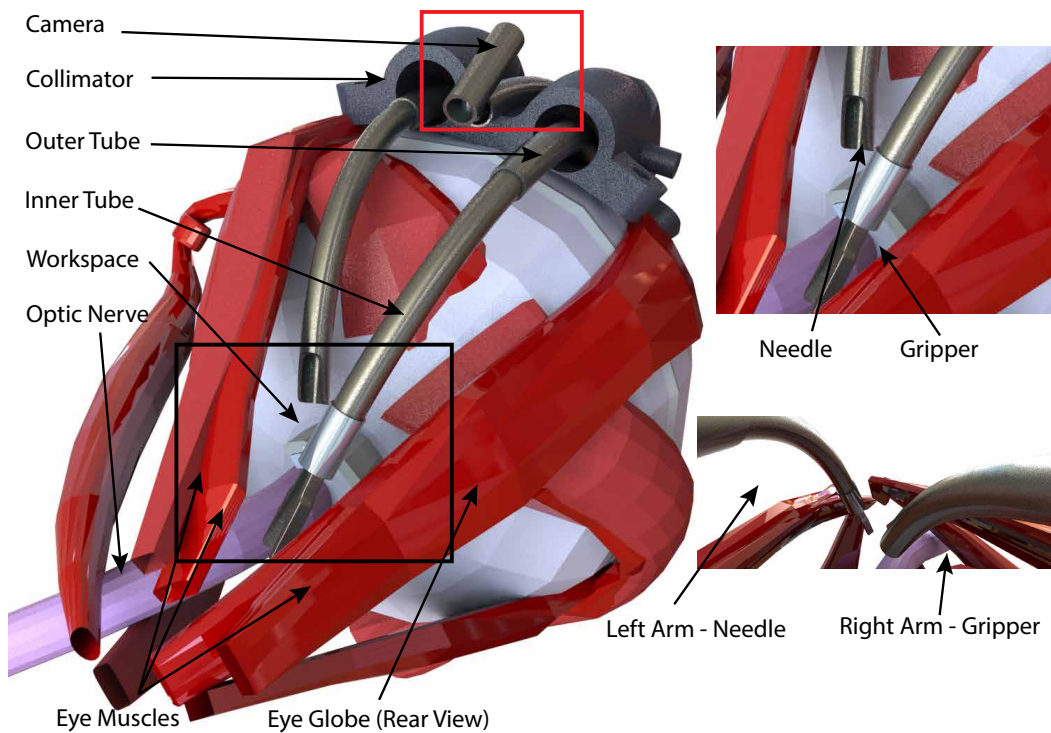
Figure 3.2: Left: Illustration of periocular access to the optic nerve using the developed robot. **Right:** Visualization of the surgical arms and tools. The red box indicates the desired workspace.

interventions due to the limited surgical workspace.

The CTR arms access the posterior part of the eye and the surgical area through a bespoke collimator shown in Fig. 3.2. The collimator is a guide which comprises two channels for the insertion of the tool-holding arms, and an open channel for the insertion of the camera arm. Each channel has a diameter of 3.5 mm to facilitate the insertion of the arms while the thickness of the collimator is chosen to be 6 mm to fit in the lateral side of the eye globe. Its radius of curvature is equal to the radius of eye i.e. approximately 11 mm, while its width is less than 13 mm to fit between the lateral and superior rectus muscles [132]. Moreover, it possesses anchor points for suturing on the eye globe. Suturing similar guides on the sclera is a common approach in procedures such as scleral buckling.

The set of tubes comprising the tool-holding continuum arms are identical in their diameters. They were chosen to function simultaneously with the camera in the limited surgical workspace, and to perform cannulation and grasping of the optic

Table 3.1: Dimensions of the NiTi tubes. The variable OD stands for Outer Diameter, ID stands for Inner Diameter, L_s and L_c stand for tube's straight and curved length and R stands for radius of curvature.

	OD (mm)	ID (mm)	L_s (mm)	L_c (mm)	R (mm)
IT_{left}	1.12	0.80	17.27	31.20	9.00
OT_{left}	1.80	1.52	0.00	26.84	33.00
IT_{right}	1.12	0.80	17.12	26.75	9.00
OT_{right}	1.80	1.52	0	17.42	22.00
Camera	1.80	1.52	5.00	13.89	38.40

nerve. The outer diameter (OD) of the outermost tube was constrained to be within the collimator, while the inner diameter (ID) of the innermost tube was constrained by the size of the deployed micro-gripper. To enhance the dexterity and the overall workspace of the robot, each continuum arm comprises two tubes, therefore being a 4 DoF system. A 5-th DoF is included through the tool's roll capability.

The continuum arm holding the vision module is chosen to be a single tube, therefore possessing 2 DoF, which are adequate for visualization of the tools and the workspace. The selected chip-on-tip camera is 1.2 mm diameter (Enable, Inc., United States), with a 120° field of view (FoV) and $2.5 - 70$ mm depth of field. Illumination is achieved through optical fibres housed within the camera body.

The curvature of each one of the tubes was decided keeping into account that the outer tube should be less curved than the inner one to ease the rotation of the innermost and reduce torsion. In addition, NiTi remains elastic to strains, ε, up to 8% [34]. The strain that a tube with radius r expresses related to its final, u_f, and initial, u_i, curvature is:

$$\varepsilon = r(u_f - u_i). \tag{3.1}$$

which gives the maximum curvature that the tubes can possess to reach the desired workspace. Their final values were chosen by following the guidelines of length and curvature reported in [34], with the goal to maximise reachability while avoiding mechanical instabilities. They are presented alongside the selected diameters (OD, ID), radii of curvature (R), and lengths (L_s, L_c) in Table 3.1. Please note that two

lengths are indicated, namely a curved length, L_c, which is the "continuum" part of the manipulator, and a straight length, L_s, which ultimately links the tube with the transmission system. IT, and OT, stand for the inner, and outer tube of each arm, respectively, while the subscript refers to the different arm. Figure 3.2 shows the curvature of the tubes and their visualization from the camera.

3.2.2   Engineering Process - Prototyping of Tubes, Tools

The micro-gripper (see A in Fig. 5.3) is produced in separate halves with wire Electro-Discharge Machining (EDM). Each half is cut with a thin electrode from a 0.7 mm thick stainless steel sheet. The gripper's half is composed of a grasping jaw, which is 3.2 mm long, 0.7 mm wide, approximately 0.5 mm thick, and a thin stem that acts as a spring element once the two gripper's halves are welded together. The stem is approximately 3 mm long and is welded at the base to the opposite jaw's stem. Welding is realized using a laser micro-welder while holding the jaws angled at approximately $30°$. The welded gripper stems act as a spring by maintaining the jaws in an open configuration. When it is pulled back relative to a cylindrical socket, the inner wall of the socket forces the gripper to close. A thin stainless steel wire (diameter 0.2 mm) is welded to the micro-gripper stems to control the relative position of the grasper compared to the socket. On the contrary, the cylindrical socket is glued on the exterior of the inner concentric tube. An illustration of the gripper's design is shown in Fig. 3.3.

Cannulation of the optic nerve is achieved through the second arm, B in Fig. 3.3. The tip of its inner concentric tube was cut to have a bevel of $45°$, allowing its use as a needle.

The vision module was mounted on a NiTi arm via the employment of a holder clip. The clip was produced with a section of stainless steel (SS316) tube. To improve the triangulation and visualisation of the surgical target, the clip was welded to the NiTi tube at an angle of approximately $15°$, see C in Fig. 3.3. In the future, the camera will be directly inserted into a NiTi tube. Currently, it was preferred to maintain it external for simplicity of placement and maintenance.

NiTi tubes were precured using heat treatment. An aluminum template (Al

2219) with slots/grooves of the desired curvature was machined. Parts of the curving protocol were extracted from different sources in the literature while experimental work went into its fine tuning. A summary of the curving protocol has been provided in Chapter 1 for completeness. The final relaxed tube curvature for use in mechanics models was identified using a vector graphics editor to fit a circle on the tube and measure its radius. The drawback of shaping NiTi tubes through heat treating in a furnace is that a part at its distal end cannot be bent to the desired curvature but rather stay straight [46]. To follow the assumption of constant curvature in the modelling theory of CTRs, the straight part at the distal end of the tube is removed.

To minimise the length of the NiTi tubes, which leads to torsion and "snapping", NiTi tubes were glued with Loctite 648 and Loctite 7649 to concentric stainless steel (SS) tubes, which are in turn coupled to the motion transmission mechanism described in the next section.

3.2.3   Motion Transmission Mechanism

The motion transmission mechanisms that deploy the continuum tools are described herein based on the DoF discussion presented above. Figure 3.3 shows the multi-arm concentric tube system that was developed to showcase tool deployment in a phantom as a proof of concept. Each tube is held by a carriage that incorporates the tube rotation mechanism. Each carriage is held by a lead screw. It was chosen to use lead screws for the translation of each carriage and tube because of the precise actuation they offer, their affordability, and long-term reliability. For each robotic arm, two lead screws are used for the two tubes that it comprises.

A timing belt is used for each rotational DoF. Even though timing belts can retain the compactness of the system, the backlash that they may effect to the system is crucial. To avoid such an effect, a pretenser is introduced on the upper part of the carriage (see Fig. 3.3). That part along with an idler add adjustable pretension to the timing belt. Every translational DoF is actuated by a continuous RS motor (SRC SM-S4315R) with a maximum torque of 1.47 Nm while servo motors (DS3235) with maximum torque of 3.43 Nm and range from $0° - 270°$ are selected for the rotational DoFs. The robot's control unit in the current setup comprises po-

tentiometers as input elements that permit fine control of the tip's motion as they allow analogous rotation and intuitive control of the speed insertion (translation) of the tubes. The control board, *i.e.* an Arduino, can be programmed directly via a PC program to implement complex control in the future.

To monitor the translation of each tube, linear, continuous turn, rotary potentiometers are employed primarily due to their low cost. They are connected to a secondary Arduino and the data are passed to Matlab® to estimate each arm's shape by the standard mechanics models of the literature [34, 35]. Any misalignment in connecting the potentiometers and the motors to lead screws and shafts respectively is absorbed by flexible couplings.
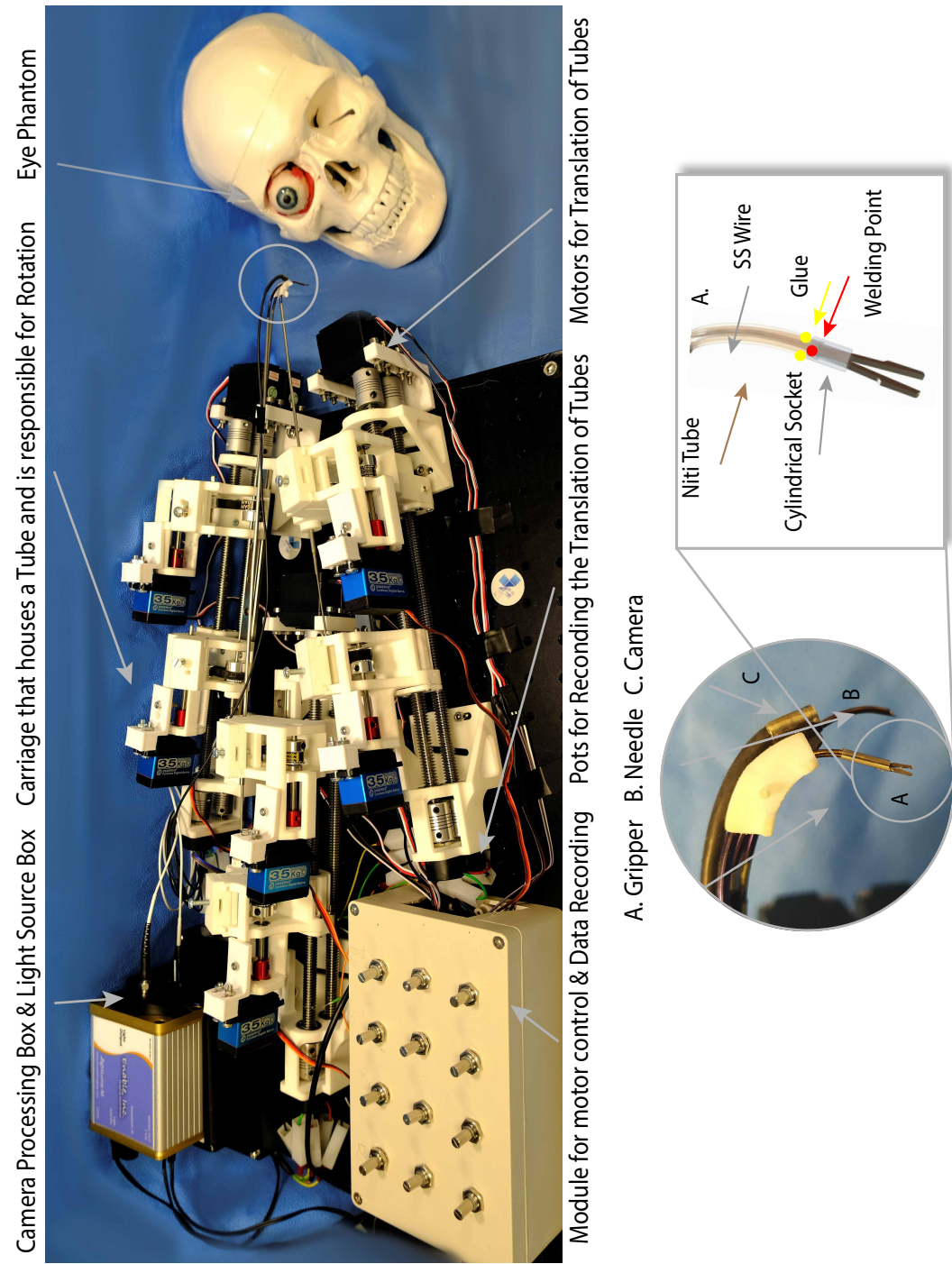
Figure 3.3: The experimental setup, comprising the mechatronics and phantom eye. The eye bulges out of the orbit in the picture for visualization purposes. The inlet depicts A: the micro-gripper, B: the needle and C: the camera while the illustration shows the design and working principle of the micro-gripper. The NiTi tube and the cylindrical socket are semi-transparent for better visualisation of the SS wire.

3.3 Modeling and Workspace Analysis

To validate that the robot can reach the desired workspace and cannulate the optic nerve, the robot was modelled and simulations were run to derive possible rotational and translational inputs respecting the application's required workspace.

3.3.1 Computational & Experimental Workspace Evaluation

System design was evaluated against the requirements by a detailed computational analysis study of the reachable workspace, employing a modification of the framework presented in [116] and also experimentally via the use of an electromagnetic spatial measurement system (NDI Aurora). The reachability results for the two manipulator arms are illustrated in Fig. 3.4. The 3D eye model was segmented from MRI scans and subsequently used to create a realistic phantom for the experimental setup (detailed in Sec. 3.4.1).

First, the global workspace investigated for reachability ($24\,\mathrm{mm}\times18\,\mathrm{mm}\times18\,\mathrm{mm}$) was voxelised into cubes with an edge length of $0.12\,\mathrm{mm}$ ($200\times150\times150$ voxels). Each voxel representing an end-effector position was further subdivided into 420 unique rotations, which results in an angular distance of $18°$ between neighbouring rotations. Each position voxel held the number of orientations that can be achieved at that respective position.

Each tube was rotated and translated within a pre-specified range of values that took into consideration the constraints arising from the collimator and the anatomy; robot tip position and orientation was recorded. For each robot arm's workspace, 50×10^9 random configurations were evaluated using GPU based sampling described in [133]. This number of samples means in average more than $10,000$ random configurations per position voxel were evaluated, and more than 25 random configurations per unique voxel (considering full pose). A position voxel is considered within the workspace if it is reachable by at least one robot configuration.

The outer tube of the left arm was translated by up to $16.7\,\mathrm{mm}$ while its rotation was fixed. This was because the whole workspace could be covered by the rotation of only its inner tube due to its high curvature. The inner tube of the same arm was translated by up to $9.8\,\mathrm{mm}$, and rotated from $-23°$ to $5.4°$ while the inner tube of the

Desired Workspace   Gripper   Gripper's Workspace   Needle's Workspace   Needle
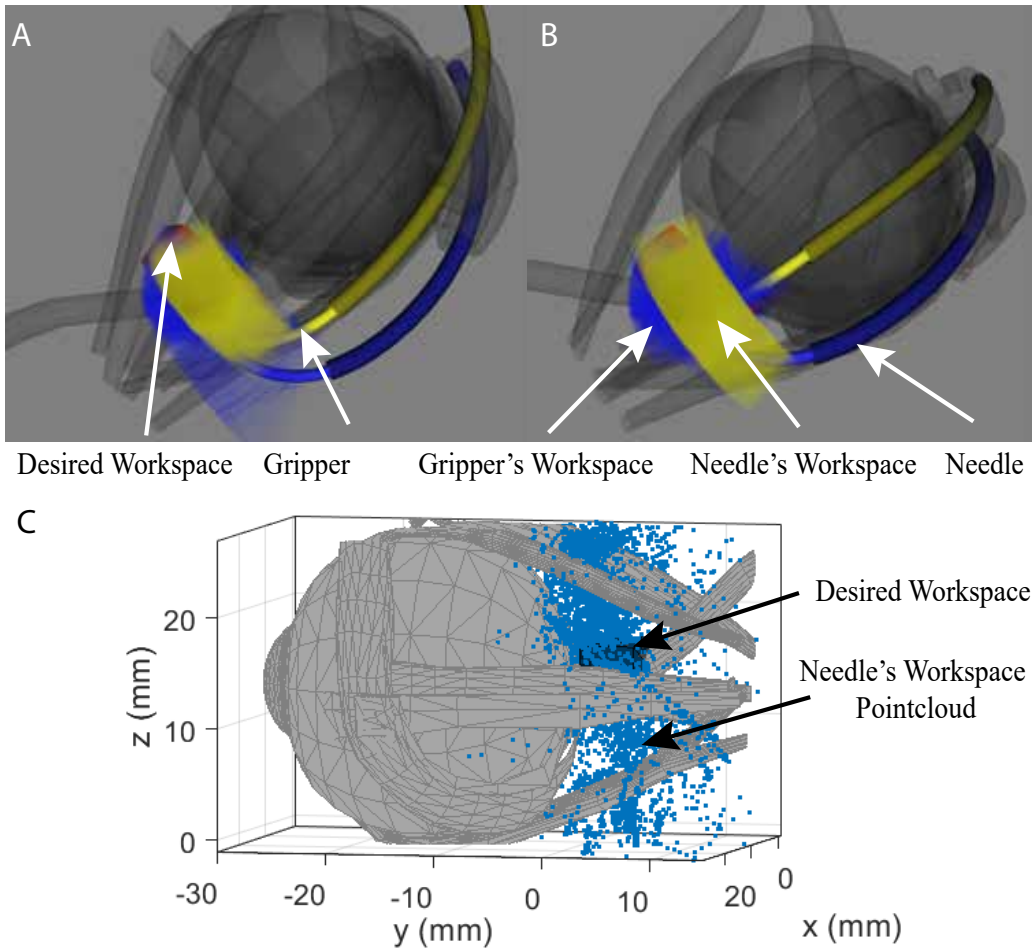
Figure 3.4: Visualization of the reachability of the desired workspace by the concentric tube manipulators. **A** - **B**: Computational analysis results: Yellow, and blue represent the reachability of the micro-gripper, and needle tip, respectively, for the evaluated configuration space, red represents the target workspace which is completely covered. **A:** Side view of the manipulator's workspace. **B:** Top view of the manipulator's workspace., **C**: Experimental validation of workspace.

right one was translated by 3.3 mm and rotated from $-5.2°$ to $11.9°$. The translation of the outer tube of the right arm was up to 8.8 mm and its rotation ranged from $-16.4°$ to $0°$. The computational result (see Fig. 3.4) supports that the designed continuum arms can reach the desired workspace based on the examined set of joint values. In Fig. 3.4, the gripper's and needle's workspace are represented by yellow and blue respectively while the desired workspace, which is fully reachable, is represented in red.

To validate the analysis presented above and that the curvatures and the lengths

Ophthlamic Artery   Optic Nerve   Medical & Lateral Rectus Muscles

Inferior Oblique   Superior Oblique Tendon   Collimator   Fixation Points
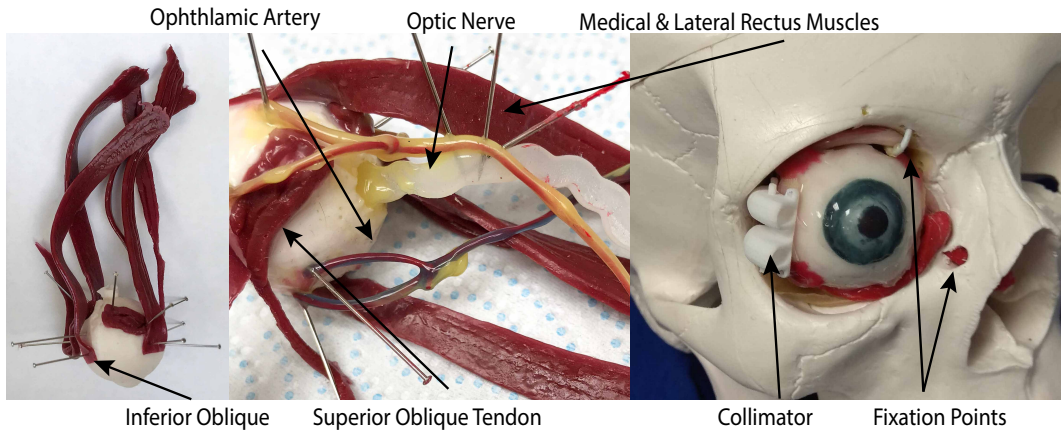
Figure 3.5: Illustration of the fabricated eye phantom and its elements.

of the tubes can cannulate the optic nerve, the prototypical robotic needle was translated and rotated while its position was recorded by an electromagnetic (EM) spatial measurement system (NDI Aurora). An EM tracker was firmly secured with tape on the exterior surface of each tube. As a result the inner tube could not be fully retracted into the outer one without restricting though the coverage of the desired workspace. The offset between the EM tracker and the tube axis was taken into account in the form of a constant transformation in the final results. Figure 3.4(A-B) presents the point-cloud workspace of the needle. It can be seen that the workspace covers a volume of $275\,\text{mm}^3$ which is the surgical area of interest while Fig. 3.4(C) depicts only the needle's workspace for clarity. The measurements were recorded during continuous rotation motor operation but with inert translation motors. The former are the distant to the EM sensors and do not affect the measurements. The latter introduce no noise when inert.

3.4 Proof-of-Concept Experimentation

The experiments section will demonstrate a meaningful manipulation sequence, derived from the robot mechanics models, that positions the tools along the configurations required to perform ONSF. This experimental study focuses on the performance evaluation of the needle of the end-effector to cannulate the optic nerve. High-fidelity components of the eye orbit were developed and fabricated to experimentally evaluate a deployment sequence, as detailed in the following.

3.4.1   Fabrication of a High-Fidelity Eye Phantom

A segmented 3D MRI scan of an adult patient's eye was used as a reference, along-side anatomical drawings. Through the 3D segmentation of the scan, a life-size rigid 3D-printed eye orbit including the optic nerve, rectus and obliques extraocular muscles and their tendons was created for reference on fabrication of a eye phantom in collaboration with the Royal College of Arts.

First, the eye globe (oculus) was isolated from the rest of the 3D-printed structures; it was cast and a mould was created. The shore 2A platinum silicone rubber was selected to model the optic nerve as its stiffness is closer to human's optic nerve sheath which is $E = 0.1\,\text{MPa}$, [134, 135]. The Young's Modulus of the selected rubber is $E = 0.26\,\text{MPa}$ according to manufacturer's data-sheet. The selected rubber, pigmented to the desired color white colour of the sclera, was poured in the mould to replicate the eye in its true dimension. When the silicone cured, the oculus was demoulded and detailed iris and pupil were painted onto it.

Subsequently, the muscles, the common tendinous ring, and the optical nerve were sculpted with plantinum cure silicone shore 2A and pigmented to the desired color following illustrations of the anatomy. A silicone tube with a diameter of approximately 2 mm was used for the fabrication of 2 blood vessel structures: a representation of the 4 vortex veins, and a representation of the ophthalmic artery with 3 branches (the ophthalmic artery, long posterior ciliary arteries and the central retinal artery). It was then coated with platinum cure silicone 2A shore to simulate the color and texture. A fat-like yellow/red color was used to color the artery, while a blue/purple coating was used to simulate the color of the vein. Platinum cure silicone rubber with shore hardness of 2A was used to assemble all components.

Once the separate components were cured, they were pinned onto their position on the eye and connected with silicone. The common tendinous ring and the muscles were attached, and the nerve and blood vessels were positioned. The completed phantom is shown in Fig. 3.5, where major elements of the anatomy are illustrated.

Upon the completion of the eye fabrication, it was installed into the cavity of a
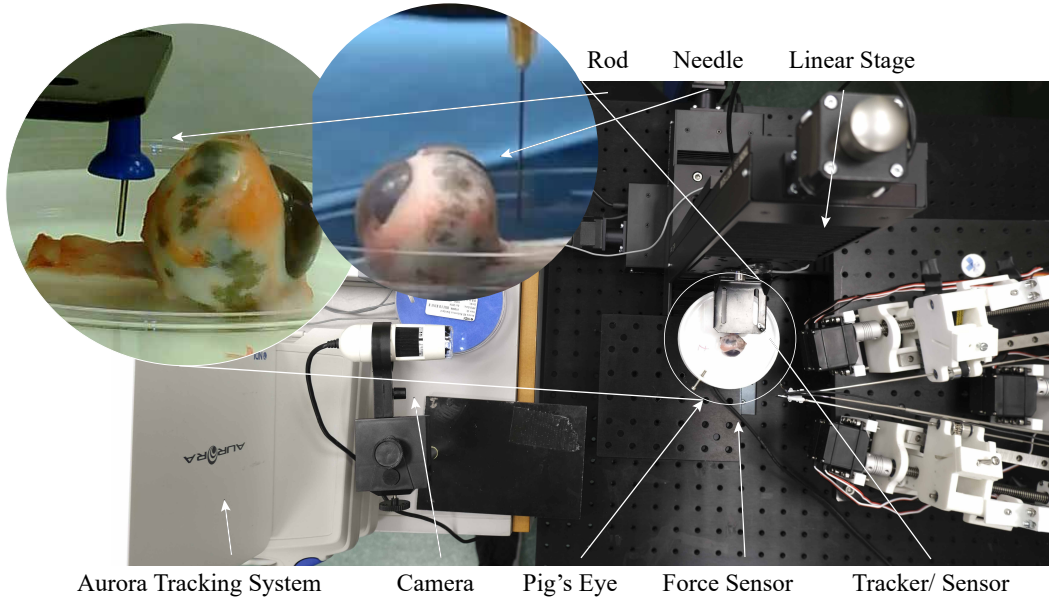
Figure 3.6: The experimental setup, comprising the porcine eye, the force sensor, the linear stage, and the tracking system.

commercially available skull. It was fixed by securing the inferior oblique muscle and superior oblique tendon to the orbital wall, while tension was provided via a knot on the optic nerve as it passes into the skull.

3.4.2 Experimental Evaluation with *Ex Vivo* Tissue

To prove that the robot can cannulate the optic nerve, a series of experiments were run on porcine eyes. They have been conducted to evaluate the performance of the robot on real tissue and due to lack of comparative data on the requirements of ONSF in the literature. The tests are: 1) stiffness measurement along the porcine eye and the eye phantom optic nerve, 2) ONS penetration force threshold measurement, and 3) robotic cannulation of the porcine eye optic nerve.

3.4.3 Porcine Eye & Eye Phantom Stiffness Measurement

Porcine eye samples acquired from an abattoir were glued to a Petri dish and placed on a 6-axis force sensor (ATI F/T Sensor: Nano17). To measure the stiffness of porcine optic nerve, a blunt pin (1.12 mm diameter) was employed to deform it by 1 mm in 3 different positions at 4, 6, and 8 mm distance from the posterior part of the eye globe for 10 different eye samples (see Fig. 3.6). These positions were

chosen according to the desired surgical workspace. The force exerted on the optic nerve was measured by a force sensor, and the motion of the pin was recorded via an electromagnetic spatial measurement system. The porcine eye was glued to a petri dish which was placed securely on a 3D printed base. This base was able to be placed rigidly using screws on the force sensor. It was found that the stiffness of porcine optic nerve increases along the nerve (as observed also on human tissue), and had an overall mean value of 0.27 N/mm (see Fig. 3.7).

The same experiment was carried out 5 times on the fabricated phantom. The stiffness of its nerve remains almost constant along it, with a mean of 0.44 N/mm, due to its homogeneous fabrication (see Fig. 3.7). It is on the same order of magnitude as the stiffness of the porcine optic nerve, making the phantom a good model for comparison with *ex vivo* data.

3.4.4   Porcine Optic Nerve Penetration Threshold

To measure the force required to cannulate the optic nerve, a similar experiment as in the previous case was carried out with a needle (Microlance 3, 0.5×25mm) on 4 different porcine eye samples. The averaged penetration force vs. indentation plot in Fig. 3.8 shows the deformation and penetration regions of different layers of the nerve tissue. The shaded area presents the minimum and maximum values recorded for each penetration value in the trials. The nerve sheath deformed until the force reached ≈ 0.1 N at ≈ 0.4 mm indentation where the sheath was teared, compared to 23.51 mN in the case of vitrectomy [136]. The needle penetrated further the tissue until it reached the nerve itself at ≈ 1 mm indentation, which is consistent with clinical measurements of the sheath thickness [134]. The nerve deflected ≈ 0.2 mm further where the needle pierced it with ≈ 0.2 N force. The robot needs to exert such forces with appropriate needle attack angle to perform ONSF.

3.4.5   Robotic Cannulation of Optic Nerve

Figure 3.9(top) shows cannulation of porcine optic nerve with the robot's sharpened tip. Four porcine eye samples, glued to a Petri dish and placed on the force sensor, were used to test the robotic cannulation procedure. The robotic needle
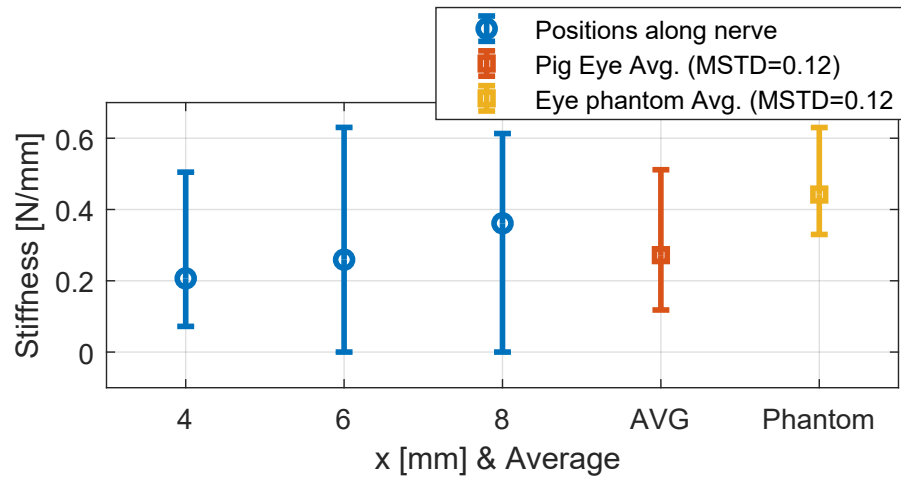
Figure 3.7: The stiffness of the porcine optic nerve for 4, 6, and 8 mm distance from the eye globe, average stiffness along the nerve (AVG), and the average stiffness of the high-fidelity eye phantom optic nerve.
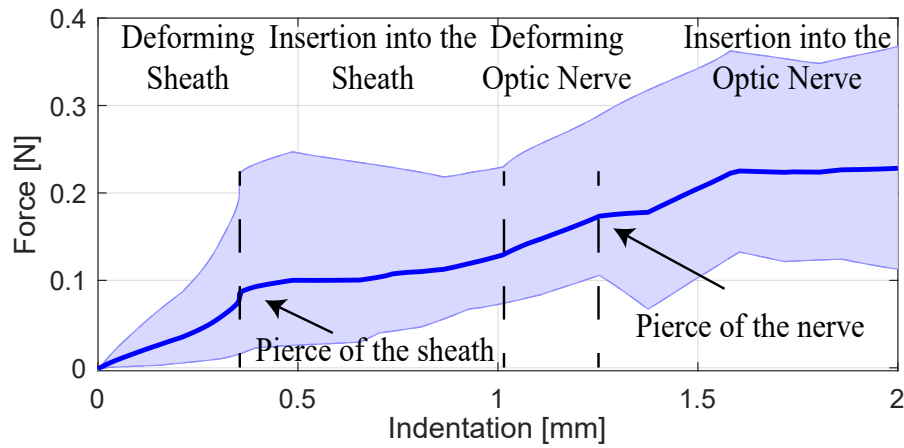
Figure 3.8: Mean value of insertion force versus displacement from experiments on 4 porcine optic nerves, and maximum/ minimum thresholds for measured values.

was extended until penetration of the nerve sheath was visually confirmed. Figure 3.9(middle) presents the force values exerted by the robotic needle for each trial starting from the time when the robot tip contacts the tissue, identified as a small spike in the force sensor readings. Figure 3.9(bottom) shows the filtered averaged values and the maximum and minimum threshold for the measured values. In all cases, penetration of the optic nerve was visually confirmed. Please note that the optic nerve was accessed from the opposite direction compared to a real scenario to decouple the compressing effect that the collimator might have on the porcine
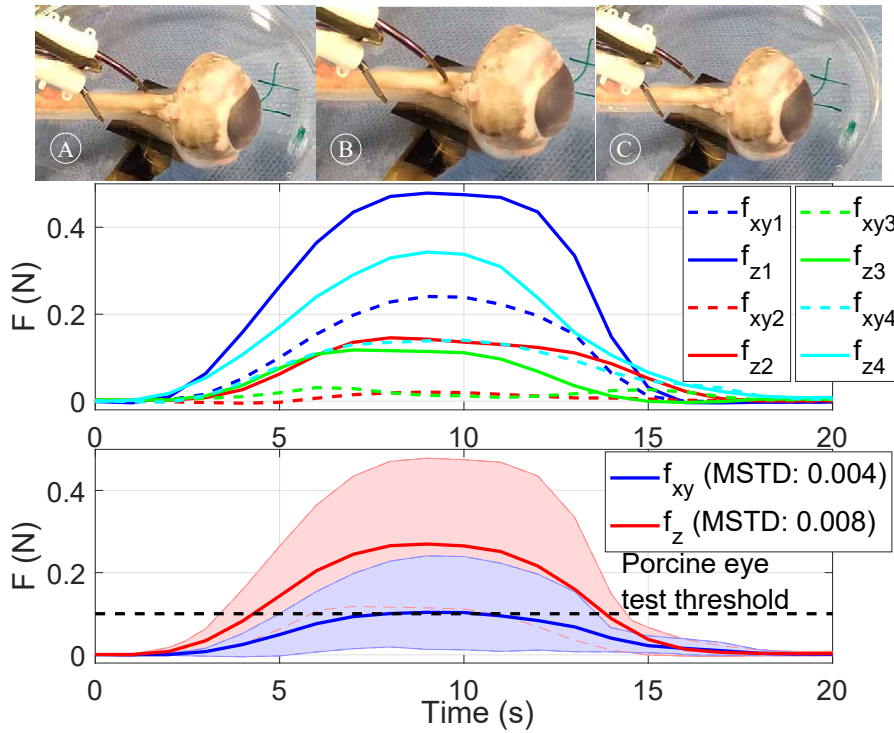
Figure 3.9: Penetration of the optic nerve by the robot's needle. Top- **A**-**C** indicate cannu-
lation of the optic nerve. **A**: Approach of the robotic needle, **B**: Cannulation
of the optic nerve, **C**: Retraction of the robotic needle. The graph presents
the mean value of the vertical and lateral forces as measured by the force sen-
sor and the maximum and minimum recorded values between different trials.
Middle- measured values for 4 trials. Bottom- averaged value and maximum
and minimum threshold for measured values of lateral (f_{xy}) and penetrating (f_z)
forces.

eye from the exercised forces. To simulate the resistance that the skull's bone ap-
plies on the collimator, the collimator was held fixed at a mirror distance from the
sclera. The measured forces are higher than the mean penetration threshold shown
in Fig. 3.8. Possible reasons for this difference are the deviation of the robot tip
attack angle, the reduced sharpness compared to a standard needle and the different
indentation values.

3.4.6   Experimental & Simulation Study with Eye Phantom

To prove the concept of accessing the eye orbit and perform an intervention on the
optic nerve, the tools that were described above were actuated to perform ONSF on
the high-fidelity eye phantom. Figure 3.5 shows the posterior part of the eye upon
its fixation into the skull, while the collimator is also illustrated. The tool guide is
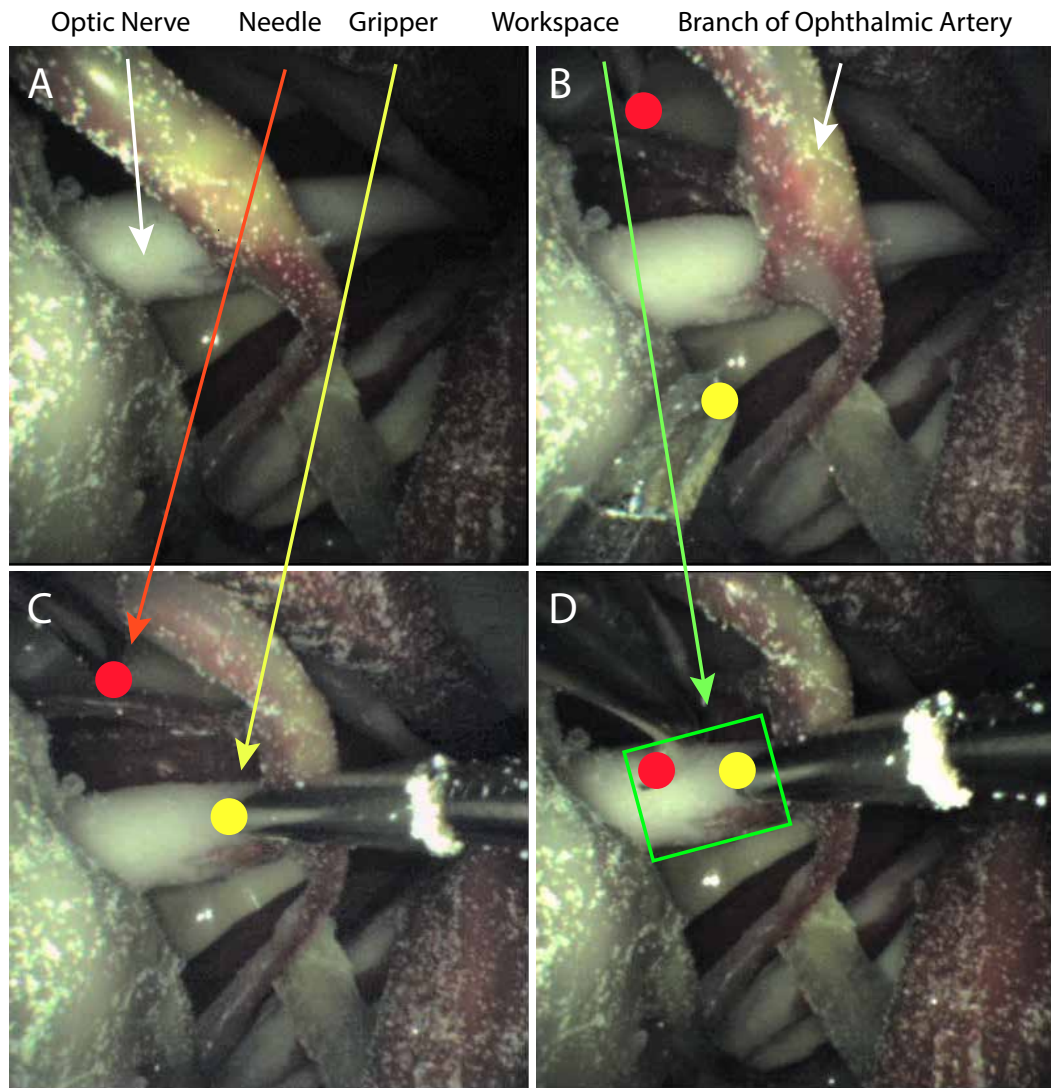
Figure 3.10: Deployment of the manipulators and the camera for OSNF. **A** - **D** indicate cannulation of the optic nerve. Brightness was enhanced for clarity. **A:** Visualization of the optic nerve from the camera. **B:** Both manipulators come into sight. **C:** The right manipulator (micro-gripper) grasps the optic nerve. **D::** The left manipulator (bevel tip) approaches the optic nerve. Everything is recorded via the miniature camera mounted on the third arm.

placed between the lateral and superior rectus. Next, the arms and the camera are inserted in the collimator, either automatically or manually using surgical tweezers, and access the orbit. The tube that holds the camera is manipulated to illuminate the orbit and reach the FoV that visualises the desired workspace and tool access points. The arm that holds the micro-gripper grasps the optic nerve to hold it steady during cannulation. Upon the grasping of the optic nerve, the second arm with the
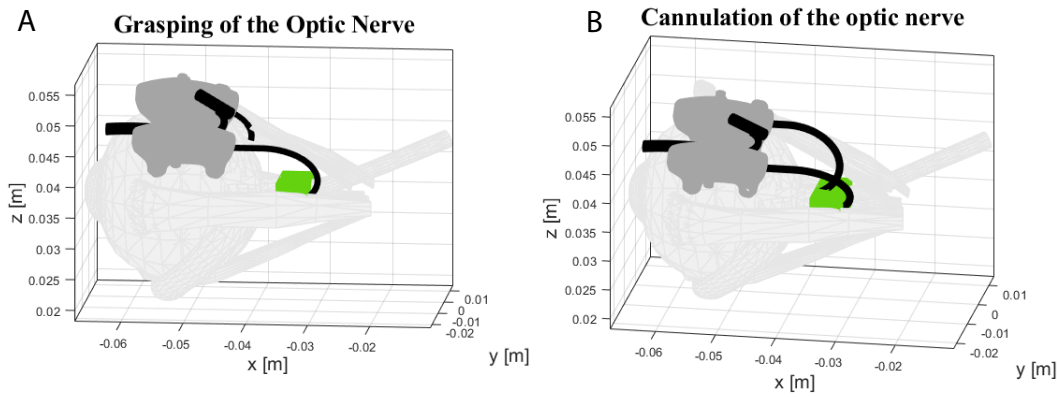
Figure 3.11: Grasping (**A**), cannulation (**B**) of the optic nerve as derived from the theoretical model based on encoder readings from the experiment in Fig. 3.10.

bevelled tip approaches the surgical area of interest and cannulates the optic nerve. The tools are then retracted and the robot can be placed away from the skull. Figure 3.10 illustrates the deployment of the tools as captured from the camera's viewpoint. Both tools operated in the desired workspace as the workspace analysis predicted.

The recorded rotation and translation of each tube were imported as initial conditions to the theoretical mechanics model of Chapter 2, to verify the theoretical model framework. Figure 3.11 shows the grasping and cannulation of the optic nerve as they were derived via simulations by moving the arms according to the experimental inputs of Fig. 3.10. The theoretical model confirms that both arms can operate in the desired workspace as it was validated by the experimental results. Figure 3.10 shows successful deployment of the arms in accordance with the prediction of the arm's shape based on the simulation results in Fig. 3.11A-B.

3.5   Conclusion

In this chapter, the work on the development of a multi-arm CTR for deep orbital interventions was presented, emphasizing on the treatment of ONSF. The design of the system considers the limitations and constraints that occur in ophthalmic surgical procedures of the optic nerve, *i.e.* limited workspace, high radius of curvatures, bimanual manipulation, and visualization of the tools and the area of surgical interest. It was shown that the proposed system can navigate periocularly the eye and perform the desired procedure in our theoretical simulation and experimental

study, and in comparison with *ex vivo* porcine tissue experimental evaluation. Here, the bespoke collimator plays the role of the navigation section. It can be designed, based on the MRI scans of a patient, being in this way a patient-specific component in the overall system. To generalize the design of the system and make it unaffected by the patient of interest, new directions are explored and presented in the next chapters to substitute this patient-specific component with a generalized approach in the design of the multi-arm continuum robot.

This work is considered to be among the state-of-the-art research studies focused on the development of multi-arm robotic system with 2 and 3 arms as it was stated in [137], while in [138] the validity of using CTRs to cannulate the optic nerve is recognised.

Chapter 4

Eccentric Arrangement of Concentric Tubes

This chapter conceptually continues the work presented in Chapter 3. A flexible backbone can substitute the bespoke collimator offering increased dexterity and flexibility to a multi-arm CTR robot. This design option is explored in this chapter, for which a quasistatic mechanics-based model is presented and experimentally evaluated. It describes the shape of concentric tube robotic arms when they are eccentrically arranged along an also-flexible backbone.

The model can estimate the shape of both the backbone and CTR arms, and can accommodate an arbitrary number of CTR arms arranged in an eccentric position with regards to the backbone's neutral axis. Experimental evaluation with a prototype system on the benchtop highlights the promise of the end-to-end proposed modelling approach, as the error between model and experiment is around 8.7% of the manipulator's overall length. The theory is the first step towards modeling multi-arm concentric tube robots, a class of continuum robots that is increasingly being considered for single-port surgical applications.

The majority of this chapter is adapted from a paper published in the *International Conference on Biomedical Robotics and Biomechatronics (BioRob)* in 2018 entitled "Towards Modelling Multi-Arm Robots: Eccentric Arrangement of Concentric Tubes" [3] and in the *10th Hamlyn Symposium on Medical Robotics* entitled "Mechanics Modelling of Eccentrically Arranged Concentric Tubes" [4].

The primary contribution of this chapter is the first quasistatic model that takes into account the eccentricity of CTR arms housed in a flexible navigation section. It is the first suggestion of a flexible navigation section that houses multiple manipulation arms enhancing in this way the flexibility of the robot's end-effector.

4.1   Multi-Arm Concentric Tube Robot Design

According to the clinical requirements presented in Chapter 3, three robotic flexible arms are eccentrically arranged with respect to the neutral robot axis: two hold tools for bimanual manipulation, and one holds a camera (1.2 mm diameter, Enable, Inc., United States). They are housed within an actuated flexible body that acts as the robot backbone. For all arms and the backbone, flexibility and steerability are achieved through concentric tube technology. As is most common in the literature, all tubes are made from NiTi to take advantage of its excellent elasticity and recovery capabilities [139].

In our current design, the backbone CTR is a 3 Degree-of-Freedom (DoF) variable stiffness section [34], comprising two tubes of identical precurvature and stiffness, and is used for global positioning and navigation of the arms. Each one of the tubes is able to be independently rotated but they are translated together as a system. Following the terminology of [34], the backbone acts as the "navigation section", while the arms act as the "manipulation sections". Each robotic arm comprises two tubes, therefore being a 5 DoF robot when accounting for the capability of tool roll. The considerations below relate to the introduction of a filling material that retains the separation of the flexible manipulation sections within the robot's navigation backbone. A rendering of the multi-arm system is depicted in Fig. 4.1.

The introduction of a filling material in the inner tube of the navigation section is required to avoid contact between the manipulation instruments and camera, both with respect to one other and the navigation backbone. This filling material should maintain the desired arrangement of manipulation instruments and their eccentric placement within the robot body, especially when the robot segments are independently actuated. The filling material must satisfy the requirements of high

flexibility, high tear resistance, and low friction. Multi-lumen catheters made of materials such as PVC, PTFE, or FEP are therefore ideal candidates given their compatible material properties primarily their elasticity and incompressibility.

The manipulation sections are spatially constrained within the navigation section by the filling material. Therefore, when the navigation section's shape changes, the shape of the manipulation arms changes as well - and vice versa. The stiffnesses of all tube constituents within the robot affect the overall shape, and these interactions need to be accounted for by any model. The development of the theory that describes the tube mechanics when eccentrically arranged is the focus of the next section.

4.2 Modelling Eccentrically Arranged CTRs

The model for the statics of a single CTR has been derived in [35, 34] and presented in Chapter 2. The previous work is extended to develop a model, based on the Cosserat-rod theory, for a multi-arm CTR as an eccentric arrangement of multiple CTRs. The assumptions of the classical elastic-rod theory of Kirchoff are employed [35]. The model assumes that only one module is moving at a time with slow velocity, and is therefore quasistatic. Subscript $i = 1, \cdots, N$ denotes the parameters and variables of the ith tube, while $j = 1, \cdots, N$ denotes the arm of the robot that the equation is referred to. For simplicity and without loss of generality, the model for the designed robot is presented, *i.e.,* $i = \{1,2\}$ (two tubes per section, 1 denoting the inner tube, and 2 denoting the outer tube), and $j = \{1,2,3,4\}$ ($1-3$ for the manipulation sections and 4 for the navigation section).

As was presented in Sec. 4.1, the navigation backbone of the robot comprises two NiTi tubes that can carry three manipulation arms, each composed of two NiTi tubes. The filling material placed inside navigation backbone, holds the three manipulation arms with an offset with respect to its centerline (see Fig. 4.1).

To describe the shape of the multi-arm CTR, the robot is broken into several segments between transitions points, *i.e.* points where a tube goes from straight to curved or points where a tube ends (see Fig. 4.2) as in the case of the single CTR. A
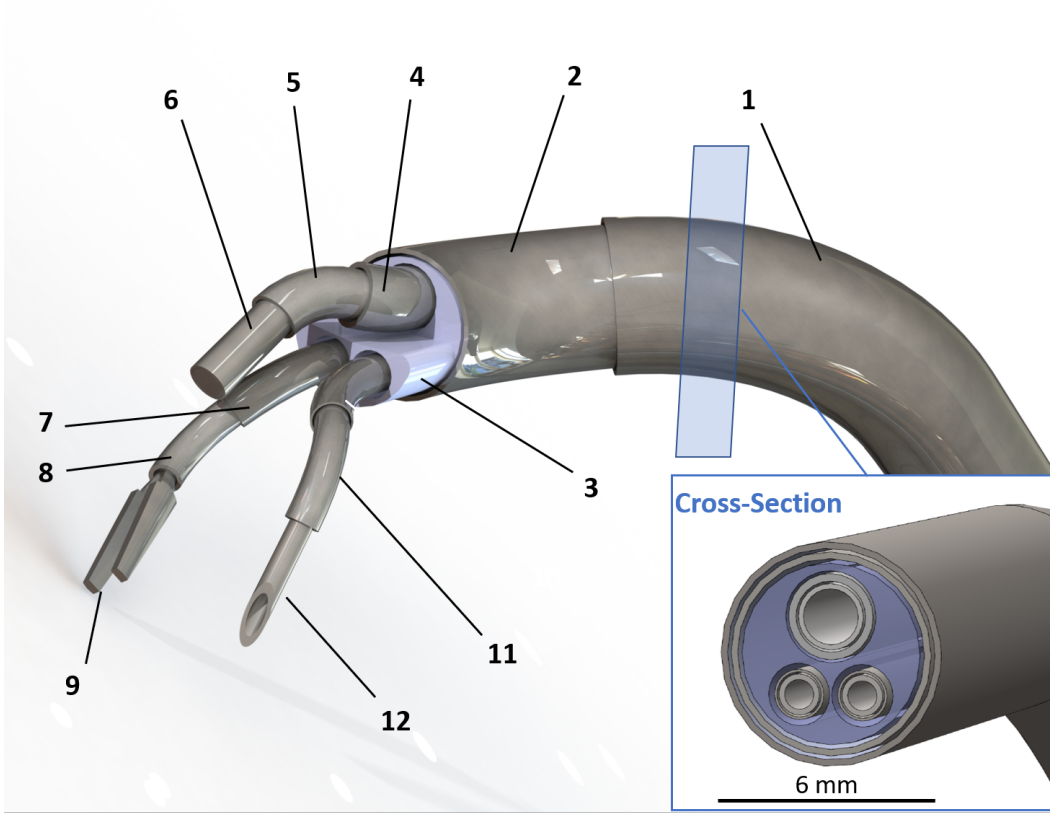
Figure 4.1: Main components and architecture of the microsurgical robot motivating this research: (1) Main body - outer tube, (2) Main body - inner tube, (3) Main body - filling material, (4) Camera holder - outer tube, (5) Camera holder - inner tube, (6) Camera head with integrated illumination, (7) Right instrument - outer tube, (8) Right instrument - inner tube, (9) Right instrument - end-effector, (10) Left instrument - outer tube, (11) Left instrument - inner tube, and (12) Left instrument - end-effector.

segment can contain from 1 to j arms. Segments are later connected to each other by enforcing the continuity of shape and internal moment.

In this approach, the deformed shape of one of the tubes in each segment is estimated. Next, the shape of that tube is used to compute the shape of all the others. Without loss of generality, it is assumed that the outermost tube of the navigation section is the referred tube for the segment that contains all the tubes while for the manipulation sections is the innermost. It should be highlighted that the choice of the referred tubes does not affect the equations that describe the shape of the CTR. As in the case of the single CTR, it should be noted that the equilibrium shape of all tubes that comprise a segment should be identical, *i.e.*, $\mathbf{r}_1^j(s) = \mathbf{r}_2^j(s)$.
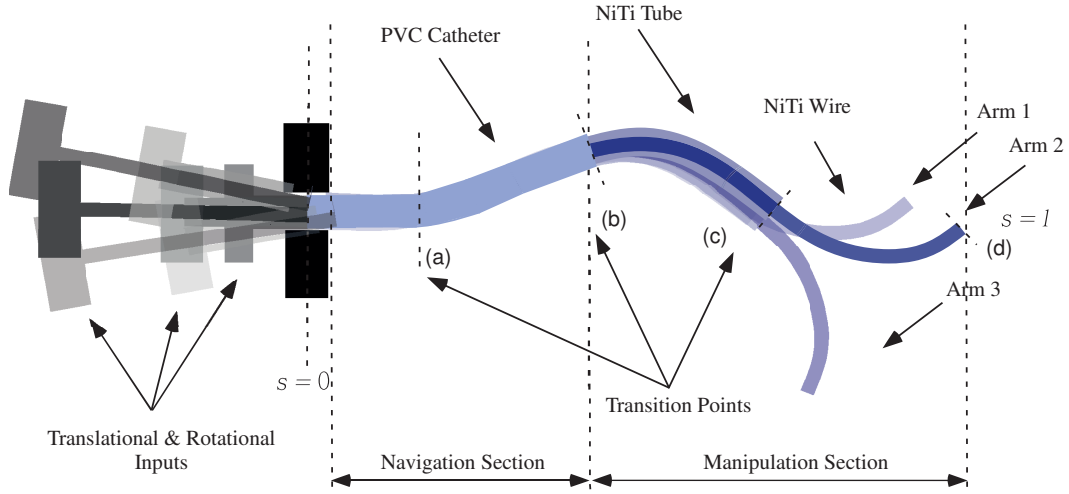
Figure 4.2: Illustration of the concentric tube manipulation arms and the material filling the navigation section.

Now, to relate all the tubes to the referred one, the angle $\theta_i^j(s)$ is introduced to parameterize tubes' twist in a single section as the difference between the rotation of a tube with respect to the referred one. Using this parametrization, I get

$$\mathbf{R}_{i=1,2}^{j=1,2,3,4} = \mathbf{R}_2^{j=4}\mathbf{R}_{\theta_{i=1,2}}^{j=1,2,3,4} \tag{4.1a}$$

$$\mathbf{R}_{i=2}^{j=1,2,3} = \mathbf{R}_1^{j=1,2,3}\mathbf{R}_{\theta_{i=2}}^{j=1,2,3} \tag{4.1b}$$

where, based on definition, $\theta_1^{j=1,2,3} \equiv 0$ when the inner tube of the segment under study is the referred one and $\theta_2^{j=1,2,3}$ is the rotation of the outer tube of each arm. For the navigation section, it is $\theta_2^{j=4} \equiv 0$ respectively. Equation (4.1a) is valid for the navigation section while (4.1b) for the manipulation sections. It is assumed that the twist of the manipulations section's inner tube with respect to the filling material is negligible. Now, the shape of the manipulation sections is given by

$$\mathbf{r}_i^{j=1,2,3} = \mathbf{r}^{j=4} + \mathbf{R}^{j=4}d_e^j, \tag{4.2}$$

where d_e^j is the eccentricity offset vector of section $j = 1, 2, 3$ in the frame of the outer tube of manipulation section and $\mathbf{R}^{j=4}$ is the rotation matrix that expresses the orientation of the navigation section.

Now, using (4.1) - (4.2) the curvature of each tube of each module can be

related to the curvature of the referred tube using the definition of $\mathbf{u}_i$ as

$$\mathbf{u}_i^j = (\mathbf{R}_i^T \dot{\mathbf{R}}_i)^\vee = \mathbf{R}_{\theta_i}^T \mathbf{u}_{i=1,2}^{j=1,2,3,4} + \dot{\theta}_i^{j=1,2,3,4} \mathbf{e}_3, \tag{4.3}$$

Equations (4.1), (4.2), (4.3) can be used to write the shape and rotation of all tubes as a function of the referred section's shape and orientation. As mentioned before, variable θ_i^j provides a parametrization of the torsion of a tube to the referred one to the section under study, which is free to vary independently as

$$\dot{\theta}_i^{j=1,2,3,4} = u_{i,z}^{j=1,2,3,4} - u_{1,z}^{j=1,2,3,4}. \tag{4.4}$$

Taking the derivative of (4.3) with respect to s it is obtained:

$$\dot{\mathbf{u}}_i^j = \dot{\theta}_i^j \frac{d\mathbf{R}_{\theta_i}^{Tj}}{d\theta_i^j} \mathbf{u}_1^j + \mathbf{R}_{\theta_i}^{Tj} \dot{\mathbf{u}}_1^j + \ddot{\theta}_i^j \mathbf{e}_3. \tag{4.5}$$

Taking into account that the model is quasistatic and the filling material is incompressible, the external force and moment exerted on the navigation section of the robot and on each manipulation section that it houses are the same. Writing the force/moment equilibrium equations with respect to s, it is obtained:

$$\begin{aligned}
&\sum_{i=1}^{n} (\dot{\mathbf{n}}_i^j + \mathbf{f}_i^j) = 0 \\
&\sum_{i=1}^{n} (\dot{\mathbf{m}}_i^j + \mathbf{e}_3 \times \mathbf{n}_i^j + \mathbf{l}_i^j) = 0
\end{aligned} \tag{4.6}$$

Using a linear constitutive law to relate the strains to moments and (4.4), (4.5) and (4.6), the derivative of curvatures can be derived as

$$\begin{aligned}
\dot{\mathbf{u}}_{1,j}\Big|_{x,y} &= -\mathbf{K}^{-1} \sum_{i=1}^{n} \mathbf{R}_{\theta_i} \Big(\mathbf{K}_{i,j} \big(\dot{\theta}_{i,j} \frac{d\mathbf{R}_{\theta_{i,j}}^T}{d\theta_{i,j}} \mathbf{u}_{1,j} - \dot{\mathbf{u}}_{1,j}^* \big) \\
&\quad + \hat{\mathbf{u}}_{i,j} \mathbf{K}_{i,j} (\mathbf{u}_{i,j} - \mathbf{u}_{i,j}^*)\Big|_{x,y} \\
&\quad - \mathbf{K}^{-1} \big(\mathbf{e}_3 \times \mathbf{R}_{1,j}^T \int_s \mathbf{f}_s(\sigma) d\sigma + \mathbf{R}_{1,j}^T \mathbf{l}\big)\Big|_{x,y},
\end{aligned} \tag{4.7}$$

where $\mathbf{K} = \sum_{i=1}^{n} \mathbf{K}_{i,j}$ is the total stiffness of the robot and $\mathbf{u}_{i,j}^{*}$ is the precurvature of each tube.

As far as torsion is concerned, it can be derived from the third component of the equation that describes the curvature for a single tube, [35],

$$
\begin{aligned}
\dot{u}_{i,j,z} = \dot{u}_{i,j}^{*} + &\frac{E_{i,j}I_{i,j}}{G_{i,j}J_{i,j}}(u_{i,j,x}u_{i,j,y}^{*} - u_{i,j,y}u_{i,j,x}^{*}) + \\
&\frac{\dot{G}_{i,j}I_{i,j}}{G_{i,j}J_{i,j}}(u_{i,j,z}^{*} - u_{i,j,z}) - \frac{1}{G_{i,j}J_{i,j}}\mathbf{e}_3 \mathbf{R}_{i,j}^{T}\mathbf{l}.
\end{aligned}
\tag{4.8}
$$

4.3 Optimization method

The equations in the above section consist a boundary value problem (BVP). The curvatures of the tubes are unknown at the entry point of the human cavity due to the long transmission and the elasticity that the system inherits. However, constraints added by the physical parameters of each tube and the system itself create the boundary conditions of the BVP.

For each transition point, the continuity of shape and internal moment must be enforced. To preserve shape continuity, it is enforced that

$$
\mathbf{g}_i(s^-) = \mathbf{g}_i(s^+)
\tag{4.9}
$$

Additionally, taking into account that there is no point load at the transition points, the static equilibrium imposes

$$
\sum_{i=1}^{n} \mathbf{m}_i(s^-) = \sum_{i=1}^{n} \mathbf{m}_i(s^+)
\tag{4.10}
$$

Moreover, at the tip of the manipulation sections the sum of the moments is considered zero in the case that no external moment is applied:

$$
\sum_{i=1}^{n} \mathbf{m}_i(s = l) = 0
\tag{4.11}
$$

Another boundary condition is related to the curvature of the inner tube of each manipulation section. At its most exerted position, its curvature should be equal to

Table 4.1: Constant Parameters Of The Tubes Used In The Experiments.

Manipulation Section - Outer Tube					
EI [Nm^2]	GJ [Nm^2]	l [m]	r_{in} [m]	r_{out} [m]	u* [m^{-1}]
0.0952	0.0732	164.3e-3	1.9e-3	2.45e-3	4.5
Manipulation Section - Inner Tube					
EI [Nm^2]	GJ [Nm^2]	l [m]	r_{in} [m]	r_{out} [m]	u* [m^{-1}]
8.2589e-04	6.3530e-04	300e-3	0	1.5e-3	16
Navigation Section - PVC Catheter					
EI [Nm^2]	GJ [Nm^2]	l [m]	r_{in} [m]	r_{out} [m]	u* [m^{-1}]
0.8259	0.6353	90e-3	1.5e-3	4.8e-3	0

the designated precurvature.

The system of equations given in (2.7), (4.1a), (4.1b), (4.2), (4.4), (4.7), and (4.8) can be solved simultaneously to calculate the shape of the moving manipulation section and the navigation section in equilibrium.

To solve for the unknown curvatures at the entry point of the system and satisfy all the boundary conditions, an optimization problem is written down and solved in Matlab$^\circledR$. The system is solved upon the minimization of the cost function that is defined as,

$$c = \sum_{=1}^{n} (u_1^j - u_1^{j*}) \tag{4.12}$$

where u_1^{j*} is the precurvature of the inner tube of the j arm.

4.4   Experimental Evaluation

Here, the experimental setup and protocol are presented. They have been used to evaluate the developed theory. In summary, a rotating PVC catheter is used as the flexible robot navigation backbone, and a pair of NiTi tubes, eccentrically arranged, form a manipulation arm.

4.4.1   Experimental Setup

The experimental setup emulates the behavior of the proposed robot, the primary difference being that the rig replicates the presence of a single manipulation arm.

The setup features a multilumen catheter made of Polyvinyl Chloride (PVC)
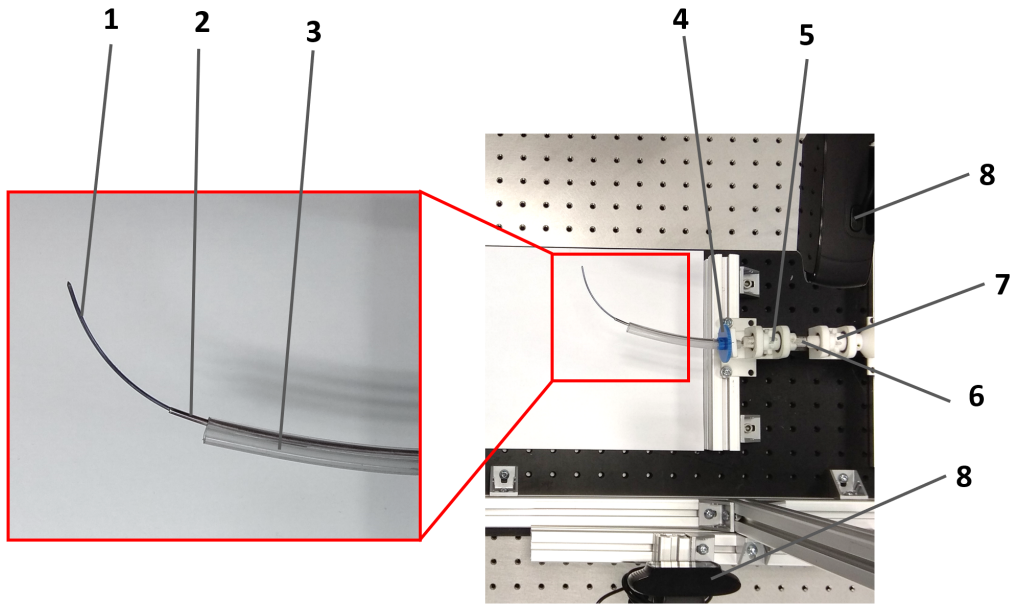
Figure 4.3: Experimental setup: (1) Manipulation section - Instrument inner rod, (2) Manipulation section - Instrument outer tube, (3) Navigation section - PVC Multi-lumen catheter, (4) Catheter rotation control, (5), (6), (7) Rotation and translation control for the manipulation section, and (8) Orthogonal camera system.

that emulates the presence of a flexible navigation section with its filling material. This section has an Outer Diameter (OD) of 9.5 mm, with three lamina arranged throughout its circumference at an angle of 120°. The Inner Diameter (ID) of each lumen is approximately 3.2 mm, allowing for the insertion of NiTi manipulation arms.

The manipulation arm comprises two tubes and is inserted through one of the three eccentrically arranged hollow lamina on the PVC catheter. The outermost tube has an OD of 2.45 mm, and carries an inner rod with a diameter of 1.5 mm. The precarvatures are known, and are given in Table 4.1 along with the remaining design specifications of the CTR.

The three tubular components of the setup (one for navigation, two for manipulation) are each mounted on rotational stages at their base. Angle markers indicate the base rotation angles. Further, the manipulation section's tubes are mounted on two carriages that lie on the same linear guide rail to allow for manual linear translation within an 80 mm range. The multi-lumen navigation section cannot translate

in this implementation.

To measure the shape of the robot, two orthogonally arranged cameras (Logitech C930e, Logitech International S.A., Lausanne, Switzerland) observing the robot workspace from the top and the side were used. The top camera view is referred to as the XY plane, while the side camera view is referred to as the YZ plane. The pixel-to-millimetre conversion rate of the cameras was calibrated prior to the experiments using a known checkerboard pattern. The experimental setup is shown in Fig. 4.3.

The proposed modeling theory focuses on predicting the position of the manipulation arm tip and the overall shape of all sections. The modeling challenge is represented by the large number of components simultaneously working and interacting with each other, leading to an increasing amount of variables to model and control. For example, pushing the instrument inner rod through one channel of the multi-lumen catheter influences the position of both its paired instrument tube, but also the catheter.

4.4.2 Experiments

To test different configurations within the rig's workspace, 9 experiments were carried out covering a range of translations and rotations of all tubular components. The experimental curvatures and lengths of the rig's tubular components were calculated using the orthogonal images. Points were captured along the entire length of the tubes, and a parametric polynomial curve was fit to approximate the total shape that was used as the ground truth. The curve was converted from 2D into 3D using the camera calibration matrix and triangulation of the selected points. All examined configurations are indicated in Fig. 4.4, where the shapes are derived from our model. Moreover, since the actual values for the moduli of the tubes and the rod are uncertain (for the NiTi they are listed as 28-83 GPa, while for the flexible PVC the Young's modulus varies from 1.5 to 15 MPa), a calibration process was followed by solving an optimization problem for the parameter set $P = \{E_i^j I_i^j\}$ of the experiment j that identifies the moduli that minimise the error between the experiment and simulation.
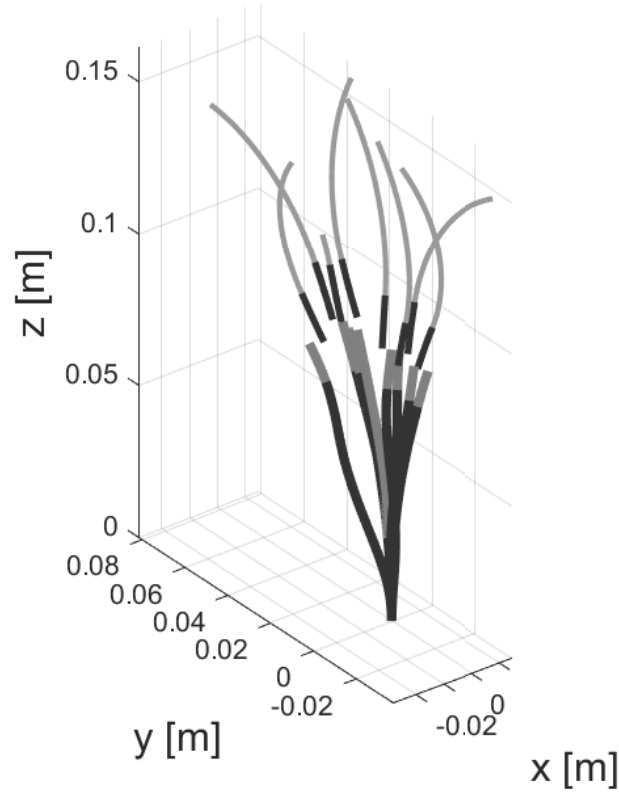
Figure 4.4: Experimentally examined configurations.

Figure 4.5 reports the experimental and simulated results for four experiments. The average error per unit length for all 9 experiments found to be 8.69% with a STD of 2.8%. The refraction caused by the PVC catheter is a potential source of error along with the clearance between the CTR arm and the PVC catheter which has not been modelled.

4.5 Conclusion

In this chapter, a new approach to model the behavior of pairs of concentric tubes that are eccentric with respect to their backbone was presented. The developed theory relates the motion of each arm of the concentric tube robot to its overall shape via an end-to-end quasistatic model. Such a model is a first step towards investigating the intricacies of multi-arm continuum robot systems based on concentric tube technology. The model showed promising results, as the average error was 8.69% of the entire manipulator length.
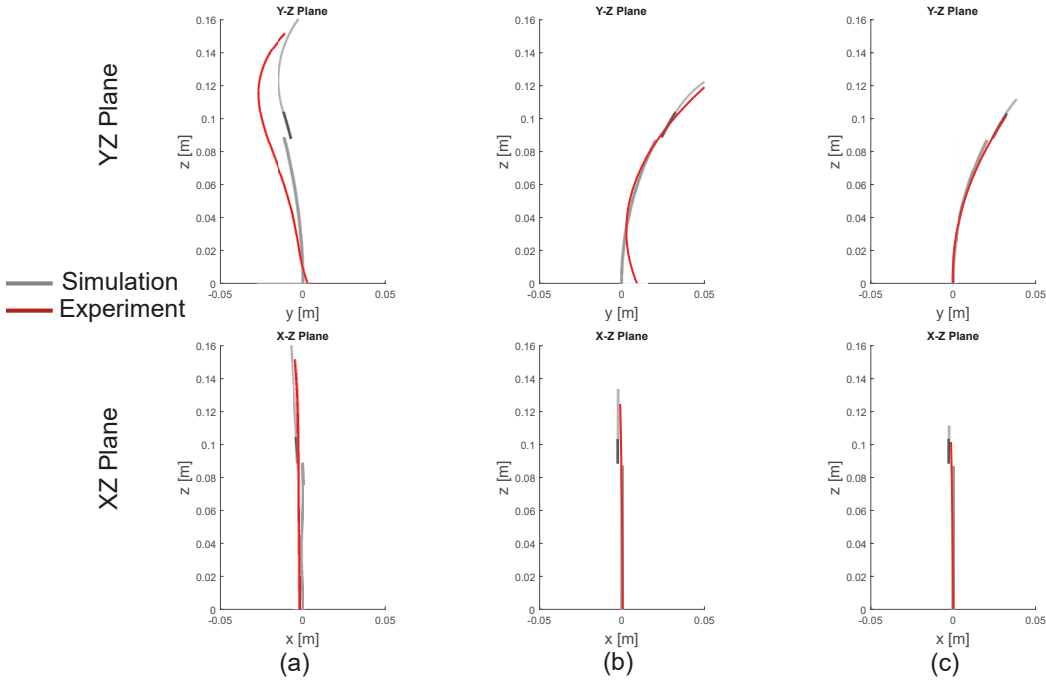
Figure 4.5: Comparison of experimental and simulated results for three experiments. The XZ, and YZ planes, are shown in the top, and bottom row, respectively. The simulated results show the centerline of the navigation and manipulation section as well as the offset between these two sections, while the experimental results show the centerline of the NiTi tubes even when they housed in the navigation section.

This work has been cited by several research groups and inspired other researchers. In [44] our contribution in extending modelling theories to account for eccentrically-arranged concentric tube arms that are housed in a flexible backbone has been recognised while in [140, 141] our work is mentioned as a representative of promising new designs of continuum robots. Moreover, this work has inspired other researchers on the design and modelling of eccentric tube robotic systems recognising the promise of this new continuum robot [142, 143].

Nevertheless, limitations have been identified in this design option. It has been observed that NiTi tubes, with a diameter equal to the one needed to build the navigation section, are difficult to be bent. Anisotropic patterning derived from a design optimization algorithm can be employed to minimize the stiffness of the NiTi tubes, however such an endeavor is not a part of this dissertation and has been left as future work.

Chapter 5

Hybrid Continuum Multi-Arm Robots

This chapter describes the development of a new type of continuum robot whose architecture combines the flexibility of a push/pull actuated continuum robot and the dexterity offered by concentric tube robotic end-effectors. Here, the design of a prototype system as a proof-of-concept and a tailored quasistatic mechanics-based model are presented. The model describes the shape and end-effector's pose of the new type robotic architecture. The design is an alternative to the design option presented in Chapter 4 as the push/pull technology can be employed to get a flexible backbone.

The primary contributions of this chapter are: 1) the development of a mechanics-based quasistastic kinematic model for the proposed hybrid continuum robot, considering an arbitrary number of push/pull actuated bending segments and CTR arms, and 2) a continuum robot prototype comprising of one push/pull actuated segment and 3 CTR arms. The prototype was employed for the experimental evaluation of the proposed model in loaded and unloaded cases. The majority of this chapter is adapted from a paper submitted in the *IEEE International Conference on Robotics and Automation* in 2022 entitled "Design and Quasistatic Modelling of Hybrid Continuum Multi-Arm Robots" [5].

5.1   Introduction

Hybrid systems can combine the advantages of both categories and overcome their constraints. The push/pull technology can offer the advantage of accessing all the workspace and be used as a driving backbone while concentric tube technology can offer increased dexterity and flexibility in confined space in the last step of an intervention. Building on our and recent work on eccentric tube robots [3, 142, 143], a multi-arm hybrid continuum robot was designed, prototyped, modelled, and experimentally evaluated. Its navigation section, responsible for anatomy navigation and coarse positioning of the robot tip, is a push/pull actuated section comprising NiTi rods and a backbone on which fixtures with holes are rigidly connected. In contrast to a cable driven system, the proposed design offers more bending curvature as the rods, because of their greater diameters, can be also pushed. Its manipulation section, responsible for performing the surgical task, comprises of CTR arms, passing through the fixtures' holes. The proposed architecture combines the flexibility and capability for conformance to the anatomy of multibackbone robots be combined with the tip dexterity offered by CTRs.

This kind of robot can be used in deep orbital interventions and more specifically in ONSF [2] but also in interventions where increased flexibility is needed alongside limited workspace. A flexible navigation section, as the proposed push/pull section, can substitute the collimator presented in Chapter 3 and the variable stiffness of CTR presented in Chapter 4. It promises to enhance the workspace and the dexterity of the multi-arm system.

5.2   Modeling and Theoretical Analysis

This section presents a mechanics-based kinematic model for the proposed hybrid continuum robot architecture, shown in Fig. 5.1, based on the Cosserat-rod theory [128]. The proposed model can be used in small scale movements, as those in robotic surgeries, in contrast to the model of [7] which is a geometric one and its accuracy is low mainly due to the effect of constant curvature. To derive the model, we employ the assumptions of the classical elastic-rod theory of Kirchhoff [35]:
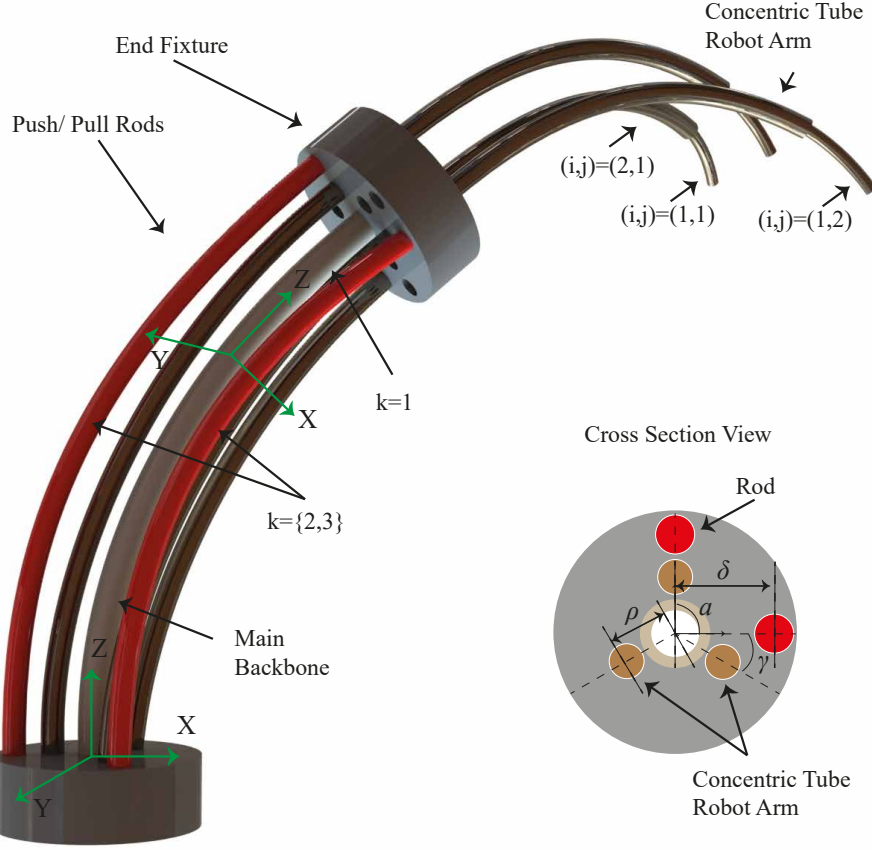
Figure 5.1: Schematic of the continuum robot with one bent segment and three eccentrically arranged concentric tube robot (CTR) arms. Each arm comprises two nitinol tubes. The central backbone of the push/pull segment is modelled as a Cosserat rod. The cross section unit depicts the position of the push/pull rods and the CTR arms with respect to the central backbone.

- The backbone, the rods and the tubes are axially rigid and no cross-sectional shear deformation is presented.

- Deformation of the tubular components is entirely due to bending.

- The fixtures, shown in Fig. 5.1, are rigid. They are perpendicular to the central backbone while their holes are big enough for the CTR arms to pass.

- The weight of fixtures, central backbone, rods and CTR arms is negligible and not taken into account.

Here, the subscript $j = 1, \cdots, N$ denotes the CTR arm of the robot referred to within the equations, while subscript $i = 1, \cdots, N$ the ith tubular component. The tubular components of the push/pull section is denoted by $k = 1, \ldots, N$, with $k = 1$
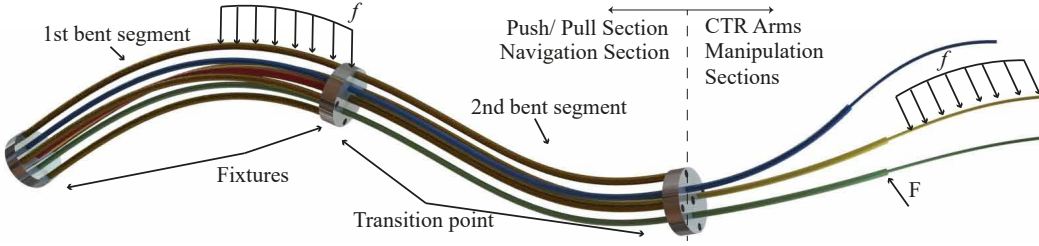
Figure 5.2: Schematic of a multi-backbone robot with two bending segments and three CTR arms, all under an arbitrary external distributed force.

referring to the backbone of the navigation section. A schematic of the proposed hybrid multi-arm continuum robot architecture is shown in Fig. 5.1 and Fig. 5.2. The relative position of each rod of the navigation section and each CTR arm with respect to the backbone is:

$$\mathbf{d}_k = [\delta_k\cos(\beta_k), \quad \delta_k\sin(\beta_k), \quad 0]^T,$$
$$\mathbf{p}_j = [\rho_j\cos(\beta_j), \quad \delta_j\sin(\beta_j), \quad 0]^T, \tag{5.1}$$

where δ_k, ρ_j are the distances of the rods, and CTR arms, from the robot's central backbone, respectively. Variables β_k, β_j are the angles of each push/pull rod, and CTR arm, with respect to the central backbone. While not necessary, angularly distributing the rods and CTR arms is a sensible design choice:

$$\beta_k = \gamma + (k-2)\gamma_{rod}, \quad k \neq 1,$$
$$\beta_j = \alpha + (j-1)\frac{2\pi}{n}, \tag{5.2}$$

with α and γ shown in Fig. 5.1 and n the number of CTR arms and γ_{rod} the angle between two subsequent rods. The position and orientation of the central backbone is defined as:

$$\dot{\mathbf{r}}(s) = \mathbf{R}(s)\mathbf{e}_3, \quad \dot{\mathbf{R}}(s) = \mathbf{R}(s)(s), \tag{5.3}$$

where $\mathbf{u}(s) = [u_x(s), u_y(s), u_z(s)]^T$ is the curvature vector of the deformed backbone and comprises the kinematic variables of the modelling problem. The unit vector, $\mathbf{e}_3 = [0, 0, 1]^T$, is aligned with the z-axis of the global coordinate frame.

Transition points divide the robot's length into segments as is shown in Fig. 5.2.

The transition points here are where a tube goes from straight to curved, where a tube or a push/pull segment ends and where the push/pull section ends and the CTR arms begin. Segments and sections are later connected to each other by enforcing the continuity of shape and internal moment.

To derive the curvature of the central backbone in the navigation section, the derivatives of the force and moment balance with respect to the arc length s are calculated as in [35]:

$$\sum_{k,i,j=1}^{n} \left(\dot{\mathbf{n}}_{k,i,j} + \mathbf{f}_{k,i,j} \right) = 0,$$
$$\sum_{k,i,j=1}^{n} \left(\dot{\mathbf{m}}_{k,i,j} + \mathbf{e}_3 \times \mathbf{n}_{k,i,j} + \mathbf{l}_{k,i,j} \right) = 0. \tag{5.4}$$

where $\mathbf{m}, \mathbf{n}$ are the internal moment and force respectively while $\mathbf{f}, \mathbf{l}$ are distributed force and moment respectively. A linear constitutive law is employed to relate the kinematic variable $\mathbf{u}$, to the derivative of the internal moment, $\dot{\mathbf{m}}$:

$$\mathbf{m} = \mathbf{K}(\mathbf{u} - \mathbf{u}^*), \tag{5.5}$$

where $\mathbf{u}^*$ is the precurvature of the ith tube of the jth arm.

After manipulation and dropping s for simplicity, the differential equation of the backbone's curvature becomes:

$$\dot{\mathbf{u}}_{k=1} = -\mathbf{K}^{-1} \Bigg[\sum_{k=1}^{n} [\mathbf{u}]_{\times} \mathbf{K}_k \mathbf{u}_{\mathbf{k=1}} + \sum_{j=1}^{n} \sum_{i=1}^{n} \mathbf{K}_{i,j} \theta_{i,j}$$
$$\frac{\mathrm{d}\mathbf{R}_{\theta_{i,j}}^{T}}{\mathrm{d}\theta_{i,j}} \mathbf{u}_{\mathbf{k=1}} + [\mathbf{u}_{i,j}]_{\times} \mathbf{K}_{i,j} (\mathbf{u}_{i,j} - \mathbf{u}_{i,j}^*) \tag{5.6}$$
$$+ [\mathbf{e}_3]_{\times} \mathbf{R}^{T} (l-s)f + \mathbf{R}_1^{T} \mathbf{l} \Bigg].$$

In (5.6), $\mathbf{K}_{i,j}$ and $\mathbf{K}_k$ are the stiffness matrices of each CTR tube and push/pull rod respectively, while $\mathbf{K} = \mathrm{diag}(EI, EI, GJ)$ is the stiffness matrix for the whole robot; E is the robot's Young's modulus; I is the second moment of inertia; G is the shear modulus; J is the polar moment of inertia and l is the length of the central backbone. It should be noted that the cross section of the robot is symmetric and

the products of inertia are negligible (*i.e*, $I_{xy} = I_{xz} = I_{yz} \simeq 0$).

Please note that the rods of the navigation section are rigidly connected to the last fixture of the segment that they actuate. As a result, they do not experience torsion. On the other hand, the tubes that comprise the CTR arms can freely pass from the fixtures' holes. We employ an angle, $\theta_{i,j}$ to model the relative rotation of the *i*th tube of the *j*th arm with respect to the central backbone.

The torsion of each CTR tube can be derived from the third component of the equation that describes the curvature for a single tube [35]:

$$
\begin{aligned}
\dot{u}_{i,j,z} = {}& \ddot{u}^*_{i,j} + \frac{E_{i,j}I_{i,j}}{G_{i,j}J_{i,j}}(u_{i,j,x}u^*_{i,j,y} - u_{i,j,y}u^*_{i,j,x}) + \\
& \frac{\dot{G}_{i,j}I_{i,j}}{G_{i,j}J_{i,j}}(u^*_{i,j,z} - u_{i,j,z}) - \frac{1}{G_{i,j}J_{i,j}}\mathbf{e}_3\mathbf{R}^T_{i,j}\mathbf{l}.
\end{aligned}
\tag{5.7}
$$

The resulting curvature of the pull/pull segment $\mathbf{u}(s)$ and position $\mathbf{r}(s)$ are unknown and are estimated as the function of the length tubes of the navigation section. The total arc length of each rod can be estimated as:

$$
\ell_k = \int_0^l \|\dot{\mathbf{r}}_k(s)\| \mathrm{d}s,
\tag{5.8}
$$

where $\|.\|$ denotes the ℓ_2-norm and $\mathbf{r}_k(s)$ is the position of kth rod given by

$$
\mathbf{r}_k(s) = \mathbf{r}_{k=1}(s) + \mathbf{R}(s)\mathbf{d}_k.
\tag{5.9}
$$

Substituting (5.9) in (5.8) and simplifying the equations using (5.3) yields

$$
\ell_k = \int_0^l \|\mathbf{e}_3 + \mathbf{d}_k\| \mathrm{d}s.
\tag{5.10}
$$

The shape of each tubular component belonging to one of the CTR arms is given by:

$$
\mathbf{r}_{i,j}(s) = \mathbf{r}_{k=1}(s) + \mathbf{R}(s)\mathbf{p}_j.
\tag{5.11}
$$

To get the shape of the CTR arms, the end position and orientation of the central backbone of the navigation is employed to define the initial posture of the

CTR arms as well as the torsion of the previous section along with tube's angle, $\theta_{i,j}$. Following the approach of [35], the curvature of the most exerted tube of the jth arm is:

$$\dot{u}_1 = -\mathbf{K}^{-1} \sum_{i=1}^{n} \mathbf{R}_{\theta_i}(\mathbf{K}_i(\frac{\mathrm{d}\mathbf{R}_{\theta_i}^T}{\mathrm{d}\theta_i}\mathbf{u}_1 - \dot{\mathbf{u}}_i^*) + [\mathbf{u}_i]_\times \mathbf{K}_i$$
$$(\mathbf{u}_i - \mathbf{u}_i^*) - \mathbf{K}^{-1}([\mathbf{e}_3]_\times R_1^T \int_s \mathbf{f}_s(\sigma)\mathrm{d}\sigma + \mathbf{R}_1^T \mathbf{l}). \tag{5.12}$$

In (5.12) we dropped the subscript j^{th} for simplicity. The torsion of each tube is described in (5.7).

Equations (5.3), (5.6), (5.7), (5.8) and (5.12) comprise the system of differential equations governing the motion of the robot. The system of equations are solved as a boundary value problem with the following boundary conditions:

$$\mathbf{r}(0) = [0\ 0\ 0]^T, \tag{5.13a}$$

$$\mathbf{R}(0) = I, \tag{5.13b}$$

$$\ell_{\mathbf{k}}(\mathbf{0}) = 0, \tag{5.13c}$$

$$\ell_{\mathbf{k}}(\mathbf{l}) = L_k,\ k \neq 1, \tag{5.13d}$$

$$\mathbf{u}_{i,j}(s = \ell) = \mathbf{u}_{i,j}^*. \tag{5.13e}$$

Additional constraints arise from the continuity that should be enforced at the bending segments and at the transition points of the CTR arms. The appropriate conditions across each transition point should be enforced and are defined as:

- the position and orientation of the backbone and each CTR arm must be continuous *i.e.*,

$$\mathbf{r}(s^-) = \mathbf{r}(s^+),\ \ \mathbf{R}(s^-) = \mathbf{R}(s^+), \tag{5.14}$$

- the torsion of each arm's tubular component should be continuous across its length around z direction:

$$u_{z,i,j}(s^-) = u_{z,i,j}(s^+), \tag{5.15}$$

- the balance of moment should be respected:

$$m_{z,i,j}(s^-) = m_{z,i,j}(s^+). \tag{5.16}$$

5.2.1   Solution Approach

The model is defined by (5.3), (5.6), (5.7), (5.8) and (5.12) with the boundary conditions and constraints described in (5.13), (5.14), (5.15) and (5.16). It accepts the overall length of the rods that comprise the navigation section of the robot $\mathbf{L}_k$ as inputs and computes the shape of the central backbone. It also accepts the length of tubes that comprise the CTR arm so to get the shape of the rest of the tubular components. However, while the initial curvature along x and y direction *i.e.* $\mathbf{u_{xy}}(0)$ is unknown, the length of the rods of the push/pull segments are known and defined both at the base ($s = 0$) and the end of each segment. In addition, the curvature of the CTR arms at the end of the navigation section is unknown, with the curvature at its distal point known and equal to the precurvature of the most exerted tube.

The model presented in Sec. 5.2 is quasi-static and solved using the separation of variables. Such an approach is acceptable in cases where the velocity and acceleration of the system is low and dynamic phenomena are avoided.

The differential equations can be solved using standard methods such as the Runge-Kutta family of algorithms, while the boundary value problem can be solved by non-linear root-finding (shooting) methods.
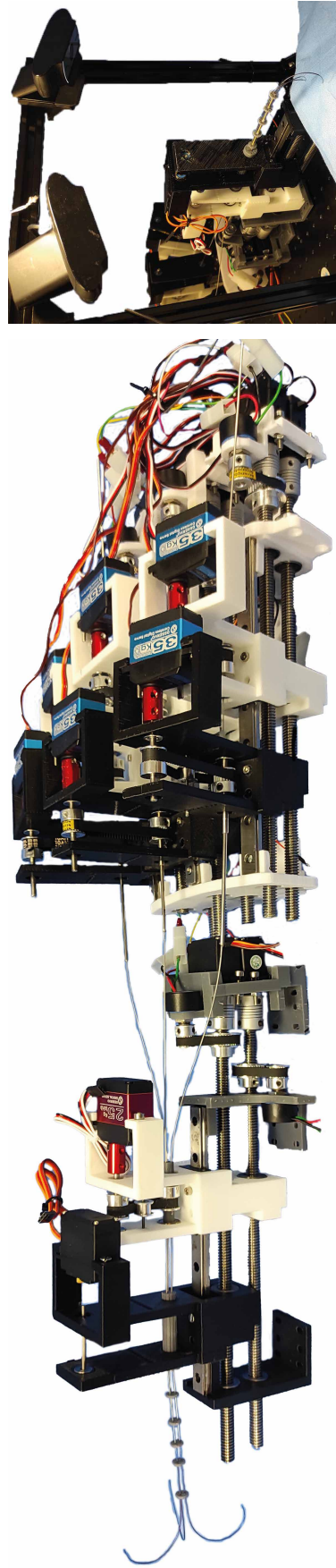
Figure 5.3: Left: The developed robot prototype. The actuation unit comprises the subsystem for the actuation of the manipulation arms and the subsystem for the actuation of the navigation section. Each CTR arm is actuated by an identical module. **Right:** The stereo vision system used to capture the end-effector's shape to verify the theoretical model.

5.3   System Design and Prototyping

This section describes the design and engineering of the robotic system prototype. The system was designed for the evaluation of the proposed theoretical work and consists a proof of concept for the ultimate employment of hybrid robotic systems for surgical interventions. The system comprises one bending push/pull segment and up to 3 CTR arms. Figure 5.3 shows the developed robotic system while important robot's dimensions are shown in Table 5.1.

The navigation part of the end-effector is a 2 DoF segment section that is actuated by two NiTi tubes with outer diameter (OD) of 0.69 mm and inner diameter (ID) of 0.45 mm, which are passed through holes located on fixtures. The fixtures, with a diameter of 9 mm, are employed to guide the manipulation arms and avoid buckling of the tubes. They were 3D-printed by Formlabs Form 3B. A PVC rod shown in beige in Fig. 5.1 is acting as the central backbone. It has a diameter of 2 mm and is rigidly connected to the fixtures to ensure that they cannot move relative to each other. The length of the navigation section is 83 mm.

The tubes are actuated by continuous RS motors (SRC SM-S4315R) with a maximum torque of 1.47 Nm. The translation of each tube is monitored via the employment of linear, continuous turn, rotary potentiometers. The motors are connected to lead screws which convert the power generated by the motors to linear velocity of the push/pull tubes. The motors are connected to the lead screws via the employment of flexible couplings to absorb also any possible misalignment. The lead screws are carrying 3D printed parts, printed in a WASP 2040 with PLA material, that are connected rigidly to the push/pull tubes.

The manipulation section can accommodate up to 3 concentric tube robot arms. It was chosen to employ 3 CTR arms based on the discussion of the clinical requirements of ONSF. In any intervention, it is preferred to be able to have bimanual manipulation and the ability to visualize the tools and the area of surgical interest. It is envisioned that one arm will be able to hold a camera while the other two a surgical tool. Each arm comprises an outer tube and an inner rod, both made of NiTi. The outermost tube has an outer diameter of 0.67 mm and inner diameter of

Table 5.1: Physical parameters of the robot.

$l_{k=1}$	83 mm	E_{NiTi}	80 MPa
l_{11}	46 mm	G_{NiTi}	15 MPa
l_{12}	41 mm	$D_{innerrod}$	0.33 mm
l_{21}	47 mm	OD/$ID_{outertube}$	0.69/0.45
l_{22}	35 mm	$D_{k=1}$	2 mm
$u'_{outertube}$	1/0.043 m^{-1}	OD/$ID_{tubepush/pull}$	1.2/0.8
$u'_{innerrod}$	1/0.031 m^{-1}	$D_{fixtures}$	9 mm

0.45 mm while the diameter of the rod is 0.33 mm. Both tubular components are precurved with the outer tube precurved at approximately 23 m^{-1} and the inner one with a precurvature of around 32 m^{-1}.

Each tubular component is able to be rotated and translated independently. Continuous RS motors (SRC SM-S431R) are employed for the translation of each tube while servo motors (DS3235) with maximum torque of 3.43 Nm and range from $0° - 270°$ are selected for the rotational DoFs. Stainless steel (SS) tubes are selected for the transmission of the manipulation arms. It is chosen to limit the length of the NiTi by gluing it to a straight and stiffer SS tube, reducing the torsional effect which can result to snapping which is the sudden motion of the tubes from one configuration to another due to accumulation of energy. As the SS tubes are stiffer than the NiTi tubes, the danger of having snapping is minimized. The translational DoF is monitored by continuous turn, linear potentiometers while for the rotational DoF a timing belt is used. Timing belts can retain the compactness of a system however they come with the problem of backlash. To avoid such an effect, a pretenser is employed to adjust the pretension of the timing belt.

5.4 Experiments & Theoretical Analysis

Experiments were performed with the prototype to evaluate the model developed in Sec. 5.2. It was preferred to accommodate here two CTR arms instead of three for facilitation of data analysis and assembly of the end-effector. The model's fidelity was examined considering various configurations with and without load.
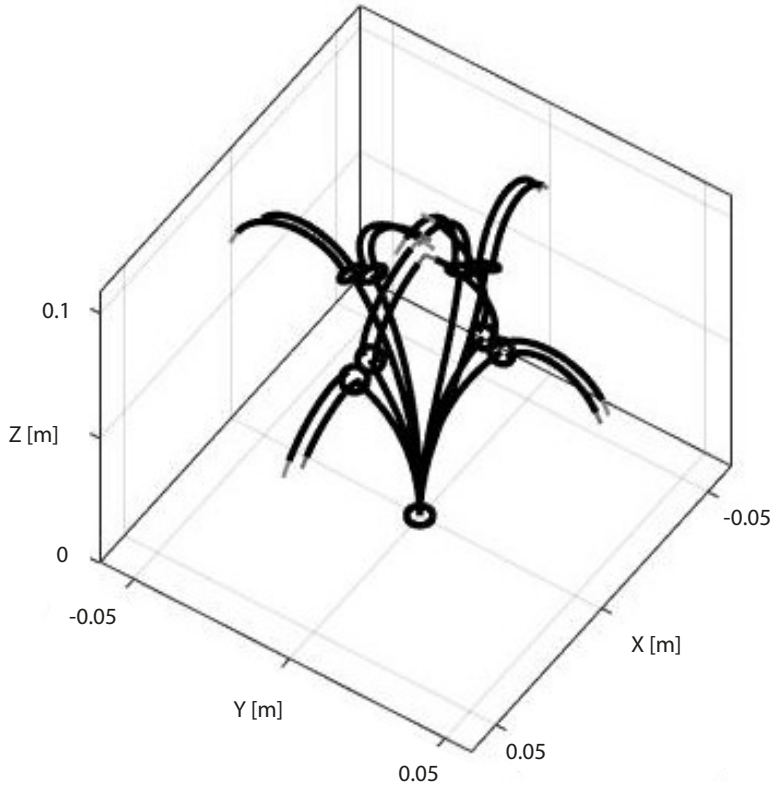
Figure 5.4: Workspace of the hybrid robot for actuation input of 1.5 mm and 2 mm in each rod's direction.

5.4.1 Workspace Analysis

Each rod of the push/pull section was actuated by an arbitrary value to showcase the robot's workspace for that value. Here, we chose to actuate each rod (push and pull) by 1.5 mm and 2 mm and rotate each arm by $180°$. Figure 5.4 showcases the configurations of the hybrid end-effector for those values. Different values of actuation of the push/pull section can eliminate the interior boundary of the workspace and achieve a convex workspace as can be seen by Fig. 5.4. Through the actuation of the push/pull section, the CTR arms can reach with enhanced dexterity regions close to vertical axis of the end-effector as well as far away from it.

5.4.2 Stereo Vision System

The accuracy of the proposed model was evaluated using a stereo pair setup (Logitech HD Pro C922), shown in Fig. 5.3. The stereo pair was calibrated using MAT-
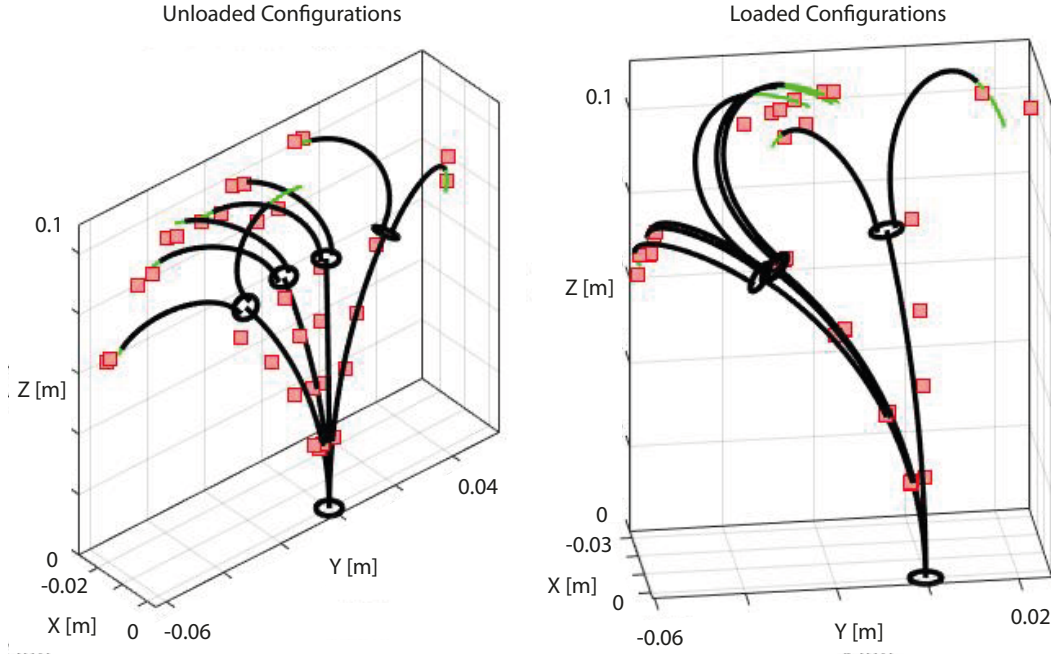
Figure 5.5: The shape of the central backbone and two CTR arms derived via simulations for 4 configurations with (left) and without (right) load. The red markers show the actual position of the fixtures and tubes' end for each configuration.

LAB's calibration toolbox. The mean reprojection error attained for each camera was 0.33 pixels.

To estimate the error of the developed model, sequences of image pairs were captured in which the robot was actuated by a different value. For each image pair, 4 distinct corresponding points in the images were manually selected and stereo triangulation was performed using the Direct Linear Transformation [144]. This resulted in a set of initial 3D points, which were then refined by minimising the reprojection error on each image pair. Each of the point that was selected corresponded to the end of each tubular component of the CTR arms. A point corresponding to the most proximal point of the end-effector was selected as reference point while the axis were rotated to manage the coordinate frame of the simulations (the z axis is tangent to the central backbone) .

5.4.3 Unloaded Experiments

We captured 38 different robot configurations without external loads on the robot. For each configuration, the translation of the tube's carriage under actuation was

Table 5.2: Experimental Results. Maximum error of tip position (e_{max}), mean error of tip position (e_{mean}), standard deviation of error (σ), and root mean squared error (RMSE) are reported. All the errors are normalized per unit length

	$\%e_{max}$	$\%e_{mean}$	σ	RMSE
Unloaded exp.	7.64	3.64	1.62	3.98
Loaded exp.	7	3.47	1.14	3.65

measured and imported as input to the model. The experimental position of each one of the CTR arms was measured via the stereo vision system and compared to the simulated one.

Results of the measurements including maximum, mean, standard deviation of error of the model in predicting the robot's shape and the root-mean-squared error of the model are listed in Table 5.2. Figure 5.5 shows that the simulated shape of the central backbone and CTR arms can capture well the actual position of the fixtures and tubes' end. It should be noted that all the errors are normalized with respect to the length of the end-effector. The root-mean-squared error is calculated as

$$\text{RMSE} = \sqrt{\frac{\sum_{j=1}^{m}(\|\hat{\mathbf{r}} - \mathbf{r}\|_j)^2}{m}}, \tag{5.17}$$

and is used as a measure of the differences between the actual shape of the robot, $\hat{\mathbf{r}}$, and the model predicted shape.

The mean error per unit length was found to be 3.64%, attaining a maximum of 7.64% and standard deviation of approximately 1.63%. Figure 5.5 depicts the shape of the central backbone via simulations. There, the red markers show the position of the fixtures as derived by the stereo vision system. It can be observed that the developed model can also predict the shape of the push/pull section. Figure 5.7 shows the statistical analysis of the errors.

5.4.4 Loaded Experiments

To demonstrate the capability of the model to capture the shape of the end-effector under external forces, a set of 32 experiments with a distributed force and a point
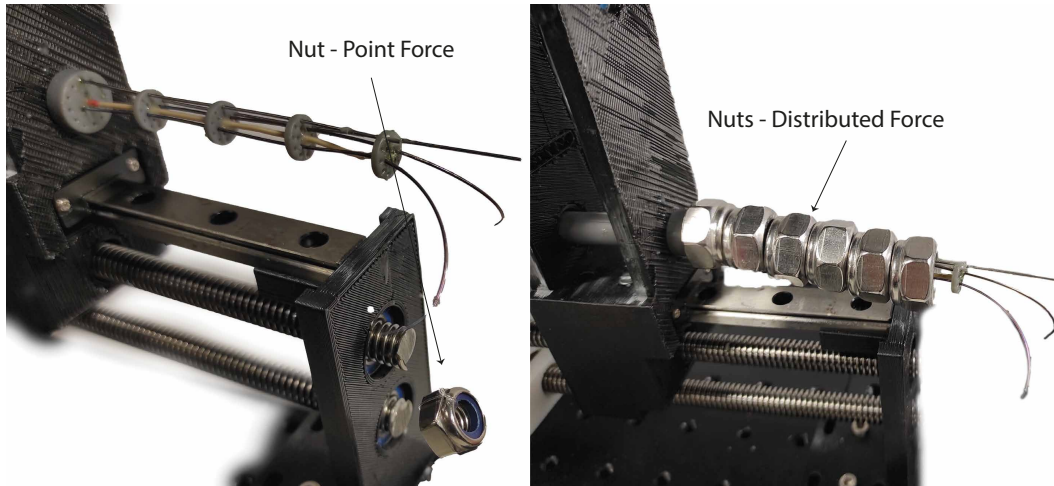
Figure 5.6: The experimental setup to simulate external forces. **Left:** Weight in the end of the outer tube of the right arm, **Right:** Distributed weight on the navigation section.

force on the outer tube of the right arm was performed. The weight of the end-effector is negligible and does not lead to noticeable deformation for that reason a number of nuts were employed which were placed along the length of the push/pull segment as can be seen in Fig. 5.6 to simulate external distributed force. The overall weight of the nuts was approximately 87 grams in the first 5 experiments and 73 grams in the rest 11 experiments. The motion of the nuts along the backbone during its "bending" was on the order of 1mm, therefore not noticeably affecting force distribution. The points of interest for model evaluation where never covered by nuts. A final set of 16 experiments were run with a point force on the outer tube of the right CTR arm. For this reason a nut weighted 4.7 grams was employed to emulate the point force. Table 5.2 shows the error in the loaded experiments. The mean error in the loaded experiments found to be 3.47% per unit length, close to the state of the art models for non-hybrid robots. Figure 5.5 shows that the model can predict the actual shape of the end-effector under loaded conditions too.

5.5 Conclusion

In this chapter, the design and modelling of a novel continuum robot was presented. It is a hybrid continuum robot combining push/pull and concentric tube technology. This miniaturized single-port system is able to deliver multiple arms through
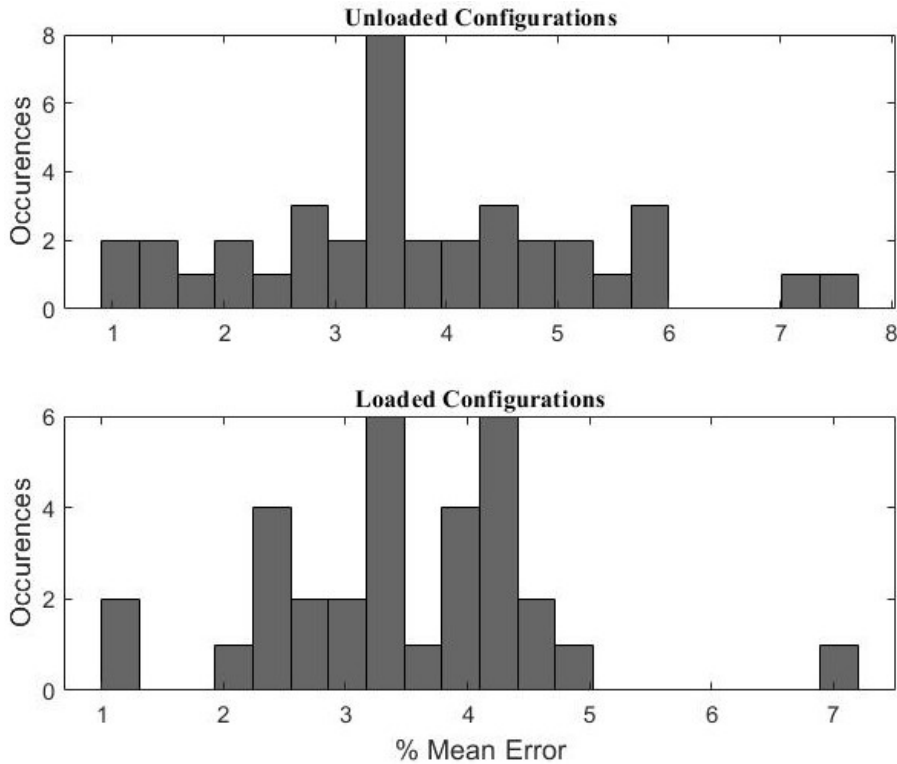
Figure 5.7: Histogram of the mean error for the unloaded configurations (above) and for the loaded cases (bottom).

a push/pull actuated segment. The hybrid multi-arm continuum robot promises to make interventions less invasive as it combines the stiffness of a push/pull system with the dexterity and the small diameter of CTRs. To prove the concept of a hybrid robot, a system with a 2 DoF push/pull segment and 3 CTR arms was designed with each one of them comprising two NiTi tubes with 4 DoF in total. It is envisioned that this kind of robot can be used in interventions in which a flexible navigation section is required to achieve enhanced dexterity and flexibility. Moreover, this new design option is easier to be implemented with respect to the one presented in Chapter 4 as there is not a need to bend NiTi tubes with a large diameter. Push/pull technology has more advantages than concentric tube technology as far as the creation of a navigation section in a multi-arm continuum robot is concerned. It has been shown in Chapter 5.4.1 that push/pull technology can also achieve coverage of convex workspaces in contrast to concentric tube technology which cannot.

Also, a new model for the hybrid continuum robot was developed and pre-

sented. The model is based on the Cosserad-rod theory and can predict the overall shape of the end-effector via an end-to-end quasistatic model. The developed theory can model the robot's end-effector with an overall error (taking into account the loaded and unloaded cases) of 3.56% per unit length as can be seen from the statistical analysis in Fig. 5.7.

Chapter 6

A Continuum Robot for Distal Lung Sampling

In this chapter, the development of a continuum robotic system based solely on the push/pull technology is presented so to showcase the advantages that this technology has too. Here, the design and development of the first robotic bronchoscope for sampling of the distal lung in mechanical-ventilated (MV) patients in critical care units (ICU) based on push/pull technology is described. The chapter showcases the advantages that this technology has and presents a new detailed mechanics-based model of a robot employing this technology.

Despite the high cost and attributable morbidity and mortality of MV patients with pneumonia which approaches 40%, sampling of the distal lung in MV patients suffering from range of lung diseases such as Covid-19 is not standardised and requires expert operators. Here, the previous design options are extended into the design of a robotic bronchoscope that enables access of deep seated pathologies and coverage of all regions inside the bronchial tree.

The majority of this chapter is adapted from a paper published in the *Frontiers in Robotics and AI* in 2021 entitled "Design and Modelling of a Continuum Robot for Distal Lung Sampling in Mechanically Ventilated Patients in Critical Care" [6].

6.1   Introduction

Critically ill patients who develop respiratory failure and require MV suffer a high morbidity and mortality. Indeed, Covid-19 patients who require MV, have a mortality approaching 40% in some case series. Once MV, patients are at high risk of developing secondary infections and other secondary complications. Sampling of the distal lung is an important diagnostic procedure to guide therapeutic interventions. However, endobronchial secretions such as mucus and often hinder manually steered bronchoscopes lead to poor sampling results due to limited dexterity and flexibility of the surgical instrument. Hence, the aim of this chapter is to develop a robotic bronchoscope that democratises sampling of the lung in MV ICU patients and enables non-skilled operators to safely sample disparate regions of the human lung to improve diagnostic accuracy and therapeutic interventions.

Bronchoscopy is a common diagnostic modality for the early detection of lung diseases (see Fig. 6.1). During bronchoscopy, a thin tube (bronchoscope) is passed through the nose or mouth into the airways to reach potential regions of the lung for directed sampling. Due to relatively large dimensions of the bronchoscope used for sampling ($> 5\,\text{mm}$), bronchoscopy of MV patients is challenging. Another major drawback of the current technology is reliance on manual insertion, which is difficult due to the limited Degrees of Freedom of the bronchoscope, *i.e.*, rotation and insertion.

To address the aforementioned challenges, a miniaturized continuum robot is been developed for lung bronchoscopy. The proposed bronchoscope is a continuum robot comprising several parallel rods that can be bent via pushing/pulling of the rods. A continuum robot composed of several constrained push/ pull rods is commonly known as a *multi-backbone robot*, first introduced in [145]. Simaan *et al.* introduced the first surgical multi-backbone robot for dexterous tool manipulation in robotics surgery [146, 147].

A major challenge in the deployment of miniaturized continuum robots is precise modelling. There are several different kinematic and dynamic models presented in the literature (see [26] for a detailed review). The most common model for multi-
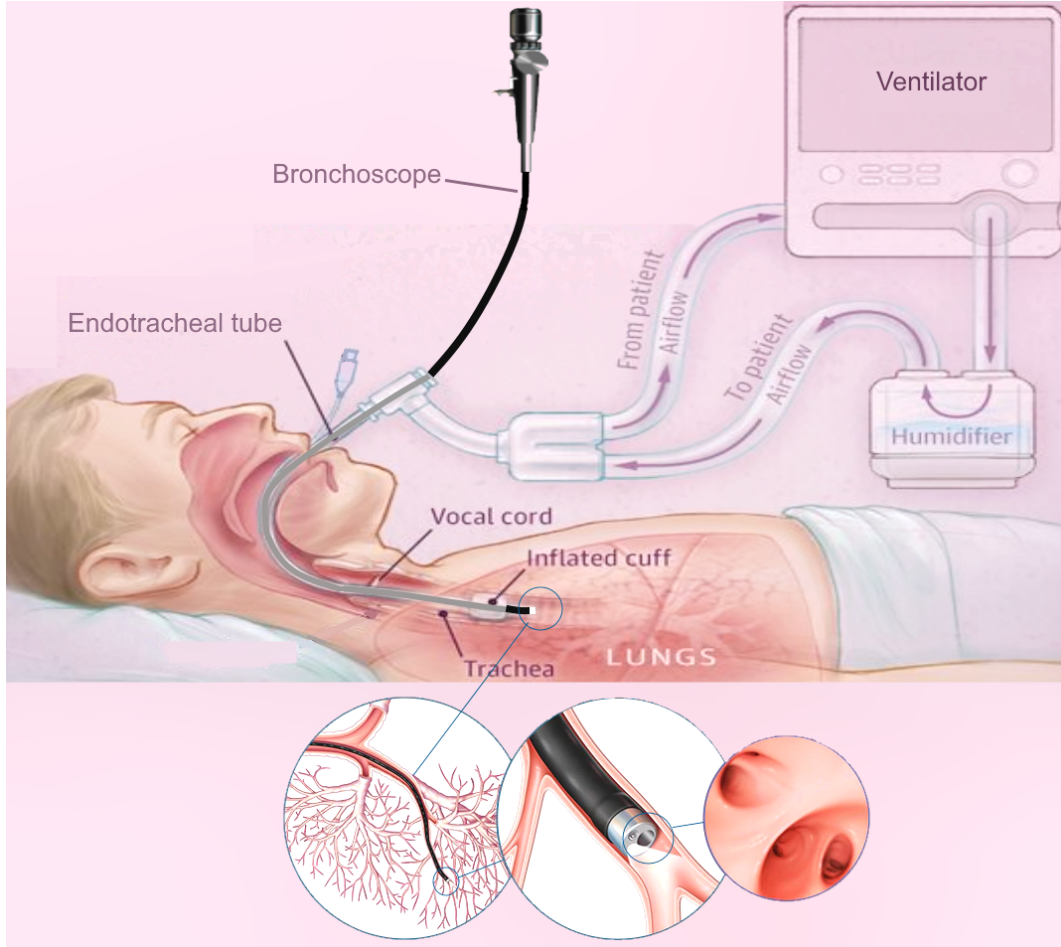
Figure 6.1: A schematic of lung bronchoscopy in ICU, showcasing the insertion of the robotic bronchoscope through the mechanical ventilator and inside the lung.

backbone robots is a geometric model proposed in [146]. The model has been used to control the motion of the robot as well as contact forces at the robot's tip [7]. The geometric model assumes the robot curvature is constant and provides an accurate description of the robot's differential kinematics for large scale movements. However, due to the effects of unknown boundary conditions and the constant curvature assumption, the model's prediction of the robot shape and micro-scale movements are not accurate. To overcome this challenge, Del Giudice *et al.* [148] proposed a method to improve micro-scale motion of a multi-backbone robot using modulation of the flexural rigidity of the rods. Another common method for modelling of multi-backbone robots is Cosserat rod theory [8, 149] however, most models are computationally expensive. As a result, less accurate modeling methods are still

attractive due to their low computational cost [7, 150].

In this chapter, a bronchoscope is developed using a miniaturized multi-backbone robot. The bronchoscope is mounted on a linear stage that can be used to automatically insert/ retract the bronchoscope to reach targeted positions in the distal lung. Next, a geometrically exact model of the robot is developed that considers both the geometry of the robot and mechanical properties of the backbones. The model results in a reduced order BVP and can be used to predict the shape of the bronchoscope without the constant curvature assumption.

In the next section, the robot architecture and bronchoscope design is presented while Sec. 6.3 details the model of the bronchoscope. In Sect. 6.4, simulations and experimental results are performed to evaluate the design and quantify the accuracy and computational efficiency of the model.

6.2   System Design and Prototyping

This section describes the design and engineering of the robotic bronchoscope. The mechanical system design begins with a DoFs discussion. To improve the dexterity of the bronchoscope, a novel design is proposed that allows the robotic bronchoscope to bend in 3D at two points. The tip of the bronchoscope is composed of two segments shown in Fig. 6.2. Each segment is actuated by 3 NiTi rods with an outer diameter of 0.475 mm which are passed through holes located on fixtures surrounding the bronchoscope. The circular fixtures are employed to avoid buckling of the rods. An additional silicone rod shown in blue in Fig. 6.2 is acting as the main backbone. It has an outer and inner diameters of 2.3 mm and 2 mm, respectively and is rigidly connected to the fixtures to ensure they cannot move relative to each other. The fixtures' outer and inner diameters are 4.5 mm and 2.4 mm respectively. The length of the proximal segment at the tip of the bronchoscope is 40 mm, the length of the distal segment is 500 mm, and the overall length of the bronchoscope is 540 mm. The end-effector is actuated via the push-pull of the 6 rods. In contrast to the cable driven bronchoscopes, the proposed design employs incompressible NiTi rods to offer more bending curvature via pushing of the rods. Furthermore,
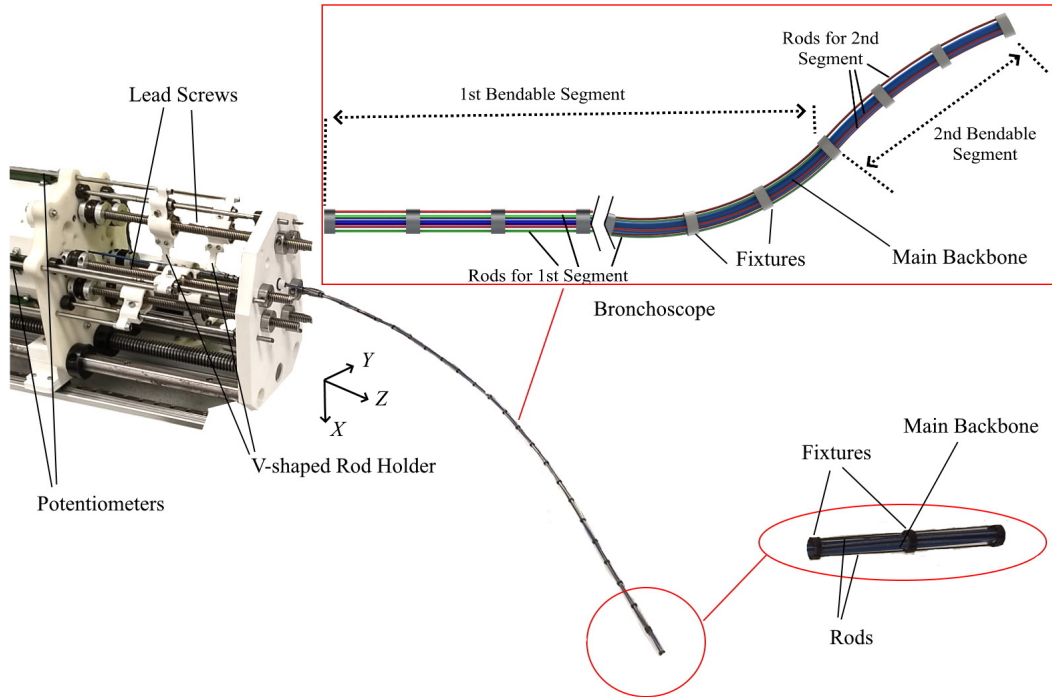
Figure 6.2: The robotic bronchoscope. (a) The inlet shows the tip of the bronchoscope which is composed of two segments that can be independently bent. By pulling/pushing the wires at each segment the bronchoscope can bend in 3D space. (b) The bronchoscope prototype placed inside a 3D printed lung model. An electromagnetic tracker (Aurora electromagnetic tracking system, NDI, Canada) is placed at the tip of the bronchoscope to measure its tip position in real-time. (c) Camera view from the endoscopic camera placed inside the working channel of the bronchoscope.

a 7th DoFs is employed for the insertion and retraction of the end-effector into the airways.

All DoFs are actuated by brushless DC motors (Maxon Motors) with a gearhead with a 150 : 1 reduction and a quadratic encoder. Each motor is controlled via a position controller module with a built in PID controller (EPOS4 Compact 50/5 CAN). The controllers employ the encoders feedback to accurately control the position of the motor shaft. The position controllers communicate with a PC via the CAN protocol. A CAN-to-USB interface (Kvaser Inc., CA, USA) is used to connect the position controllers to the PC.

The motors are connected to lead screws that convert the power generated by the motor into feed velocity for pulling/pushing the rods. The lead screws are carrying a v-shaped 3D printed part that is connected to the rods (shown in Fig. 6.2)

and travels along the lead screw to pull/push the rods. Additionally, 6 linear poten-
tiometers are used to accurately measure the displacement of the rods.

Figure 6.2 shows the developed robot and an inlet showcases the different seg-
ments that the manipulator comprises.

6.3   Geometrically Exact Model of the Robot

The Cosserat-rod theory is used [128, 151] to model the robot. First, the model for
a robot with one bendable segment is presented. Next, the model is generalized to
a robot with more segments.

A schematic of the robot is shown in Fig. 6.3. The robot comprises a main
backbone (shown in blue) rigidly connected to the fixtures and three NiTi rods
(shown in red) fixed at the end fixture. The three rods can pass through the rest
of the fixtures and have enough clearance to not create forces and moments but
rather follow the curvature of the main backbone. The relative position of each rod
with respect to the main backbone ($\mathbf{d}_i$, $i = 1, 2, 3$ in Fig. 6.3) is given by

$$\mathbf{d}_i = [\delta\cos(\beta_i), \ \delta\sin(\beta_i), \ 0]^T, \tag{6.1}$$

where δ is the rods' distance from the robots centroid (see Fig. 6.3) and β_i is the
relative angular position of each rod with respect to the main backbone

$$\beta_i = \alpha + (i-1)\frac{2\pi}{3}, \ i = 1, 2, 3, \tag{6.2}$$

with α shown in Fig. 6.3.

The robot main backbone is modelled as a long, slender, one-dimensional
Cosserat rod endowed with a rotation frame attached to every point on its arc with
the z axis of the frame tangent to the curve. The rod is under an external point
force, $\mathbf{F}$ and distributed constant load, $\mathbf{f}$ simulating the weight of the fixtures. The
configuration of the rod can be defined using a unique set of 3D centroids, $\mathbf{r}(s)$ and
a family of orthogonal transformations, $\mathbf{R}(s)$. The position of the main backbone is
defined by
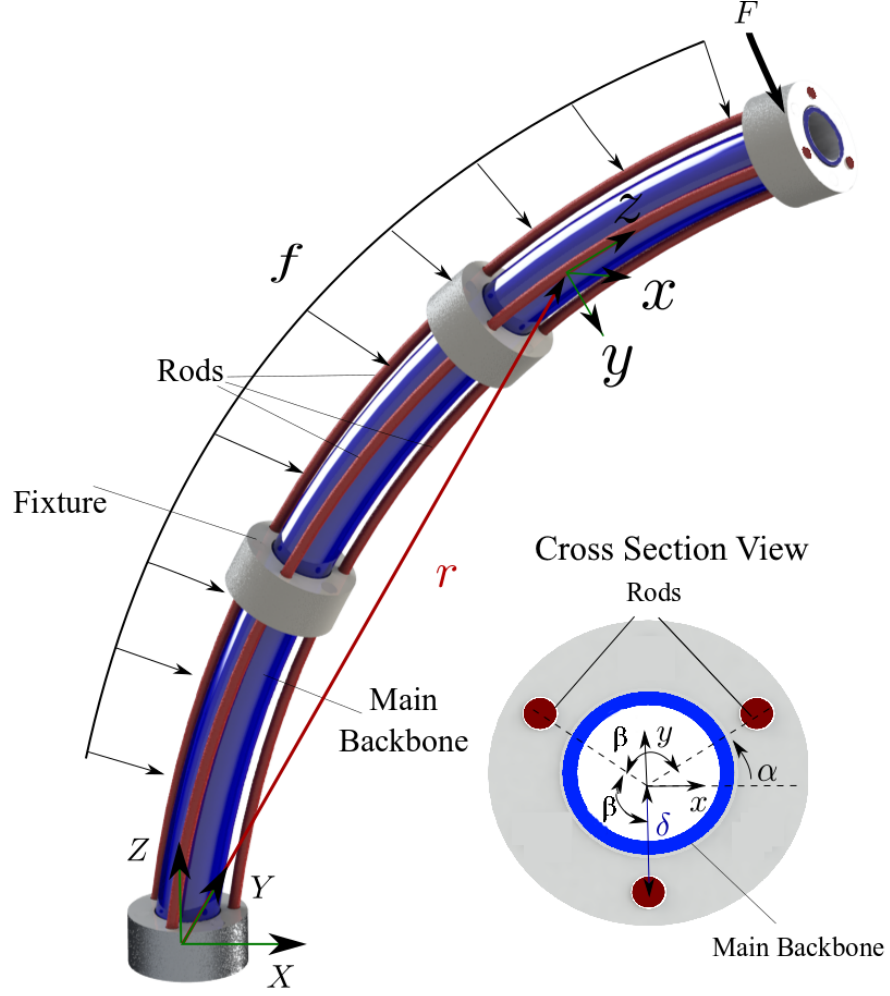
Figure 6.3: A schematic of the continuum robot with one bent segment. The main back-bone is modelled as a Cosserat rod under external point force (F) and distributed load (f). The cross section view shows the position of the rods with respect to the main backbone.

$$\dot{\mathbf{r}}(s) = \mathbf{R}(s)\mathbf{e}_3, \quad \dot{\mathbf{R}}(s) = \mathbf{R}(s)\hat{\mathbf{u}}(s), \tag{6.3}$$

where $\mathbf{u}(s) = [u_x(s), u_y(s), u_z(s)]^T$ is the curvature vector of the deformed backbone, $[.]_\times$ operator is the isomorphism between a vector in $\mathbb{R}^3$ and its skew-symmetric cross product matrix, and $\mathbf{e}_3 = [0,\ 0,\ 1]^T$ is the unit vector aligned with the z-axis of the global coordinate frame. Assuming the rods are made of linear elastic isotropic materials, the constitutive equations for calculating the instantaneous curvature of the rod can be derived [35]

$$\dot{\mathbf{u}}(s) = -\mathbf{K}^{-1}\left[[\mathbf{u}(s)]_\times \mathbf{K}\mathbf{u}(s) + [\mathbf{e}_3]_\times \mathbf{R}^T(s)(\mathbf{F} + (l-s)f)\right], \tag{6.4}$$
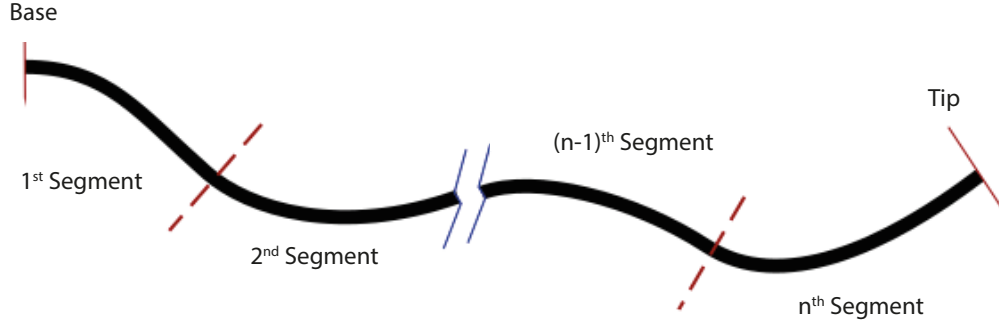
Figure 6.4: A schematic of multi-backbone robot with multiple bending segments, dashed lines denote break points.

where l is the length of the main backbone and $\mathbf{K} = \text{diag}(EI, EI, GJ)$ is the stiffness matrix for the whole robot; E is the robot's Young's modulus; I is the second moment of inertia; G is the shear modulus; J is the polar moment of inertia. It is assumed that the cross section of the robot is symmetric and the products of inertia are negligible (*i.e*, $I_{xy} = I_{xz} = I_{yz} \simeq 0$)

In practice, the robot curvature $\mathbf{u}(s)$ and position $\mathbf{r}(s)$ are unknown and should be estimated as the function of the length of the three rods (ℓ_i, $i = 1, 2, 3$). Each rod's total arc length can be estimated as

$$\ell_i = \int_0^l \|\mathbf{r}_i(s)\| ds, \tag{6.5}$$

where $\|.\|$ denotes the ℓ_2-norm and $\mathbf{r}_i(s)$ is the position of ith rod given by

$$\mathbf{r}_i(s) = \mathbf{r}(s) + \mathbf{R}(s)\mathbf{d}_i. \tag{6.6}$$

Substituting (6.6) in (6.5) and simplifying the equations using (6.3) yields

$$\ell_i = \int_0^l \|\mathbf{e}_3 + [\mathbf{u}(s)]_\times \mathbf{d}_i\| ds, \tag{6.7}$$

Now, the system of differential equations governing the motion of the robot

using (6.3), (6.4), and (6.7) can be written

$$\dot{\mathbf{r}}(s) = \mathbf{R}(s)\mathbf{e}_3, \tag{6.8a}$$

$$\dot{\mathbf{R}}(s,t) = \mathbf{R}(s)[\mathbf{u}(s)]_\times, \tag{6.8b}$$

$$\dot{\mathbf{u}}(s) = -\mathbf{K}^{-1}\left[[\mathbf{u}(s)]_\times\mathbf{K}\mathbf{u}(s) + [\mathbf{e}_3]_\times\mathbf{R}^T(s)(\mathbf{F} + (l-s)\mathbf{f})\right], \tag{6.8c}$$

$$\dot{\ell}_i(s) = \|\mathbf{e}_3 + [\mathbf{u}(s)]_\times\mathbf{d}_i\|, \ i = 1,2,3, \tag{6.8d}$$

with the following boundary conditions

$$\mathbf{r}(0) = [0\ 0\ 0]^T, \tag{6.9a}$$

$$\mathbf{R}(0) = \mathbf{I}, \tag{6.9b}$$

$$u_z(0) = 0, \tag{6.9c}$$

$$\ell_i(0) = 0, \tag{6.9d}$$

$$\ell_i(l) = L_i, \ i = 1,2. \tag{6.9e}$$

The model defined by (6.8) and (6.9) accepts the overall length of the first two rods L_i, $i = 1,2$ as inputs and predicts the robot curvature $\mathbf{u}(s)$, position $\mathbf{r}(s)$, and length of the third rod ℓ_3. The length of the third rod is always defined by the length of the first and second rod. Additionally, (6.8) and (6.9) form a boundary value problem.

In the absence of external torques, the initial curvature of the robot along z direction is zero (6.9c). However, the initial curvatures along x and y directions (*i.e.*, $u_x(0)$ and $u_y(0)$) are unknown. In addition, the first and second rods' arc length $\ell_i(s)$, $i = 1,2$ are defined both at the base ($s = 0$) and the tip of the robot ($s = l$) by (6.9d, 6.9e).

Moreover, the model given in (6.8) is quasi-static and solved using the separation of variables. The equations are solved in the spatial domain (with respect to s) using standard methods such as the Runge-Kutta or Adams–Bashforth families of algorithms. Shooting methods can be used to solve the boundary value problem. A shooting method consists of using a nonlinear root-finding algorithm to iteratively converge on values for $u_x(0,t)$ and $u_y(0,t)$, in order to satisfy (6.9e).

6.3.1   Multi-Segment Robot

Here, the model given in (6.8) is generalized for a multi-backbone robot with multiple bending segments shown in Fig. 6.4. It is assumed that the robot is composed of n segments with lengths of l_j, $j = 1,..,n$. Each segment is actuated via 3 parallel rods fixed at the end the segment. Thus, there are n rods and the jth segment contains $3 \times (n+1-j)$ rods.

To model the robot, I start from the 1st segment containing $n \times 3$ rods and use (6.8) to estimate the curvature, position of the main backbone, and the lengths of the cables up to the next segment. Next, at the junction where the segment ends (shown with dashed lines in Fig. 6.4) the appropriate boundary conditions are enforced. The boundary conditions to be enforced across each transition point between sections are as follows:

1) The position and orientation of each tube must be continuous across the boundary, *i.e.*,

$$\mathbf{r}(s^-) = \mathbf{r}(s^+), \quad \mathbf{R}(s^-) = \mathbf{R}(s^+), \qquad (6.10)$$

2) considering the static equilibrium and the fact that the rods apply no torque around z direction:

$$u_z(s^-) = u_z(s^+), \qquad (6.11)$$

3) at the distal end of each segment, a boundary condition exists for the length of the rods that end:

$$\ell_j(s) = L_j. \qquad (6.12)$$

This process is repeated for the rest of the segments. It should be mentioned that the curvatures along x and y at each break point are unknown. A shooting method must be used to iteratively converge on values for $\{u_x(0), u_y(0), u_x(l_1), u_y(l_1),..., u_x(\Sigma_{j=1}^n l_j), u_y(\Sigma_{j=1}^n l_j)\}$, in order to acquire the desired length for the rods.

6.4   Experimental Analysis

Simulations and experiments are performed to evaluate the proposed design and modelling theory. The bronchoscopic robot used in the simulations and experi-
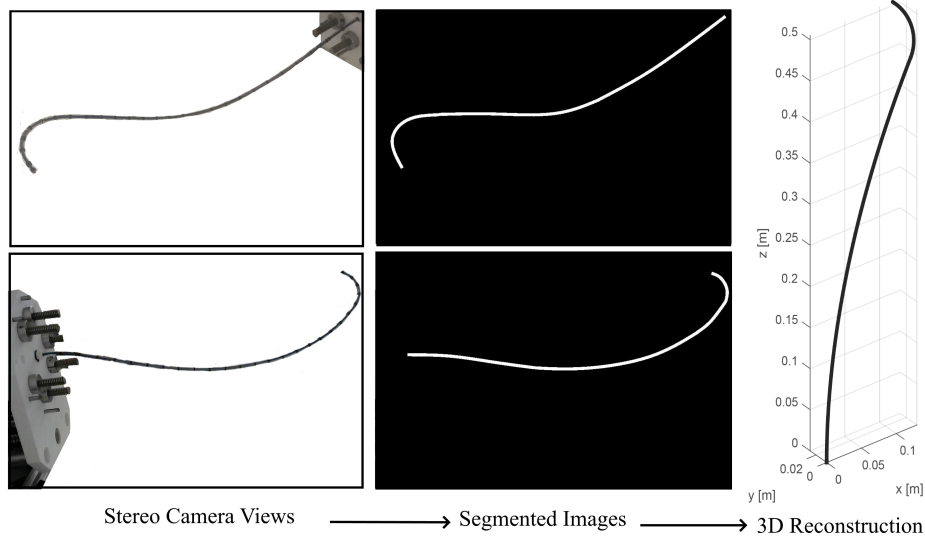
Figure 6.5: Estimating robot's backbone shape using two calibrated cameras.

ments consists of two bendable segments, shown in Fig. 6.2. The length of the first segment is 500 mm, and the length of the second segment (at the tip) is 40 mm. The outer diameter of the robot is 4.5 mm and the inner diameter of the robot is 2 mm. 27 circular fixtures each weighting 5 grams were equally spaced along the length of the bronchoscope and were rigidly fixed to the main backbone shown in blue in Fig. 6.2.

Experiments were performed to identify the developed model parameters and validate the model. First, experiments were performed to identify the model parameters. For the identification phase, each rod was commanded to either push or pull the end disks by 5 mm, making the robot to randomly bend to 12 different positions. The 3D shape of the robot was estimated using calibrated stereo rig comprising two Logitech HD Pro C922 webcams. The cameras were running at 1080p resolution. As identified through calibration using on average 30 views of a checkerboard, a single pixel corresponded to 0.25×0.25 mm on the image plane. Following calibration, the entry point of the robot, *i.e.*, $s = 0$ was estimated in 3D space via triangulation. The robot coordinate frame was aligned to a planar calibration target always visible by the cameras during the experiments.

Furthermore, manual backbone segmentation established the base and shape of the bronchoscope relative to the aligned calibration grid. Matching backbone points
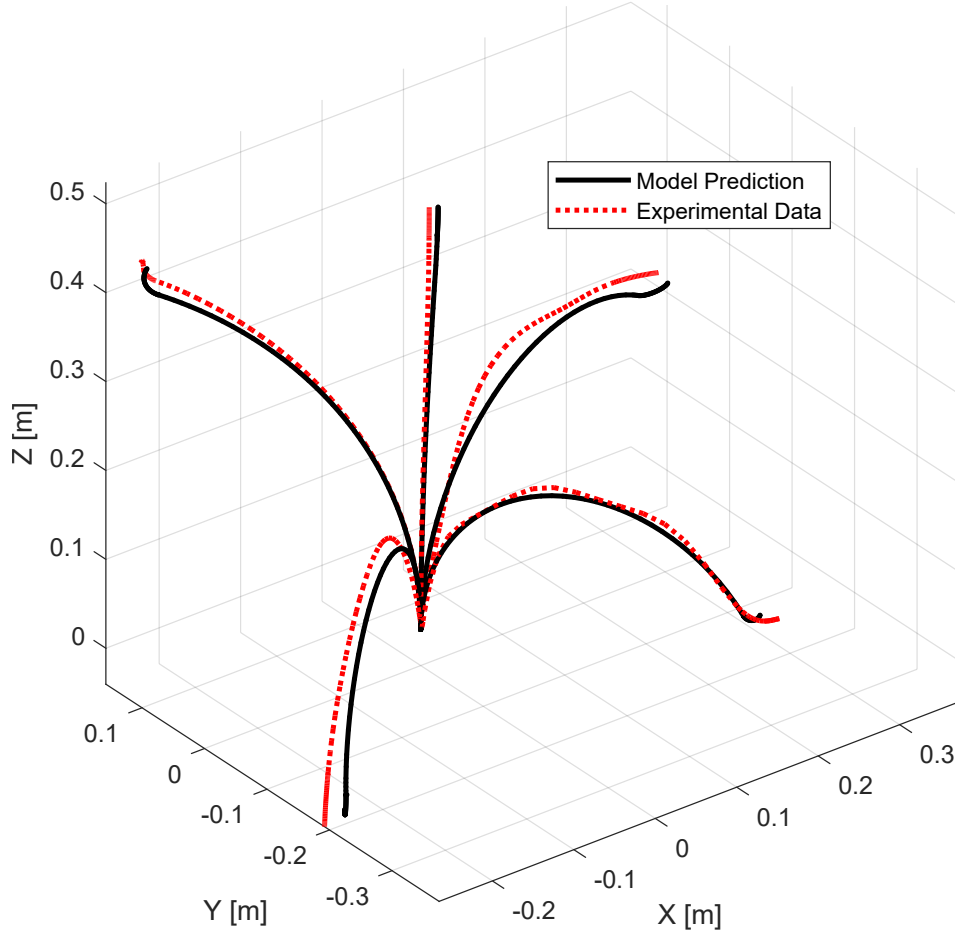
Figure 6.6: A comparison of experimental bronchoscope's shape with model prediction at 4 different configurations.

were selected in both images, and then triangulated to provide the 3D point cloud. This process is shown in Fig. 6.5. The mean error of the 3D triangulation algorithm was equal to 6 pixels corresponding to 1.5 mm. The extracted 3D backbones were used to identify for the robot model parameters, namely, Young's modulus, E and shear moduli G of the robot and initial displacement of the rods, $\delta\ell_i$, $i = 1,...,6$. The parameters were identified by fitting the kinematic model given in (6.8) to the shape of the robot estimated via the cameras at 12 different configurations. The identified parameters of the model and the known parameters of the model are given in Table 5.1.

In the next step, to validate the model accuracy the robot was moved to 20 different positions. The shape of the robot was estimated using the calibrated cameras and was compared to the shape of the robot predicted by the identified model. Fig-

ure 6.6 shows representative results. Results of the measurements including maximum, mean, and standard deviation of error of the model in predicting the robot tip position and the root-mean-squared error of the model in predicting robot shape are listed in Table 5.2. The root-mean-squared error is calculated as

$$\text{RMSE} = \sqrt{\frac{\sum_{j=1}^{m}(\|\hat{r} - r\|_j)^2}{m}},\qquad(6.13)$$

and is used as a measure of the differences between the actual shape of the robot, $\hat{r}$, and the model predicted shape, *i.e.* r, for $m = 30$ data points along the robot backbone.

In the experiments, the robot tip was capable of bending up to 100 degree with respect to its backbone (see Fig. 6.6). The maximum error of the model in estimating the position of the robot tip corresponds to 1.9% of the robot's length.

6.5 Conclusion

In this chapter, the concept for and the design of a continuum robot for pulmonary endoscopy in MV patients was presented. MV patients are at high risk of developing secondary infections and there is a need for a reliable and controlled sampling of the distal lung to guide therapeutic interventions. Current methods for diagnosis of diseases in the distal lung in MV patients are not standardised, lack reproducibility and require expert operators. Here, a novel robotic bronchoscope was presented that can be used to democratise lung sampling and improve the accuracy and reliability of distal lung sampling in MV patients. The proposed design of the system considers the limitations and constraints of current bronchoscopy, *i.e.* limited dexterity, low repeatability, and relatively large size of the bronchoscope.

One of the aims of this research was to democratise ICU bronchoscopy via automating the procedure. The new mechanics-based model of the robotic bronchoscope can predict the shape of the robotic bronchoscope under external forces with an accuracy corresponding to 1.9% of its arc-length. It should be noted that for long, slender continuum robots, tip error is highly dependent on the total arc length

[35] and robot's backbone's interaction with its surrounding environment.

This error can be further reduced via closed-loop control of the robot tip. A closed-loop controller can employ sensory feedback from the robot tip position to minimise the bronchoscope error in navigating the lung. In practice, electromagnetic trackers are placed at the tip of the bronchoscope to measure its tip position in real-time. The proposed design offers a 2 mm working channel that can be used to place such trackers, allowing real-time monitoring of robot position for closed-loop control.

This work is considered to be a representative work showcasing the ability of continuum robots accessing difficult to reach areas and enter the human body via the mouth, nostrils, rectum, and other natural orifices [137].

Chapter 7

Conclusions and Future Directions

7.1 Limitations and Future Directions

This dissertation has provided several contributions in the field of CTRs and in general in continuum robotics. Having presented new design options and modelling theories, I have laid the foundations for future research in these topics. Moreover, limitations of this research work are highlighted here as these limitations can highlight future opportunities for research.

7.1.1 Limitations

The content of this dissertation has been affected by several factors. The bending of NiTi tubes, in the diameter needed to build the navigation section as described in Chapter 4, did not take place due to the high tubes' stiffness and the time consuming process of patterning. This fact did not allow the experimental evaluation through the development of a complete system of the aforementioned concept however, this limitation inspired the research of Chapter 5. That research has laid the foundations for the development of hybrid continuum robots. Moreover, the experimental evaluation of the design options described in Chapters 4-5 in a mockup scenario as the one in Chapter 3 has not been performed and challenges for the introduction of these systems in the OR remain open.

7.1.2 Future Work in Hardware Design

CTRs and continuum robots in general promise to perform several interventions in a less invasive way. The systems presented in this dissertation aim to be proof of

concept of making deep orbital interventions and distal lung sampling less invasive. Moreover, a new system combining two prominent technologies in continuum robots was presented. In the future, the complete development of the system described in Chapter 4 should be performed through the anisotropic patterning of NiTi tubes with large diameter. This will also allow the performance of a comparative study between the design of a hybrid robot compared to the design of a multi-arm CTR robot. It will make clear to the scientific community which design options should be followed to develop miniature continuum end-effectors.

Future studies on open design challenges could be the key to bring theses systems one step closer to the operating theater (OR). One such opportunity for the design advancement is to take into account the needed sterility that theses systems should have and the incorporation of additional sensing technologies like magnetic trackers and fiber Bragg grating strain sensors. Moreover, a more compact version of the system could be implemented, facilitating in this way their usage in an actual OR. Also, an intuitive way to control the designed robots could be implemented in the future so to take full advantage of their potentials. The systems can be integrated to a haptic device offering the ability to the surgeons to perform in a easy way the control of the robotic tools and also gain haptic feedback.

7.1.3   Future Work in Modeling and Analysis

In this dissertation, several models were presented with each one able to predict the shape of each one of the designed robots. However, there are still open challenges despite the precision that the models can offer. While the topic of forward kinematics and static problems has been addressed, real-time implementation, inverse kinematics and dynamic control remain subjects for future work. The introduction of dynamical phenomena in theoretical works can minimize the error between models and reality while the dynamic control can offer accomplishment of surgical tasks faster and in more stable way. Moreover, real-time implementation of the developed models is important to employ control algorithms. Computational efficient models are needed to be able to predict the robot's shape in real-time enabling in this way their control.

7.2 Conclusions

This dissertation has presented 5 main contributions to the established, yet growing body of knowledge about continuum robots and more specifically about CTRs. In Chapter 1, a detailed literature review on CTRs was presented with an emphasis on the design of existing robots and on the modelling theories describing the kinematics of this class of continuum robots. In Chapter 3, the first multi-arm CTRs for ONSF was developed and presented. The concept of accessing the eye cavity by following the eye's curvature was validated through a set of experiments. In Chapter 4, I derived and experimentally validated a new mechanics-based model for eccentrically arranged concentric tube arms housed in a flexible variable stiffness backbone composed of NiTi tubes. Chapter 5 discusses the development of the first system combining push/pull technology and concentric tube technology. A generalized mechanics-based model was developed and experimentally evaluated for this new hybrid continuum robot. Finally, the main contribution of Chapter 6 is the design of a system for thoracic interventions for which a mechanics-based model, employing the Cosserat rod theory, was presented and experimentally evaluated.

Bibliography

[1] Z. Mitros, R. Henry, S. L. D. Cruz, and Sadati, and C. Bergeles, "From Theoretical Work to Clinical Translation: Progress in Concen-tric Tube Robots," *Annual Review of Control, Robotics, and Autonomous Systems*, 2021.

[2] Z. Mitros, S. Sadati, C. Seneci, E. Bloch, K. Leibrandt, M. Khadem, L. D. Cruz, and C. Bergeles, "Optic Nerve Sheath Fenestration with a Multi-Arm Continuum Robot," *IEEE Robotics and Automation Letters*, vol. 5, no. 3, pp. 4874–4881, 2020.

[3] Z. Mitros, M. Khadem, C. Seneci, S. Ourselin, L. Da Cruz, and C. Bergeles, "Towards Modelling Multi-Arm Robots: Eccentric Arrangement of Concentric Tubes," in *IEEE International Conference on Biomedical Robotics and Biomechatronics*, 2018, pp. 43–48.

[4] Z. Mitros, M. Khadem, C. Seneci, L. D. Cruz, and C. Bergeles, "Mechanics modelling of eccentrically arranged concentric tubes," in *Hamlyn Symposium on Medical Robotics*, 2018, pp. 23–24.

[5] Z. Mitros, S. Sadati, S. Nousias, L. D. Cruz, and C. Bergeles, "Design and quasistatic modelling of hybrid continuum multi-arm robots," in *IEEE International Conference on Robotics and Automation*, 2022.

[6] Z. Mitros, B. Thamo, C. Bergeles, L. da Cruz, K. Dhaliwal, and M. Khadem, "Design and modelling of a continuum robot for distal lung sampling in mechanically ventilated patients in critical care," *Frontiers in Robotics and AI*, vol. 8, p. 94, 2021.

[7] A. Bajo and N. Simaan, "Hybrid motion/force control of multi-backbone continuum robots," *The International Journal of Robotics Research*, vol. 35, no. 4, pp. 422–434, 2016.

[8] C. E. Bryson and D. C. Rucker, "Toward parallel continuum manipulators," in *2014 IEEE International Conference on Robotics and Automation (ICRA)*, 2014, pp. 778–785.

[9] D. B. Camarillo, C. F. Milne, C. R. Carlson, M. R. Zinn, and J. K. Salisbury, "Mechanics modeling of tendon-driven continuum manipulators," *IEEE Transactions on Robotics*, vol. 24, no. 6, pp. 1262–1273, 2008.

[10] M. S. Moses, M. D. M. Kutzer, H. Ma, and M. Armand, "A continuum manipulator made of interlocking fibers," in *2013 IEEE International Conference on Robotics and Automation*, 2013, pp. 4008–4015.

[11] J. Till, V. Aloi, and C. Rucker, "Real-Time Dynamics of Soft and Continuum Robots Based on Cosserat Rod Models," *The International Journal of Robotics Research*, vol. 38, no. 6, pp. 723–746, 8 2019.

[12] E. Amanov, T.-D. Nguyen, and J. Burgner-Kahrs, "Tendon-Driven Continuum Robots with Extensible Sections — A Model-Based Evaluation of Path-Following Motions," *The International Journal of Robotics Research*, p. 0278364919886047, 5 2019.

[13] R. Grassmann, V. Modes, and J. Burgner-Kahrs, "Learning the Forward and Inverse Kinematics of a 6-DOF Concentric Tube Continuum Robot in SE(3)," in *IEEE/RSJ International Conference on Intelligent Robots and Systems*, 4 2018, pp. 5125–5132.

[14] G. Chen, M. T. Pham, and T. Redarce, "Development and kinematic analysis of a silicone-rubber bending tip for colonoscopy," in *2006 IEEE/RSJ International Conference on Intelligent Robots and Systems*, 2006, pp. 168–173.

[15] Y. Goergen, R. Chadda, R. Britz, D. Scholtes, N. Koev, P. Motzki, R. Werth-schützky, M. Kupnik, and S. Seelecke, "Shape memory alloys in continuum and soft robotic applications," 09 2019.

[16] K. Ikuta, Y. Matsuda, D. Yajima, and Y. Ota, "Pressure pulse drive: A control method for the precise bending of hydraulic active catheters," *IEEE/ASME Transactions on Mechatronics*, vol. 17, no. 5, pp. 876–883, 2012.

[17] L. Wu, B. L. W. Tan, and H. Ren, "Prototype Development of a Hand-Held Robotic Light Pipe for Intraocular Procedures," in *IEEE International Conference on Robotics and Biomimetics*, 2015, pp. 368–373.

[18] R. J. Hendrick, C. R. Mitchell, S. D. Herrell, and R. J. Webster III, "Hand-held Transendoscopic Robotic Manipulators: A Transurethral Laser Prostate Surgery Case Study," *International Journal of Robotics Research*, vol. 34, no. 13, pp. 1559–1572, 5 2015.

[19] C. Girerd and T. K. Morimoto, "Design and Control of a Hand-Held Concentric Tube Robot for Minimally Invasive Surgery," *IEEE Transactions on Robotics*, 2020.

[20] J. Burgner, P. J. Swaney, R. A. Lathrop, K. D. Weaver, and R. J. Webster, "Debulking from Within: A Robotic Steerable Cannula for Intracerebral Hemorrhage Evacuation," *IEEE Transactions on Biomedical Engineering*, vol. 60, no. 9, pp. 2567–2575, 2013.

[21] A. H. Gosline, N. V. Vasilyev, A. Veeramani, M. Wu, G. Schmitz, R. Chen, V. Arabagi, P. J. d. Nido, and P. E. Dupont, "Metal MEMS tools for Beating-Heart Tissue Removal," in *IEEE International Conference on Robotics and Automation*, 2012, pp. 1921–1926.

[22] H. B. Gilbert, "Concentric Tube Robots: Design, Deployment, and Stability," Ph.D. dissertation, Vanderbilt University, 2016.

[23] J. Burgner, D. C. Rucker, H. B. Gilbert, P. J. Swaney, P. T. Russell, K. D. Weaver, and R. J. Webster, "A Telerobotic System for Transnasal Surgery," *IEEE/ASME Transactions on Mechatronics*, vol. 19, no. 3, pp. 996–1006, 2014.

[24] E. Amanov, T. D. Nguyen, S. Markmann, F. Imkamp, and J. Burgner-Kahrs, "Toward a Flexible Variable Stiffness Endoport for Single-Site Partial Nephrectomy," *Annals of Biomedical Engineering*, vol. 46, no. 10, pp. 1498–1510, 2018.

[25] N. Mukherjee, M. A. El-Dairi, and M. T. Bhatt, "Optic nerve sheath fenestration - indications and techniques," *US Ophthalmic Review*, vol. 6, no. 2, pp. 125–132, Jul. 2013.

[26] J. Burgner-Kahrs, D. C. Rucker, and H. Choset, "Continuum Robots for Medical Applications: A Survey," *IEEE Transactions on Robotics*, vol. 31, no. 6, pp. 1261–1280, 2015.

[27] V. Vitiello, S.-L. Lee, T. P. Cundy, and G.-Z. Yang, "Emerging Robotic Platforms for Minimally Invasive Surgery," *IEEE Reviews in Biomedical Engineering*, vol. 6, pp. 111–126, 2013.

[28] G. Robinson and J. Davies, "Continuum robots - a state of the art," in *Proceedings 1999 IEEE International Conference on Robotics and Automation (Cat. No.99CH36288C)*, vol. 4, 1999, pp. 2849–2854 vol.4.

[29] J. Till, C. E. Bryson, S. Chung, A. Orekhov, and D. C. Rucker, "Efficient computation of multiple coupled cosserat rod models for real-time simulation and control of parallel continuum manipulators," in *2015 IEEE International Conference on Robotics and Automation (ICRA)*, 2015, pp. 5067–5074.

[30] F. Janabi-Sharifi, A. Jalali, and I. D. Walker, "Cosserat rod-based dynamic modeling of tendon-driven continuum robots: A tutorial," *IEEE Access*, vol. 9, pp. 68 703–68 719, 2021.

[31] D. P. Noonan, V. Vitiello, J. Shang, C. J. Payne, and G.-Z. Yang, "A modular, mechatronic joint design for a flexible access platform for mis," in *2011 IEEE/RSJ International Conference on Intelligent Robots and Systems*, 2011, pp. 949–954.

[32] J. Bishop-Moser and S. Kota, "Towards snake-like soft robots: Design of fluidic fiber-reinforced elastomeric helical manipulators," in *2013 IEEE/RSJ International Conference on Intelligent Robots and Systems*, 2013, pp. 5021–5026.

[33] W. McMahan, V. Chitrakaran, M. Csencsits, D. Dawson, I. Walker, B. Jones, M. Pritts, D. Dienno, M. Grissom, and C. Rahn, "Field trials and testing of the octarm continuum manipulator," in *Proceedings 2006 IEEE International Conference on Robotics and Automation, 2006. ICRA 2006.*, 2006, pp. 2336–2341.

[34] P. E. Dupont, J. Lock, B. Itkowitz, and E. Butler, "Design and Control of Concentric Tube Robots," *IEEE Transactions on Robotics*, vol. 26, no. 2, pp. 209–225, 2010.

[35] D. C. Rucker, B. A. Jones, and R. J. Webster, "A Geometrically Exact Model for Externally Loaded Concentric Tube Continuum Robots," *IEEE Transactions on Robotics*, vol. 26, no. 5, pp. 769–780, 2010.

[36] B. L. Bates, T. A. Hall, and T. A. Osborne, "Guide for Localizing a Nonpalpable Breast Lension," 1993.

[37] A. Cuschieri and G. Buess, *Operative Manual of Endoscopic Surgery*, 1992.

[38] W. R. Daum and N. Schalgdorf, "Deflectable Needle Assembly, Patent No: US 6,572,593 b1," 1995.

[39] J. Furusho, T. Ono, R. Murai, T. Fujimoto, Y. Chiba, and H. Horio, "Development of a Curved Multi-Tube (CMT) Catheter for percutaneous umbilical blood sampling and control methods of CMT catheters for solid organs,"

International Conference on Mechatronics and Automation, pp. 410–415, 2005.

[40] R. J. Webster, A. M. Okamura, and N. J. N. J. Cowan, "Toward Active Cannulas: Miniature Snake-Like Surgical Robots," in *IEEE/RSJ International Conference on Intelligent Robots and Systems*, 2006, pp. 2857–2863.

[41] P. Sears and P. E. Dupont, "A Steerable Needle Technology Using Curved Concentric Tubes," in *IEEE International Conference on Intelligent Robots and Systems*, 2006, pp. 2850–2856.

[42] T. L. Bruns, A. A. Remirez, M. A. Emerson, R. A. Lathrop, A. W. Mahoney, H. B. Gilbert, C. L. Liu, P. T. Russell, R. F. Labadie, K. D. Weaver, and R. J. W. Iii, "A Modular, Multi-Arm Concentric Tube Robot System with Application to Transnasal Surgery for Orbital Tumors," *The International Journal of Robotics Research*, vol. 40, pp. 521–533, 2021.

[43] A. W. Mahoney, H. B. Gilbert, and R. J. Webster, "A Review of Concentric Tube Robots: Modeling, Control, Design, Planning, and Sensing," in *The Encyclopedia of Medical Robotics*. WORLD SCIENTIFIC, 5 2018, no. 4, pp. 181–202.

[44] H. Alfalahi, F. Renda, and C. Stefanini, "Concentric Tube Robots for Minimally Invasive Surgery: Current Applications and Future Opportunities," *IEEE Transactions on Medical Robotics and Bionics*, vol. 3202, no. MAY, pp. 1–1, 2020.

[45] H. Gilbert, D. C. Rucker, and R. Webster, "Concentric tube robots: The state of the art and future directions," in *ISRR*, 2013.

[46] H. B. Gilbert, R. J. Webster, and U. e. Al., "Rapid, Reliable Shape Setting of Superelastic Nitinol for Prototyping Robots," *IEEE Robotics and Automation Letters*, vol. 1, no. 1, pp. 98–105, 2016.

[47] P. Sears and P. E. Dupont, "Inverse Kinematics of Concentric Tube Steerable Needles," in *IEEE International Conference on Robotics and Automation*, 2007, pp. 1887–1892.

[48] R. J. Webster, J. M. Romano, N. J. Cowan, I. I. I. Webster Robert J., J. M. Romano, and N. J. Cowan, "Mechanics of Precurved-Tube Continuum Robots," *IEEE Transactions on Robotics*, vol. 25, no. 1, pp. 67–78, 2009.

[49] P. E. Dupont, J. Lock, and B. Itkowitz, "Real-Time Position Control of Concentric Tube Robots," in *IEEE International Conference on Robotics and Automation*, 2010, pp. 562–568.

[50] R. Xu, A. Asadian, A. S. Naidu, and R. V. Patel, "Position Control of Concentric-Tube Continuum Robots using a Modified Jacobian-Based Approach," in *IEEE International Conference on Robotics and Automation*, 2013, pp. 5813–5818.

[51] C. Baek, K. Yoon, and D. N. Kim, "Finite Element Modeling of Concentric-Tube Continuum Robots," *Structural Engineering and Mechanics*, vol. 57, no. 5, pp. 809–821, 2016.

[52] M. Pourafzal, H. A. Talebi, and K. Rabenorosoa, "Piecewise Constant Strain Kinematic Model of Externally Loaded Concentric," *Mechatronics*, vol. 74, p. 102502, 2021.

[53] F. Renda, C. Messer, C. Rucker, and F. Boyer, "A Sliding-rod Variable-strain Model for Concentric Tube Robots," *IEEE Robotics and Automation Letters*, no. 1, pp. 1–8, 2021.

[54] S. Sadati, Z. Mitros, R. Henry, L. D. Cruz, and C. Bergeles, "Reduced-Order Real-Time Dynamics of Concentric Tube Robots: A Polynomial Shape (PS) Parametrization," King's College London, Tech. Rep., 2020.

[55] G. Fagogenis, C. Bergeles, and P. E. Dupont, "Adaptive Nonparametric Kinematic Modeling of Concentric Tube Robots," in *IEEE International Conference on Intelligent Robots and Systems*, 2016, pp. 4324–4329.

[56] A. Kuntz, A. Sethi, R. J. Webster, and R. Alterovitz, "Learning the Complete Shape of Concentric Tube Robots," *IEEE Transactions on Medical Robotics and Bionics*, vol. 2, no. 2, pp. 140–147, 2020.

[57] D. C. Rucker, B. A. Jones, and R. J. Webster, "A Model for Concentric Tube Continuum Robots Under Applied Wrenches," in *IEEE International Conference on Robotics and Automation*, 2010, pp. 1047–1052.

[58] J. Lock, G. Laing, M. Mahvash, and P. E. Dupont, "Quasistatic Modeling of Concentric Tube Robots with External Loads," in *IEEE/RSJ International Conference on Intelligent Robots and Systems*, 2010, pp. 2325–2332.

[59] D. C. Rucker, R. J. Webster, G. S. Chirikjian, and N. J. Cowan, "Equilibrium Conformations of Concentric-tube Continuum Robots," *The International Journal of Robotics Research*, vol. 29, no. 10, pp. 1263–1280, 5 2010.

[60] C. Girerd, K. Rabenorosoa, P. Rougeot, and P. Renaud, "Towards Optical Biopsy of Olfactory Cells using Concentric Tube Robots with Follow-the-Leader Deployment," in *IEEE/RSJ International Conference on Intelligent Robots and Systems*, 2017, pp. 5661–5887.

[61] C. Kim, S. C. Ryu, and P. E. Dupont, "Real-Time Adaptive Kinematic Model Estimation of Concentric Tube Robots," in *IEEE/RSJ International Conference on Intelligent Robots and Systems*, 2015, pp. 3214–3219.

[62] C. Jang, J. Ha, P. E. Dupont, and F. C. Park, "Toward on-line parameter estimation of concentric tube robots using a mechanics-based kinematic model," in *IEEE/RSJ International Conference on Intelligent Robots and Systems*, 2016, pp. 2400–2405.

[63] J. Ha, F. C. Park, and P. E. Dupont, "Optimizing Tube Precurvature to Enhance the Elastic Stability of Concentric Tube Robots," *IEEE Transactions on Robotics*, vol. 33, no. 1, pp. 22–37, 2 2017.

[64] Q. Peyron, K. Rabenorosoa, N. Andreff, and P. Renaud, "A Numerical Framework for the Stability and Cardinality Analysis of Concentric Tube Robots: Introduction and Application to the Follow-the-Leader Deployment," *Mechanism and Machine Theory*, vol. 132, pp. 176–192, 2019.

[65] R. J. Hendrick, H. B. Gilbert, and R. J. Webster, "Designing Snap-Free Concentric Tube Robots: A Local Bifurcation Approach," in *IEEE International Conference on Robotics and Automation*, 2015, pp. 2256–2263.

[66] C. Bergeles and P. E. Dupont, "Planning Stable Paths for Concentric Tube Robots," in *IEEE/RSJ International Conference on Intelligent Robots and Systems*, 2013, pp. 3077–3082.

[67] R. Xu, S. F. Atashzar, and R. V. Patel, "Kinematic Instability in Concentric Tube Robots: Modeling and Analysis," in *IEEE RAS/EMBS International Conference on Biomedical Robotics and Biomechatronics*, 2014, pp. 163–168.

[68] J. Ha, F. C. Park, and P. E. Dupont, "Achieving Elastic Stability of Concentric Tube Robots Through Optimization of Tube Precurvature," in *IEEE/RSJ International Conference on Intelligent Robots and Systems*, 2014, pp. 864–870.

[69] H. B. Gilbert, R. J. Hendrick, R. J. Webster, and R. J. Webster III, "Elastic Stability of Concentric Tube Robots: A Stability Measure and Design Test," *IEEE Transactions on Robotics*, vol. 32, no. 1, pp. 20–35, 2016.

[70] J. Ha, F. C. Park, and P. E. Dupont, "Elastic Stability of Concentric Tube Robots Subject to External Loads," *IEEE Transactions on Biomedical Engineering*, vol. 63, no. 6, pp. 1116–1128, 2016.

[71] K. E. Riojas, R. J. Hendrick, and R. J. Webster, "Can Elastic Instability Be Beneficial in Concentric Tube Robots?" *IEEE Robotics and Automation Letters*, vol. 3, no. 3, pp. 1624–1630, 7 2018.

[72] J. Till, V. Aloi, K. E. Riojas, P. L. Anderson, R. J. Webster, and C. Rucker, "A Dynamic Model for Concentric Tube Robots," *IEEE Transactions on Robotics*, vol. 36, no. 6, pp. 1704–1718, 2020.

[73] J. Lock and P. E. Dupont, "Friction Modeling in Concentric Tube Robots," in *IEEE International Conference on Robotics and Automation*, 2011, pp. 1139–1146.

[74] J. Ha, G. Fagogenis, and P. E. Dupont, "Modeling Tube Clearance and Bounding the Effect of Friction in Concentric Tube Robot Kinematics," *IEEE Transactions on Robotics*, vol. 35, no. 2, pp. 353–370, 4 2019.

[75] R. J. Webster, J. M. Romano, and N. J. Cowan, "Kinematics and Calibration of Active Cannulas," in *IEEE International Conference on Robotics and Automation*, 2008, pp. 3888–3895.

[76] L. A. Lyons, R. J. Webster, and R. Alterovitz, "Motion Planning for Active Cannulas," in *IEEE/RSJ International Conference on Intelligent Robots and Systems*, 2009, pp. 801–806.

[77] D. C. Rucker and R. J. Webster, "Computing Jacobians and Compliance Matrices for Externally Loaded Continuum Robots," in *IEEE International Conference on Robotics and Automation*, 2011, pp. 945–950.

[78] L. G. Torres, C. Baykal, and R. Alterovitz, "Interactive-Rate Motion Planning for Concentric Tube Robots," in *IEEE International Conference on Robotics and Automation*, 2014, pp. 1915–1921.

[79] M. Khadem, J. O'Neill, Z. Mitros, L. Da Cruz, and C. Bergeles, "Autonomous steering of concentric tube robots via nonlinear model predictive

control," *IEEE Transactions on Robotics*, vol. 36, no. 5, pp. 1595–1602, 2020.

[80] K. Leibrandt, C. Bergeles, G.-z. Yang, B. K. Leibrandt, C. Bergeles, and G.-z. Yang, "Concentric Tube Robots: Rapid, Stable Path-Planning and Guidance for Surgical Use," *IEEE Robotics & Automation Magazine*, vol. 24, no. 2, pp. 42–53, 5 2017.

[81] R. Xu and R. V. Patel, "A Fast Torsionally Compliant Kinematic Model of Concentric Tube Robots," in *IEEE International Conference of Engineering in Medicine and Biology*, 2012, pp. 904–907.

[82] R. Xu, A. Asadian, S. F. Atashzar, and R. V. Patel, "Real-Time Trajectory Tracking for Externally Loaded Concentric-Tube Robots," in *IEEE International Conference on Robotics and Automation*, 2014, pp. 4374–4379.

[83] J. Ha and P. E. Dupont, "Designing Stable Concentric Tube Robots Using Piecewise Straight Tubes," *IEEE Robotics and Automation Letters*, vol. 2, no. 1, pp. 298–304, 2017.

[84] J. A. Childs and C. Rucker, "Concentric Precurved Bellows: New Bending Actuators for Soft Robots," *IEEE Robotics and Automation Letters*, vol. 5, no. 2, pp. 1215–1222, 2020.

[85] W. Wei, R. Goldman, N. Simaan, H. Fine, and S. Chang, "Design and Theoretical Evaluation of Micro-Surgical Manipulators for Orbital Manipulation and Intraocular Dexterity," *IEEE International Conference on Robotics and Automation*, pp. 3389–3395, 2007.

[86] W. Wei, R. E. Goldman, H. F. Fine, S. Chang, and N. Simaan, "Performance Evaluation for Multi-Arm Manipulation of Hollow Suspended Organs," *IEEE Transactions on Robotics*, vol. 25, no. 1, pp. 147–157, 2009.

[87] F.-Y. Lin, C. Bergeles, and G.-Z. Z. Yang, "Biometry-Based Concentric Tubes Robot for Vitreoretinal Surgery," in *IEEE International Conference on Engineering in Medicine and Biology*, 2015, pp. 5280–5284.

[88] G. Dwyer, F. Chadebecq, M. T. Amo, C. Bergeles, E. Maneas, V. Pawar, E. V. Poorten, J. Deprest, S. Ourselin, P. De Coppi, T. Vercauteren, and D. Stoyanov, "A Continuum Robot and Control Interface for Surgical Assist in Fetoscopic Interventions," *IEEE Robotics and Automation Letters*, vol. 2, no. 3, pp. 1656–1663, 2017.

[89] G. Dwyer, E. J. Alles, R. J. Colchester, K. Iyengar, A. E. Desjardins, and D. Stoyanov, "Robot-assisted optical ultrasound scanning," *IEEE Transactions on Medical Robotics and Bionics*, vol. 3, no. 4, pp. 948–958, 2021.

[90] T. Vandebroek, M. Ourak, C. Gruijthuijsen, A. Javaux, J. Legrand, T. Vercauteren, S. Ourselin, J. Deprest, and E. V. Poorten, "Macro-Micro Multi-Arm Robot for Single-Port Access Surgery," in *IEEE/RSJ International Conference on Intelligent Robots and Systems*, 2019, pp. 425–432.

[91] A. H. Gosline, N. V. Vasilyev, E. J. Butler, C. Folk, A. Cohen, R. Chen, N. Lang, P. J. Del Nido, and P. E. Dupont, "Percutaneous Intracardiac Beating-Heart Surgery using Metal MEMS Tissue Approximation Tools," *The International Journal of Robotics Research*, vol. 31, no. 9, pp. 1081–1093, 5 2012.

[92] N. V. Vasilyev, A. H. Gosline, A. Veeramani, M. T. Wu, G. P. Schmitz, R. T. Chen, V. Arabagi, P. J. Del Nido, P. E. Dupont, M. Ting Wu, G. P. Schmitz, R. T. Chen, V. Arabagi, P. J. Del Nido, and P. E. Dupont, "Tissue Removal Inside the Beating Heart Using a Robotically Delivered Metal MEMS Tool," *The International Journal of Robotics Research*, vol. 34, no. 2, pp. 236–247, 5 2014.

[93] G. Fagogenis, M. Mencattelli, Z. Machaidze, B. Rosa, K. Price, F. Wu, V. Weixler, M. Saeed, J. E. Mayer, and P. E. Dupont, "Autonomous Robotic

Intracardiac Catheter Navigation Using Haptic Vision," *Science Robotics*, vol. 4, no. 29, p. eaaw1977, 10 2019.

[94] P. J. Swaney, A. W. Mahoney, A. A. Remirez, E. Lamers, B. I. Hartley, R. H. Feins, R. Alterovitz, and R. J. Webster, "Tendons, Concentric Tubes, and a Bevel Tip: Three Steerable Robots in one Transoral Lung Access System," in *IEEE International Conference on Robotics and Automation*, 2015, pp. 5378–5383.

[95] S. Amack, M. F. Rox, M. Emerson, R. J. Webster, R. Alterovitz, A. Kuntz, J. Mitchell, T. E. Ertop, J. Gafford, F. Maldonado, and J. Akulian, "Design and Control of a Compact Modular Robot for Transbronchial Lung Biopsy," in *Medical Imaging: Image-Guided Procedures, Robotic Interventions, and Modeling.*, vol. 1095, 2019.

[96] T. K. Morimoto, E. W. Hawkes, and A. M. Okamura, "Design of a Compact Actuation and Control System for Flexible Medical Robots," *IEEE Robotics and Automation Letters*, vol. 2, no. 3, pp. 1579–1585, 2017.

[97] J. Burgner, P. J. Swaney, D. C. Rucker, H. B. Gilbert, S. T. Nill, P. T. Russell, K. D. Weaver, and R. J. Webster, "A bimanual teleoperated system for endonasal skull base surgery," in *IEEE/RSJ International Conference on Intelligent Robots and Systems*, 2011, pp. 2517–2523.

[98] P. J. Swaney, J. M. Croom, J. Burgner, H. B. Gilbert, D. C. Rucker, R. J. Webster, K. D. Weaver, P. T. Russell, J. M. Croom, J. Burgner, H. B. Gilbert, D. C. Rucker, R. J. W. Iii, and P. T. R. Iii, "Design of a Quadramanual Robot for Single-Nostril Skull Base Surgery," Tech. Rep., 2012.

[99] D. B. Comber, D. Cardona, R. J. Webster III, and E. J. Barth, "Sliding Mode Control of an MRI-Compatible Pneumatically Actuated Robot," *ASME Symposium on Fluid Power and Motion Control*, no. 5, pp. 283–293, 2012.

[100] H. Azimian, T. Looi, and J. Drake, "A Dual-Arm Robotic Neuroendoscope: Early Results," in *Hamlyn Symposium on Medical Robotics*, 2016, pp. 34–35.

[101] H. Su, G. Li, D. C. Rucker, R. J. Webster, G. S. Fischer, R. J. Webster III, and G. S. Fischer, "A Concentric Tube Continuum Robot with Piezoelectric Actuation for MRI-Guided Closed-Loop Targeting," *Annals of Biomedical Engineering*, vol. 44, no. 10, pp. 2863–2873, 5 2016.

[102] M. N. Boushaki, "Design optimization and control for concentric tube robot in assisted single-access laparoscopic surgery," Ph.D. dissertation, Université Montpellier, 2016.

[103] H. Yu, L. Wu, K. Wu, and H. Ren, "Development of a Multi-Channel Concentric Tube Robotic System With Active Vision for Transnasal Nasopharyngeal Carcinoma Procedures," *IEEE Robotics and Automation Letters*, vol. 1, no. 2, pp. 1172–1178, 7 2016.

[104] K. Wu, G. Zhu, L. Wu, W. Gao, S. Song, C. M. Lim, and H. Ren, "Safety-Enhanced Model-Free Visual Servoing for Continuum Tubular Robots Through Singularity Avoidance in Confined Environments," *IEEE Access*, vol. 7, pp. 21 539–21 558, 2019.

[105] X. Yang, S. Song, L. Liu, T. Yan, and M. Q. Meng, "Design and Optimization of Concentric Tube Robots Based on Surgical Tasks, Anatomical Constraints and Follow-the-Leader Deployment," *IEEE Access*, vol. 7, pp. 173 612–173 625, 4 2019.

[106] M. F. Rox, D. S. Ropella, R. J. Hendrick, E. Blum, R. P. Naftel, H. C. Bow, S. D. Herrell, K. D. Weaver, L. B. Chambless, and R. J. Webster, "Mechatronic Design of a Two-Arm Concentric Tube Robot System for Rigid Neuroendoscopy," *IEEE/ASME Transactions on Mechatronics*, vol. 25, no. 3, pp. 1432–1443, 2020.

[107] J. Wang, X. Yang, P. Li, S. Song, L. Liu, and M. Q. Meng, "Design of a Multi-Arm Concentric-Tube Robot System for Transnasal Surgery," *Medical and Biological Engineering and Computing*, vol. 58, no. 3, pp. 497–508, 3 2020.

[108] C. Girerd, A. V. Kudryavtsev, P. Rougeot, P. Renaud, K. Rabenorosoa, and B. Tamadazte, "SLAM-Based Follow-the-Leader Deployment of Concentric Tube Robots," *IEEE Robotics and Automation Letters*, vol. 5, no. 2, pp. 548–555, 4 2020.

[109] A. V. Kudryavtsev, M. T. Chikhaoui, A. Liadov, P. Rougeot, F. Spindler, K. Rabenorosoa, J. Burgner-Kahrs, B. Tamadazte, and N. Andreff, "Eye-in-hand visual servoing of concentric tube robots," *IEEE Robotics and Automation Letters*, vol. 3, no. 3, pp. 2315–2321, 2018.

[110] J. Kim, W.-Y. Choi, S. Kang, C. Kim, and K.-J. Cho, "Continuously variable stiffness mechanism using nonuniform patterns on coaxial tubes for continuum microsurgical robot," *IEEE Transactions on Robotics*, vol. 35, no. 6, pp. 1475–1487, 2019.

[111] M. Khadem, J. O'Neill, Z. Mitros, L. D. Cruz, and C. Bergeles, "Autonomous Steering of Concentric Tube Robots for Enhanced Force/Velocity Manipulability," in *IEEE International Conference on Intelligent Robots and Systems*, 2019, pp. 2197–2204.

[112] Y. Lu, C. Zhang, S. Song, and M. Q. Meng, "Precise Motion Control of Concentric-Tube Robot based on Visual Servoing," in *IEEE International Conference on Information and Automation*, 2017, pp. 299–304.

[113] G. Noh, S. Y. Yoon, S. Yoon, K. Kim, W. Lee, S. Kang, and D. Lee, "Expeditious Design Optimization of a Concentric Tube Robot with a Heat-Shrink Plastic Tube," in *IEEE International Conference on Intelligent Robots and Systems*, vol. 2016-Novem, 2016, pp. 3671–3676.

[114] T. Anor, J. R. Madsen, and P. Dupont, "Algorithms for Design of Continuum Robots using the Concentric Tubes Approach: A Neurosurgical Example," in *IEEE International Conference on Robotics and Automation*, 2011, pp. 667–673.

[115] C. Bedell, J. Lock, A. Gosline, and P. E. Dupont, "Design Optimization of Concentric Tube Robots Based on Task and Anatomical Constraints," in *IEEE International Conference on Robotics and Automation*, 2011, pp. 398–403.

[116] J. Burgner-Kahrs, H. B. Gilbert, R. J. Webster, J. Burgner, H. B. Gilbert, and R. J. Webster, "On the Computational Design of Concentric Tube Robots: Incorporating Volume-Based Objectives," in *IEEE International Conference on Robotics and Automation*, 2013, pp. 1193–1198.

[117] J. Granna, Y. Guo, K. D. Weaver, and J. Burgner-Kahrs, "Comparison of Optimization Algorithms for a Tubular Aspiration Robot for Maximum Coverage in Intracerebral Hemorrhage Evacuation," *Journal of Medical Robotics Research*, vol. 02, no. 01, p. 1750004, 5 2016.

[118] J. Granna, A. Nabavi, and J. Burgner-Kahrs, "Computer-Assisted Planning for a Concentric Tube Robotic System in Neurosurgery," *International Journal of Computer Assisted Radiology and Surgery*, vol. 14, no. 2, pp. 335–344, 5 2019.

[119] L. G. Torres, R. J. Webster, and R. Alterovitz, "Task-Oriented Design of Concentric Tube Robots using Mechanics-Based Models," in *IEEE/RSJ International Conference on Intelligent Robots and Systems*, 2012, pp. 4449–4455.

[120] C. Bergeles, A. H. Gosline, N. V. Vasilyev, P. J. Codd, P. J. del Nido, and P. E. Dupont, "Concentric Tube Robot Design and Optimization Based on Task and Anatomical Constraints," *IEEE Transactions on Robotics*, vol. 31, no. 1, pp. 67–84, 5 2015.

[121] C. Baykal, "Design Optimization Algorithms for Concentric Tube Robots," Master's thesis, University of North Carolina at Chapel Hill, 2015.

[122] J. Ha and P. E. Dupont, "Incorporating Tube-to-Tube Clearances in the Kinematics of Concentric Tube Robots," in *IEEE International Conference on Robotics and Automation*, 2017, pp. 6730–6736.

[123] M. T. Chikhaoui, J. Granna, J. Starke, and J. Burgner-Kahrs, "Toward Motion Coordination Control and Design Optimization for Dual-Arm Concentric Tube Continuum Robots," *IEEE Robotics and Automation Letters*, vol. 3, no. 3, pp. 1793–1800, 2018.

[124] T. K. Morimoto, J. D. Greer, M. H. Hsieh, and A. M. Okamura, "Surgeon Design Interface for Patient-Specific Concentric Tube Robots," in *IEEE International Conference on Biomedical Robotics and Biomechatronics*, vol. 2016, 6 2016, pp. 41–48.

[125] H. Azimian, P. Francis, T. Looi, and J. Drake, "Structurally-Redesigned Concentric-Tube Manipulators with Improved Stability," in *IEEE/RSJ International Conference on Intelligent Robots and Systems*, 2014, pp. 2030–2035.

[126] D. Lee, J. Kim, J. Kim, C. Baek, G. Noh, D. Kim, K. Kim, S. Kang, and K. Cho, "Anisotropic Patterning to Reduce Instability of Concentric-Tube Robots," *IEEE Transactions on Robotics*, vol. 31, no. 6, pp. 1311–1323, 2015.

[127] K. A. Xin Jue Luo, T. Looi, S. Sabetian, and J. Drake, "Designing Concentric Tube Manipulators for Stability Using Topology Optimization," in *IEEE/RSJ International Conference on Intelligent Robots and Systems*, 2018, pp. 1764–1769.

[128] S. S. Antman, *Nonlinear Problems of Elasticity Second Edition*, 2005, vol. 107.

[129] M. Yaqub, M. A. Mehboob, and Q. Ul Islam, "Efficacy and safety of optic nerve sheath fenestration in patients with raised intracranial pressure," *Pak J Med Sci*, vol. 33, no. 2, pp. 471–475, 2017.

[130] R. C. Sergott, P. J. Savino, and T. M. Bosley, "Optic nerve sheath decompression: a clinical review and proposed pathophysiologic mechanism." *Aust N Z J Ophthalmol.*, vol. 18, no. 4, pp. 365–373, 1990.

[131] D. I. Friedman and D. M. Jacobson, "Idiopathic intracranial hypertension," *J NeuroOphthalmology*, vol. 24, no. 2, p. 138–145, 2004.

[132] I. Beckerman, P. Gottlieb, and M. Vaiman, "Variations in eyeball diameters of the healthy adults," *J Ophth.*, Nov. 2014.

[133] K. Leibrandt, C. Bergeles, and G.-Z. Yang, "Implicit Active Constraints for Concentric Tube Robots Based on Analysis of the Safe and Dexterous Workspace," in *IEEE/RSJ International Conference on Intelligent Robots and Systems*, 5 2017, pp. 193–200.

[134] Y. Hua, A. P. Voorhees, and I. A. Sigal, "Cerebrospinal fluid pressure: Revisiting factors influencing optic nerve head biomechanics," *Invest Ophthalmol Vis Sci*, vol. 59, no. 1, pp. 154–165, Jan. 2018.

[135] A. J. Feola, E. S. Nelson, J. Myers, C. R. Ethier, A, and B. C. Samuels, "The impact of choroidal swelling on optic nerve head deformation," *Invest Ophthalmol Vis Sci*, vol. 59, no. 10, pp. 4172–4181, Aug. 2018.

[136] M. U. Farooq, B. Xu, and S. Y. Ko, "A concentric tube-based 4-dof puncturing needle with a novel miniaturized actuation system for vitrectomy," *BioMed Eng OnLine*, vol. 18, no. 46, 2019.

[137] S. Song, H. Ge, J. Wang, and M. Q.-H. Meng, "Real-time multi-object magnetic tracking for multi-arm continuum robots," *IEEE Transactions on Instrumentation and Measurement*, vol. 70, pp. 1–9, 2021.

[138] D.-V.-A. Nguyen, C. Girerd, Q. Boyer, P. Rougeot, O. Lehmann, L. Tavernier, J. Szewczyk, and K. Rabenorosoa, "A hybrid concentric tube robot for cholesteatoma laser surgery," *IEEE Robotics and Automation Letters*, pp. 1–1, 2021.

[139] T. K. Morimoto and A. M. Okamura, "Design of 3-D Printed Concentric Tube Robots," *IEEE Transactions on Robotics*, vol. 32, no. 6, pp. 1419–1430, 2016.

[140] B. Thamo, K. Dhaliwal, and M. Khadem, "Rapid solution of cosserat rod equations via a nonlinear partial observer," in *2021 IEEE International Conference on Robotics and Automation (ICRA)*, 2021, pp. 9433–9438.

[141] M. Abdel-Nasser and O. Salah, "The inverse kinematics analysis for tendon-driven robot based on an adaptive neuro-fuzzy inference system," in *2020 16th International Computer Engineering Conference (ICENCO)*, 2020, pp. 118–123.

[142] L. Wang, F. C. Pedrosa, and R. V. Patel, "Eccentric-Tube Robot (ETR) Modeling and Validation," in *IEEE International Conference on Biomedical Robotics and Biomechatronics*, 2020, pp. 866–871.

[143] J. Wang, J. Peine, and P. E. Dupont, "Eccentric tube robots as multiarmed steerable sheaths," *IEEE Transactions on Robotics*, pp. 1–15, 2021.

[144] R. Hartley and A. Zisserman, *Multiple View Geometry in Computer Vision*, 2nd ed. USA: Cambridge University Press, 2003.

[145] I. A. Gravagne and I. D. Walker, "Kinematic transformations for remotely-actuated planar continuum robots," in *Proceedings 2000 ICRA. Millennium Conference. IEEE International Conference on Robotics and Automation. Symposia Proceedings (Cat. No.00CH37065)*, vol. 1, 2000, pp. 19–26 vol.1.

[146] N. Simaan, R. Taylor, and P. Flint, "A dexterous system for laryngeal surgery," in *IEEE International Conference on Robotics and Automation*, vol. 1, 2004, pp. 351–357 Vol.1.

[147] J. Ding, R. E. Goldman, K. Xu, P. K. Allen, D. L. Fowler, and N. Simaan, "Design and coordination kinematics of an insertable robotic effectors platform for single-port access surgery," *IEEE/ASME Transactions on Mechatronics*, vol. 18, no. 5, pp. 1612–1624, 2013.

[148] G. Del Giudice, L. Wang, J. Shen, K. Joos, and N. Simaan, "Continuum robots for multi-scale motion: Micro-scale motion through equilibrium mod-

ulation," in *IEEE/RSJ International Conference on Intelligent Robots and Systems*, 2017, pp. 2537–2542.

[149] J. Wang, J. Ha, and P. E. Dupont, "Steering a Multi-Armed Robotic Sheath using Eccentric Precurved Tubes," in *IEEE International Conference on Robotics and Automation*, 2019, pp. 9834–9840.

[150] J. H. Kaouk, G.-P. Haber, R. Autorino, S. Crouzet, A. Ouzzane, V. Flamand, and A. Villers, "A novel robotic system for single-port urologic surgery: first clinical investigation." *European urology*, vol. 66, no. 6, pp. 1033–1043, dec 2014.

[151] R. J. Webster and B. A. Jones, "Design and Kinematic Modeling of Constant Curvature Continuum Robots: A Review," *The International Journal of Robotics Research*, vol. 29, no. 13, pp. 1661–1683, 2010.